Development and Characterization of Al-coated Mg Alloy

In Partial Fulfillment of the Requirements for the Degree of Doctor of Engineering

Toko Tokunaga

Hokkaido University
Graduate School of Engineering
Division of Materials Science and Engineering

AGH University of Science and Technology
Faculty of Metals Engineering and Industrial Computer Science

June 2015

Acknowledgments

I would like to express my appreciation to all the people who is involved in the completion of this thesis.

Firstly, I would like to gratefully and sincerely thank my supervisor, Professor Kiyotaka Matsuura in Hokkaido University, for his guidance, understanding and sincere support during my study from undergraduate study. Without his guidance and help, this thesis would not have been possible.

I am deeply grateful to my supervisor in Poland, Professor Maciej Pietrzyk in AGH University of Science and Technology. I appreciate his sincere and continuous support of my study not only in Poland but also when I was in Japan. His kindness and great knowledge keep me motivated during my stay in Poland.

I would like to thank Professor Munekazu Ohno in Hokkaido University. All his advices and comments inspired me very much.

Thanks must go to Professor Marta Ziemnicka-Sylwester in Hokkaido University. I have been motivated by her devotion to work.

I would also like to thank Professor Seiji Miura, Professor Masatoshi Sakairi, Professor Michał Krzyżanowski and Professor Krzysztof Banaś for their kind and continuous supports.

I am grateful for Mr. Nobuyuki Miyazaki, Mr. Kenji Ohkubo, Mr. Takashi Endo, Mr. Keita Suzuki, Mr. Kenta Chubachi, Mr. Yuji Mori and Ms. Mika Yamamoto for their technical supports. I have learnt a lot from them and it was a great pleasure to work with them.

I would like to thank Professor Danuta Szeliga and Mr. Stanisław Węglarczyk in AGH University of Science and Technology for their kind and continuous supports. I also would like to thank Professor Roman Kuziak, in the Institute for Ferrous Metallurgy in Gliwice for his help in the compression tests with Gleeble 3800 for my inverse analysis.

I am deeply grateful for Mr. Hikaru Nomura for his guidance and support.

I would like to say a big thank-you to all of my friends. This thesis definitely would not been completed without them.

I also would like to thank my family for their understanding.

Lastly, I appreciate the financial support of JSPS.

Table of contents

Chapter 1: Introduction

1.1 Social demands and characteristics of Mg alloys 2
1.2 Corrosion characteristics of Mg alloys 5
1.3 Corrosion mitigation strategy of Mg alloys 6
1.4 Coating technique by hot extrusion 8
1.5 Motivation 8
1.6 Organization of this thesis 9
References 11

Chapter 2: Al coating on Mg alloy by hot extrusion

2.1 Introduction 13
2.2 Fabrication of Al-coated Mg alloy 13
2.2.1 Experimental 13
2.2.2 Results and discussion 16
2.3 Corrosion mitigation strategy of Mg alloys 19
2.3.1 Effect of the die angle 19
2.3.2 Effect of the initial thickness of the coating material plate 19
2.4 Corrosion resistance 23
2.4.1 Experimental 23
2.4.2 Results and discussion 23
2.4.2.1 Weight loss measurement 23
2.4.2.2 Electrical potential measurement 24
2.5 Microstructure 26
2.6 Mechanical properties 27
2.6.1 References 27
2.6.2 Results and discussion 28
2.6.2.1 Bending test 28
2.6.2.2 Tensile test 32
2.7 Summary 33
References 34

Chapter 3: Development of flow stress model for the coating process

3.1 Introduction 35
3.2 Direct and inverse problems 36
3.3 Inverse algorithm 37
3.3.1 Experimental investigation 37
3.3.1.1 Experimental method 37
3.3.1.2 Results 38
3.3.2 Numerical simulation as direct problem 40
3.3.3 Inverse analysis 43
3.3.3.1 Step 1 43
3.3.3.2 Constitutive models 45
3.3.3.3 Step 2 46
3.3.4 Verification 47
3.4 Summary 51
References 52

Chapter 4: Investigation of process parameters on the coating behaviors by computer simulation of hot extrusion

4.1 Introduction 54
4.2 Numerical simulation of the coating process 54
4.2.1 Methodology 54
4.2.1.1 Finite element model 54
4.2.1.2 Finite element discretization 55
4.2.1.3 Extrusion model 56
4.2.1.4 Material consistencies 57
4.2.1.5 Contact conditions 58
4.2.2 Model verification 59
4.2.2.1 Methodology 59
4.2.2.2 Results 59
4.3 Effective strain distribution 60
4.4 Sensitivity analysis 61
4.4.1 Methodology 61
4.4.2 Results and discussion 63
4.4.2.1 Coating thickness uniformity 64

4.4.2.2 Average coating thickness 67
4.4.2.3 Velocity field 69
4.5 Summary 71
References 72

Chapter 5: Fabrication of Al-coated Mg alloy sheet by hot forging

5.1 Introduction 73
5.2 Experimental 73
5.3 Al-coated Mg alloy sheet 75
5.3.1 Macroscopic observation 75
5.3.2 Microstructure observation 75
5.4 Corrosion resistance 77
5.4.1 Experimental 77
5.4.2 Results and discussion 77
5.5 Summary 78

Chapter 6: Tensile deformation behavior of Al-coated Mg alloy sheet

6.1 Introduction 79
6.2 Experimental 79
6.3 Results and discussions 79
6.3.1 Deformability of the Al-coated Mg alloy sheet 79
6.3.2 Al coating deformability 80
6.4 Summary 83
References 84

Chapter 7: Deformation mechanism of the Al-coated Mg alloy sheet

7.1 Introduction 85
7.2 Superplasticity evaluation of the Al-coated Mg alloy sheet 85
7.2.1 Strain rate sensitivity index 85
7.2.1.1 Definition 86
7.2.1.2 Strain rate sensitivity index of the Al-coated Mg alloy sheet 87
7.3 Brief review of superplasticity 88

7.3.1 Fundamental characteristics 88
7.3.2 Deformation mechanisms 88
7.3.2.1 Diffusion creep model 88
7.3.2.2 Dislocation motion model 89
7.3.2.3 Grain boundary sliding model 89
7.3.3 Grain boundary sliding with accommodation processes 89
7.3.3.1 Grain boundary sliding with accommodation by dislocation motion 90
7.3.3.2 Grain boundary sliding with accommodation by diffusion creep 90
7.4 Deformation mechanism of the Al-coated Mg alloy sheet 92
7.4.1 Deformation behavior of Mg alloy substrate 92
7.4.1.1 Crystallographic observation 92
7.4.1.2 Fractography 94
7.4.2 Activation energy 96
7.5 Individual deformation behavior of Mg alloy and pure Al 98
7.5.1 Experimental 98
7.5.2 Results 98
7.5.2.1 Mg alloy 98
7.5.2.2 Pure Al 102
7.6 Interface structure 106
7.7 Deformation mechanism of pure Al as coating layer 110
7.7.1 Microstructure and crystallographic observation after tensile tests 110
7.7.2 Microstructure and crystallographic evolution during tensile test 114
7.8 Summary 122
References 123

Chapter 8: Conclusions 128

Appendix

1 Newton-Raphson method 131
1.1 Algorithm 131

1.2 End of the process 132
2 Nelder-Mead simplex method 133
2.1 Algorithm 133
2.2 End of the process 135
References 136

Chapter 1

Introduction

This study deals with Mg alloys as structural materials. The most attractive property of Mg alloys is its low density. Mg alloys also possess many other attractive properties such as good recyclability and high ability of vibration absorption and electromagnetic shielding. Owing to these superior properties, they have attracted a great deal of attention from a number of industries in a broad range of areas. Specifically, Mg alloys capture the attentions of automobile industries, which are ambitious to achieve the weight reduction of vehicles due to the global environmental problems. However, the practical applications of Mg alloys have been limited because of their extremely poor corrosion resistance. Among a number of corrosion mitigation strategies, coating is known as an efficient technique to prevent corrosion. In fact, many coating techniques have been proposed, however, those techniques require complex procedures and appropriate pretreatments due to the high chemical reactivity of Mg alloys. Furthermore, in order to realize the good corrosion protection, coating must be sufficiently uniform, well adhered, pore free and strong enough for the use in the applicable environment. In this way, many severe demands are required to achieve the corrosion protection of Mg alloys, hence development of promising coating techniques has been a critical issue for the further progress in practical application of Mg alloys.

In the preliminary study of the present author, a new Al coating technique for Mg alloys by means of a hot extrusion has been developed. This technique offers possibilities of wide and practical applications of Mg alloys. Thus, the present study mainly focuses on the development and characterization of the Al-coated Mg alloy. In this chapter, the social demands of Mg alloys are specifically described and by characterizing the Mg alloys, the need for corrosion protection is demonstrated. The early-developed corrosion protection techniques are summarized and remaining problems are pointed out. Lastly, the purposes of the present study are stated.

1.1 Social demands and characteristics of Mg alloys

Mg alloys are the lightest materials among practical alloys for structural use [1.1]. The density of Mg at 293 K is 1.738 g/cm^3, which is two-thirds of that of Al (2.7 g/cm^3) and quarter of that of Fe (7.86 g/cm^3) [1.1-1.3]. Mg alloys also possess many other attractive properties such as good recyclability, damping capacity, machinability, high ability of vibration absorption and electromagnetic shielding [1.3-1.6]. Furthermore, Mg is 8th most abundant element in the outer layer of the earth and the sea water contains Mg of approximately 1.3 kg/m^3 (0.3 mass%) [1.2, 1.4]. Owing to those superior properties and the rich deposit, Mg alloys have attracted a number of industries and have been utilized in a broad range of areas for instance in hobby equipment i.e. bicycle frames and sporting equipment and also in communication engineering such as cases of portable electronic devices like laptops and cellphones as presented in Fig. 1.1 [1.5, 1.7].

Recently, emissions of the greenhouse gases, including carbon dioxide (CO_2), chlorofluorocarbons (CFCs), methane (CH_4) and nitrous oxide (N_2O), have gained wide range of attentions. Since the emissions of greenhouse gases have been drastically increasing every year, the immediate action to prevent the further growth in those emissions is urgently required to protect the global environment. It is known that the transport sector is one of the major sources of CO_2 emissions. In fact, the transport sector owns 25 % of the total CO_2 emissions, and specifically, the road transportation owns 75 % of the total emission from the transport sector [1.8]. However, the number of vehicles has been growing and this leads to a further increase of the greenhouse gas emissions. Thus, global policies and legislations on the vehicle weight restriction have been implemented, not only for the aforementioned problem, but also for securing the energy supply, considering the exhaustion of fossil fuels. Accordingly, the light Mg alloys currently capture the attention of automobile industries, which are ambitious to achieve the weight reduction of vehicles. Actually, the applications of Mg alloys into the automotive components have been widely developing, as can be seen from the examples shown in Fig. 1.2.

Basically, the main metal components of automobile components are steel and Al alloys [1.9]. As mentioned above, since Mg is much lighter than these metal materials, the replacement of these materials with Mg alloys can lead to a significant weight reduction. For example, in the automotive applications in body panels, Mg sheet metal can offer a weight saving of as much as 62 % over steel [1.9]. Moreover, it has been estimated that 10 % weight reduction from a total weight of vehicle can improve the fuel economy by 5 to 7 %, namely, CO_2 can be eliminated by about 20 kg from every kilogram weight reduction of a vehicle [1.10].

Consequently, Mg is considered as a key material for the great development of the global industries in technical and environmental point of view and social expectations have been raising for its potential.

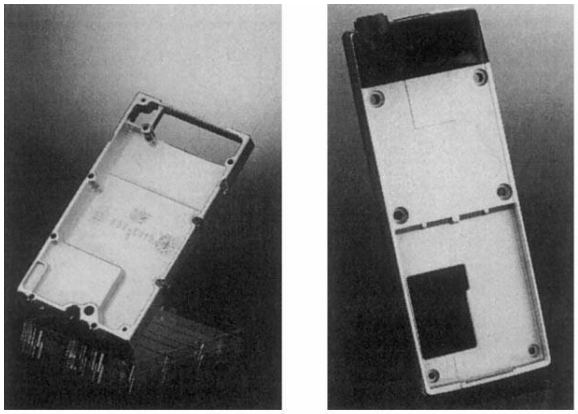

Screen housing　　Units for mobile phone

Fig. 1.1 Examples of the Mg alloy applications [1.5].

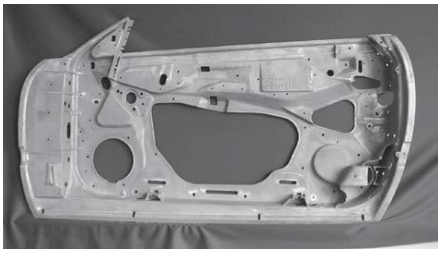

Inner door frame

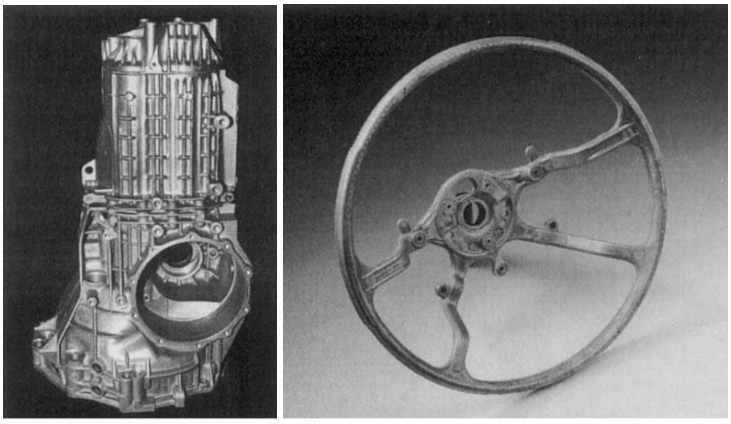

Gear box housing　　Steering wheel frame

Fig. 1.2 Examples of the Mg alloy applications in automobile components [1.5, 1.11].

Although the widespread applications of Mg alloys have been expected as mentioned above, actually, the practical applications of Mg alloys still have been limited because of their insufficient mechanical strength and poor resistance to creep and corrosion [1.3, 1.4, 1.9].

Basically those drawbacks have been suppressed and ameliorated by alloying. It is well known that the alloying technique can significantly improve the strength of Mg especially with Al, Mn, Zn, Zr and Th [1.1] and also, the creep resistance with e.g. La, Ca and Ce [1.9, 1.12]. It has been also reported that alloying of some specific elements such as Mn, Er, Ce, La and Nd improves the corrosion resistance of Mg alloys [1.12], however, alloying technique generally did not offer dramatic improvement with respect to the corrosion resistance, in contrast to the great improvements in mechanical strength and creep resistance. Figure 1.3 depicts the practical corrosion potentials of various metals and alloys [1.13, 1.14]. As is clear from the figure, although the corrosion resistance of Mg is only slightly improved by alloying, the practical corrosion potentials are still extremely low compared to other metal materials.

Consequently, it is clear that the development of the corrosion protection strategy is a critical issue for Mg alloys. In order to develop and advance the corrosion protection, it is important to understand the basic corrosion characteristics and have a practical corrosion mitigation strategy. Thus, firstly the corrosion characteristics of Mg alloys are explained and subsequently, the early-developed countermeasures against the corrosion are given in the following sections.

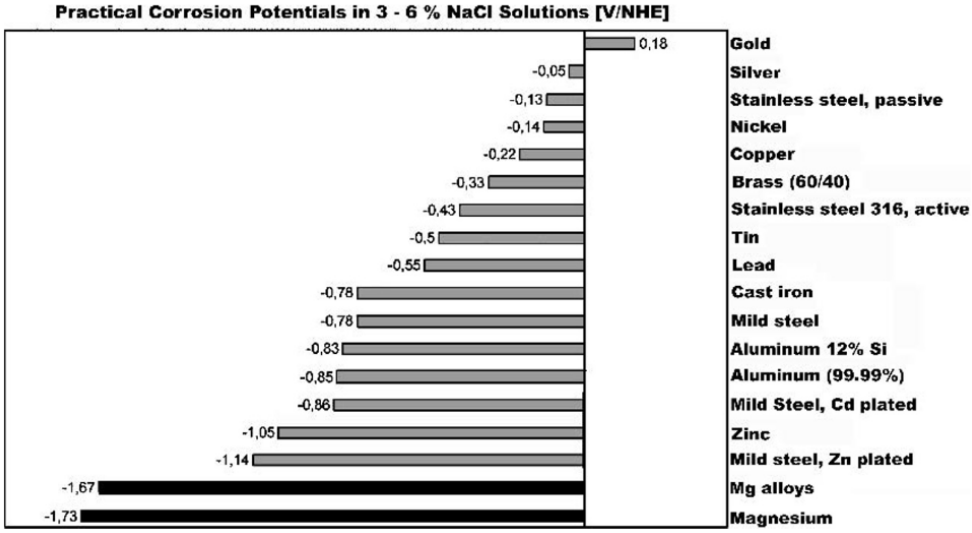

Fig. 1.3 Practical corrosion potentials of various metals and alloys measured in 3-6 % NaCl solution [1.13, 1.14].

1.2 Corrosion characteristics of Mg alloys

Mg and Mg alloys are often considered as severe corrosive metals because of their low standard electrode potential as shown in Table 1.1 [1.15]. Actually, however, there is no appreciable corrosion of Mg near room temperature unless water is present [1.16]. The reaction of Mg with water can be described by the following reaction formula;

$$\mathrm{Mg} + 2\mathrm{H_2O} = \mathrm{Mg(OH)_2} + \mathrm{H_2}$$

From this formula, it is clear that the $Mg(OH)_2$ forms when Mg contacts with water under the neural or basic environment. This hydroxide is stable in the basic range of pH values, therefore, in the alkaline environments, a $Mg(OH)_2$ film can offer considerable protection to the Mg substrate, though it is not as effective as Al_2O_3 on Al substrate [1.17]. However, on the other hand, Mg is subjected to dissolution by most acids. Weathering to acidic environments, the hydroxide layer loses their protective potential by conversion to the soluble crystalline, which is easily washed away and causes the re-exposing of the surface [1.17]. Therefore, actually, Mg dissolves as rapidly as the acid can diffuse to its surface, thus, even the atmosphere contains acid gases like CO_2 can also significantly corrode Mg [1.17]. That is, Mg is significantly eroded by serial absorption of moisture containing CO_2

from the atmosphere in the actual environment [1.16]. Therefore, considering the practical applications in the actual environment, corrosion protection techniques for Mg alloys are absolutely necessary.

Table 1.1 Standard equilibrium potentials of typical metals in aqueous solution [1.15].

Electrode	Reaction	Potential, V
Li, Li^+	$Li^+ + e^- \rightarrow Li$	−3.02
K, K^+	$K^+ + e^- \rightarrow K$	−2.92
Na, Na^+	$Na^+ + e^- \rightarrow Na$	−2.71
Mg, Mg^{2+}	$Mg^{2+} + e^- \rightarrow Mg$	−2.37
Al, Al^{3+}	$Al^{3+} + e^- \rightarrow Al$	−1.71
Zn, Zn^{2+}	$Zn^{2+} + e^- \rightarrow Zn$	−0.76
Fe, Fe^{2+}	$Fe^{2+} + e^- \rightarrow Fe$	−0.44
Cd, Cd^{2+}	$Cd^{2+} + e^- \rightarrow Cd$	−0.40
Ni, Ni^{2+}	$Ni^{2+} + e^- \rightarrow Ni$	−0.24
Sn, Sn^{2+}	$Sn^{2+} + e^- \rightarrow Sn$	−0.14
Cu, Cu^{2+}	$Cu^{2+} + e^- \rightarrow Cu$	0.34
Ag, Ag^+	$Ag^+ + e^- \rightarrow Ag$	0.80

1.3 Corrosion mitigation strategy of Mg alloys

In order to protect the Mg alloys from corrosion, a number of strategies have been proposed such as alloying, associated with the microstructure control, elimination of bad design, flux inclusions, surface contamination or galvanic couples, and coating and cladding techniques [1.7, 1.5]. As already mentioned above, alloying technique slightly improves the corrosion resistance of Mg alloys, and even worse, it is known that improper selection of the alloying element can deteriorate the corrosion resistance. Also, even though the aforementioned harmful sources are eliminated, as long as the Mg alloys are directly exposed to corrosive sources, superior corrosion resistance can hardly be expected. On the other hand, coating and cladding techniques are known as efficient techniques to improve the corrosion resistance of Mg alloys because the coating and cladding can work as a barrier and isolate the substrate from the outer corrosive environment [1.18]. In fact, a great deal of coating techniques has been proposed for Mg alloys. The widely-used techniques are listed and their advantages and disadvantages are summarized in Table 1.2 [1.4, 1.6, 1.16, 1.18]. All the techniques have the strong and weak points and therefore practically, a careful selection of the technique is required with

considering applicable environment, required surface morphology and components design. Moreover, those techniques require complex procedures and appropriate pretreatments [1.18]. These challenges are originating from the presence of surface oxide or hydroxide layer attributable to the high reactivity of Mg alloys as was shown in Table 1.1 [1.1]. As mentioned above, as soon as Mg is exposed to air or water, an oxide or hydroxide layer forms on the surface, and it interferes the good bonding between the coating and Mg surface. Therefore, in order to achieve the good bonding interface, the surface layer elimination and the continued pretreatment or additional procedures are of great importance. Furthermore, to realize the excellent corrosion resistance, coating must be uniform in thickness, well adhered, pore free and strong enough for the use in an applicable environment [1.18]. Since such a lot of severe demands are required to achieve the corrosion protection of Mg alloys, promising coating or cladding techniques have been still anticipated for the further development and applications of Mg alloys.

Table 1.2 Corrosion mitigation techniques [1.4, 1.6, 1.16, 1.18].

Technique	Advantage	Disadvantage
electro/electroless plating	• Good appearance • Good corrosion resistance • Good abrasion and wear properties • Low cost	• Difficult pretreatment • Toxic chemicals • Difficult control of the electrochemical inhomogeneity
anodizing	• Enable to color • Excellent pre-surface for other subsequent technique • Low cost	• Difficult pretreatment • Brittle coating • Insufficient mechanical strength
chemical conversion coatings	• Good corrosion resistance with self-healing characteristics • Low cost	• Toxicity of the treatment solutions
gas-phase deposition	• Environment friendly	• High capital cost • Requirement of sealing and mechanical finishing • Requirement of pretreatment
laser surface alloying/cladding	• Enable to treat complex geometries • Low operation cost • Ease to automation • Rapid processing	• Undesirable interfacial reactions • High capital cost • Difficult to uniformly coat on the complex geometries
organic/polymer coatings	• Good corrosion resistance • Good abrasion and wear properties	• Difficult pretreatment
diffusion coatings	• High adhesion strength • Good wear properties	• Negative effect on the microstructure and mechanical properties of the substrate

1.4 Coating technique by hot extrusion

In the preliminary study of the author, a new coating technique for Mg alloys has been developed by using the hot extrusion [1.19]. For the coating material, pure Al was selected because of its lightness and superior corrosion resistance [1.20]. In the technique, Al and Mg alloys should be plastically deformed in contact with each other at high pressures and temperatures, which can destroy the aforementioned problematic oxide layer and realize the continuous contact between the newly-born surfaces of the metals, thus yielding the strong bonding between both the metals. Furthermore, since the extrusion is a common conventional technique, this technique does not require new equipment investment. Moreover, owing to the severe plastic deformation by the hot extrusion, grain refinement can be expected, which leads up to the strength improvement. The details of this technique are given in Chapter 2.

Although the Al coating on Mg alloy has been achieved in the preliminary study of the present author, there is still a considerable lack of important information as follows.

Firstly, as mentioned in the section 1.3, in order to realize the sufficient corrosion protection, the coating thickness should be uniform. In the preliminary study of the present author, the uniform coating thickness has been achieved. However, it is still unclear what process parameter is predominant in the coating thickness uniformity and there should be an absolute indication for the coating thickness uniformity when considering the practical applications. Therefore, the significance of the extrusion process parameters in the coating thickness uniformity should be indicated. Secondly, although Mg alloys are often used industrially in a sheet form rather than bars or plates, the preliminary study has dealt with only bars and plates. Therefore, the feasibility of sheet fabrication based on the present technique should be clarified.

Consequently, as just described, there is still much need for a further research. Thus, the present study is carried out. The motivation for the present study is described in the next section.

1.5 Motivation

As mentioned above, the new Al coating technique for Mg alloys has been developed. In order to demonstrate the possibility of wide and practical use of Mg alloys, the main purpose of this study has been set as development and characterization of the Al-coated Mg alloy by the present coating technique. Several issues are tackled in this study by the multi-disciplinary approach with both experimental and numerical methods.

1.6 Organization of this thesis

This thesis consists of 8 chapters and the organization is described below.

In Chapter 2, the author's preliminary study, namely, the Al coating technique for Mg alloys by hot extrusion is explained and the chemical and mechanical properties of the produced Al-coated Mg alloy are illustrated.

When considering development of the coating technique, the precise control of the thickness of Al coating is the important issue. However, the coating thickness should be dependent on many process parameters and empirical elucidation of such dependencies requires a considerable amount of time and energy. Therefore, in order to clarify the dependencies of the process parameters on the coating thickness, the sensitivity analysis is performed with the help of numerical simulations.

In numerical simulations, flow stress models have a considerable influence on the accuracy of the simulation by describing the rheological properties of the materials. In Chapter 3, therefore, the flow stress model of the focused Mg alloy is developed for the numerical simulation of the coating process by a combination of the inverse analysis and optimization process. The algorithm of the inverse analysis and optimization process are firstly explained and then, the optimal flow stress model is determined by the comparative verification with the experimental and simulated results.

In Chapter 4, the effects of extrusion parameters on the coating thickness uniformity are evaluated by the sensitivity analysis with data collected with the numerical simulation, implemented with the above-developed flow stress model. Firstly, the numerical simulation of the coating process is verified and the effects of the following five parameters are evaluated; (1) initial thickness of the coating material plate, (2) extrusion temperature, (3) ram speed, (4) die angle and (5) the strength of core and coating materials.

Chapter 5 focuses on the feasibility of fabrication of the Al-coated Mg alloy sheet with a view to the practical application of the present coating technique. The feasibility is estimated by the investigation of the cross section and the corrosion resistance of the sheet.

In Chapter 6, the tensile properties of the Al-coated Mg alloy sheet are investigated because the deformability and mechanical properties of the sheet are of primary importance for the practical applications of the sheet. The tensile tests are performed and

the bondability and deformability of the Al coating are investigated with a special attention.

Chapter 7 focuses on the deformation mechanism of the Al-coated Mg alloy sheet during the tensile test. Careful discussions have been made by means of the microstructure and crystallographic observations. Consequently, the deformation behaviors of both Mg alloy substrate and Al coating layer in the sheet have been explained in detail.

Finally, the contributions and future perspectives of the present study are summarized in Chapter 8.

References

[1.1] M.K. Kulekci, Magnesium and its alloys applications in automotive industry. *Int. J. Adv. Manuf. Technol.* **39** (2008) 851-865.

[1.2] H.E. Friedrich, B.L. Mordike, *Magnesium Technology - Metallurgy, Design Data, Applications*. Springer-Verlag Berlin Heidelberg, 2006.

[1.3] H. Haferkamp, R. Boehm, U. Holzkamp, C. Jaschik, V. Kaese, M. Niemeyer, Alloy development, processing and applications in magnesium lithium alloys. *Mater. Trans.* **42** (2001) 1160-1166.

[1.4] A. Singh, S.P. Harimkar, Laser Surface Engineering of Magnesium Alloys: A Review. *JOM* **64** (2012) 716-733.

[1.5] B.L. Mordike, T. Ebert, Magnesium – Properties – applications – potential. *Mater. Sci. Eng. A* **302** (2001) 37-45.

[1.6] G.-L. Song (Ed.) Corrosion prevention of magnesium alloys. Woodhead Pub., Cambridge, UK, 2013.

[1.7] R.G. Hu, S. Zhang, J.F. Bu, C.J. Lin, G.L. Song, Recent progress in corrosion protection of magnesium alloys by organic coatings. *Progress in Organic Coatings.* **73** (2012) 129-141.

[1.8] R. Kok, J.A. Annema, B. van Wee, Cost-effectiveness of greenhouse gas mitigation in transport: A review of methodological approaches and their impact. *Energy Policy* **39** (2011) 7776-7793.

[1.9] A.A. Luo, Magnesium: Current and potential automotive applications. *JOM* **54** (2002) 42-48.

[1.10] E. Ghassemieh, Materials in Automotive Application, State of the Art and Prospects, New Trends and Developments in Automotive Industry, M. Chiaberge (Ed.), In Tech, 2011.

[1.11] C. Blawert, N. Hort, K.U. Kainer, Automotive applications of magnesium and its alloys. *Trans. Indian Inst. Met.* **57** (2004) 397-408.

[1.12] Y. Ding, C. Wen, P. Hodgson, Y. Li, Effects of alloying elements on the corrosion behavior and biocompatibility of biodegradable magnesium alloys: a review. *J. Mater. Chem. B* **2** (2014) 1912-1933.

[1.13] G.L. Song, A. Atrens, Corrosion mechanisms of magnesium alloys. *Adv. Eng. Mater.* **1** (1999) 11-33.

[1.14] E. Ghali, W. Dietzel, K.U. Kainer, General and localized corrosion of magnesium alloys: a critical review. *J. Mater. Eng. Perform.* **22** (2013) 2875-2891.

[1.15] B.A. Shaw, Corrosion resistance of magnesium alloys. in: ASM Handbook, **13A**

Corrosion: Fundamentals, Testing, and Protection, 2003.

[1.16] H.P. Godard, W.B. Jepson, M.R. Bothwell, R.L. Kane, The corrosion of light metals. John Wiley & Sons, Inc., 1967.

[1.17] W.A. Ferrando, Review of corrosion and corrosion control of magnesium alloys and composites. *J. Mater. Eng.* **11** (1989) 299-313.

[1.18] J.E. Gray, B. Luan, Protective coatings on magnesium and its alloys – a critical review. *J. Alloy. Compd.* **336** (2002) 88-113.

[1.19] T. Tokunaga, K. Matsuura, M. Ohno, Aluminum coating on magnesium-based alloy by hot extrusion and its characteristics. *Mater. Trans.* **53** (2012) 1034-1041.

[1.20] B.S. DeForce, T.J. Eden, J.K. Potter, Cold Spray Al-5% Mg Coatings for the Corrosion Protection of Magnesium Alloys. *J. Thermal Spray Technology* **20** (2011) 1352-1358.

Chapter 2

Al coating on Mg alloy by hot extrusion

2.1 Introduction

As mentioned in Chapter 1, a new Al coating technique for Mg alloys was developed by using a hot extrusion technique in the author's preliminary study [2.1]. In this chapter, the coating technique is explained in detail and the characteristics of the fabricated Al-coated Mg alloy are also demonstrated.

2.2 Fabrication of Al-coated Mg alloy

2.2.1 Experimental

Figure 2.1 illustrates the schematic drawing of the experimental equipment and materials for the present coating technique. In the preliminary experiments, it was found that the direct extrusion requires such a high load that is beyond the capacity of our press machine. Therefore, in the present study, an indirect extrusion process was adopted, which requires less power, because no friction between the billet and the container wall is required. For the substrate material, a commercial extruded round bar of AZ80 Mg alloy, having a diameter of 42 mm, was used. The chemical composition of the alloy is shown in Table 2.1. The alloy was cut into a billet with a thickness of 30 mm and subsequently, it was solution-treated at 673 K for 5 hours, and then aging-treated at 623 K for 1 hour in order for the generation of the precipitations which can retard the grain coarsening during the hot extrusion. While as for the coating material, an industrially pure Al (99. 7 % purity) ingot, having a diameter of 45 mm, was cut into a disc shape with a thickness of 3 mm and subjected to the extrusion. Figure 2.2 shows the schematic drawing of the die used in this study. The dies angle, θ, in Fig. 2 (d) was varied from 90 ^{o} to 120 ^{o}.

As illustrated in Fig. 2.2, the Al plate was installed between the Mg alloy billet and the die. The die and ram were preheated at 523 K before setting. All the materials inside the container were heated to the extrusion temperature of 583 K at a heating rate of 0.033 K/sec and then, the materials were extruded backward by loading on the ram. The ram speed was

about 0.023 mm/sec and the extrusion reduction ratio was 92 %. In the present study, the effect of the die angle on the reduction ratio is not considered.

Table 2.1 Chemical composition of the AZ80 Mg alloy.

Al	Zn	Mn	Fe	Ni	Cu	Si	Ca	Sn	Others Total (max)	Mg
8.2	0.56	0.44	.0001	.0006	.0008	0.013	0.001	<0.001	0.30	Bal.

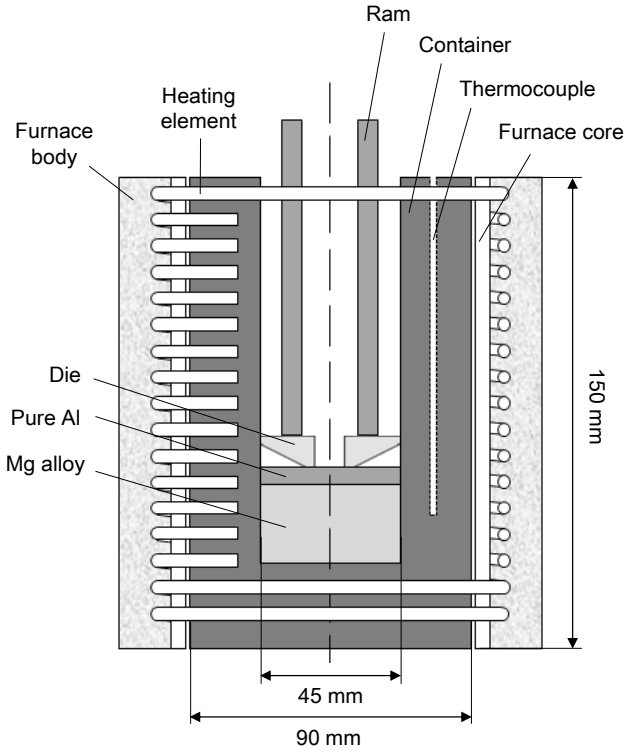

Fig. 2.1 Schematic drawing of equipment and materials for the extrusion

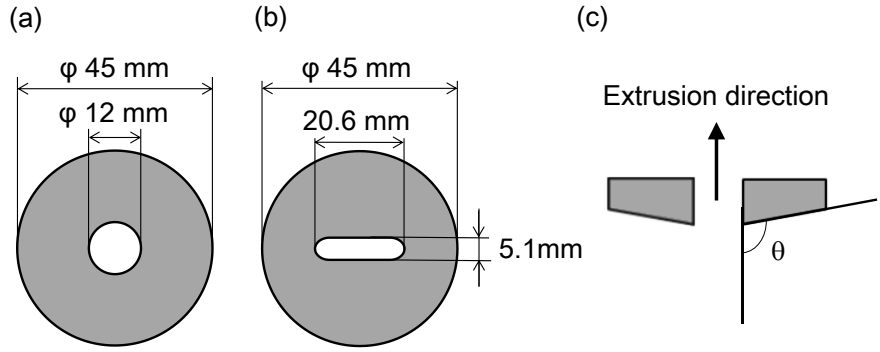

Fig. 2.2 Schematic drawings of the dies; (a) overhead view of a die, (b) overhead view of a die used for specimen fabrication of bending and tensile tests and (c) cross section of the die.

2.2.2 Results and discussion

After the extrusion, the extrudate was cut every 10 mm from the tip of the extrudate and the cross section was observed. Figure 2.3 depicts the cross section of the extrudate. It is clear that the Mg alloy surface is fully covered with the Al coating. The coating of the Mg alloy with Al was successful regardless of the die angles.

The apparent density was measured with the Archimedes method using pure water. The temperature of the water was 23.7 ^{o}C and the density was measured 5 times for each of 3 samples. Consequently, the apparent density of the Al-coated Mg alloy was 1.90 g/cm^3, which is about 70 % of Al (2.70 g/cm^3).

Figure 2.4 depicts the Mg/Al interface. No cracks or debondings were observed, however, a newly-formed intermetallic compound (IMC) was found at the interface. In order to reveal the chemical composition of IMC, the electron probe micro analysis (EPMA) was performed. The measurement was performed continuously every 0.2 μm with the spot size of 1.0 μm along a line crossing the interface. The elements being of interest were Mg, Al, Zn, Mn and O. Figure 2.5 shows the analysis results. Since the concentrations of Zn, Mn and O were significantly low, the results of these elements are not presented in the figure. From the analysis, it was found that the focused IMC phase consists of Al and Mg in a proportion of 3:2. From the phase diagram shown in Fig. 2.6, this IMC phase can be recognized as Al_3Mg_2. Additionally, the average thickness of the IMC layer was measured and it was approximately 3.5 μm.

Furthermore, in order to investigate the growth rate of the IMC layer at elevated temperatures, the extrudate was heated and the thickness change of the IMC layer was investigated. The heating temperature was set at 473, 583 and 623 K.

The thickness change of the IMC layer after heating is shown in Fig. 2.7. It was found that IMC grows faster at higher temperatures, but growth rate at 473 K is negligibly low. Additionally, two different IMCs were found after heating. EPMA revealed that those phases are Al_3Mg_2 and $Al_{12}Mg_{17}$ and the former IMC layer was thicker than the latter.

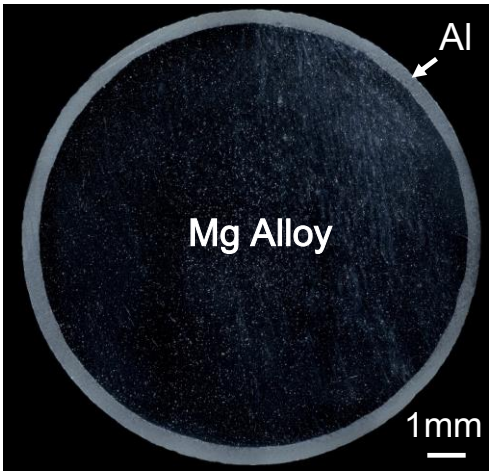

Fig. 2.3 Cross-section of the extrudate, produced with a die having an angle of 110 °.

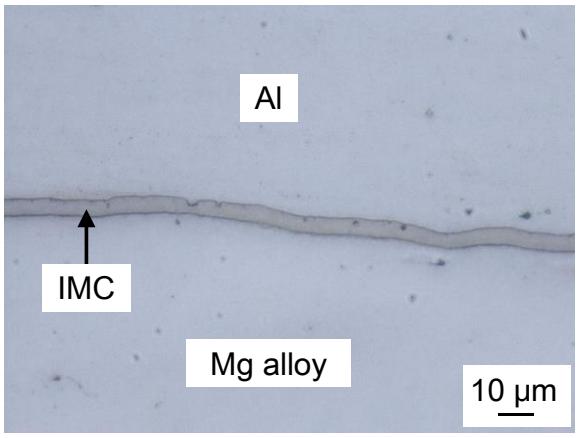

Fig. 2.4 Mg/Al interface in the extrudate produced with a die having an angle of 110 °.

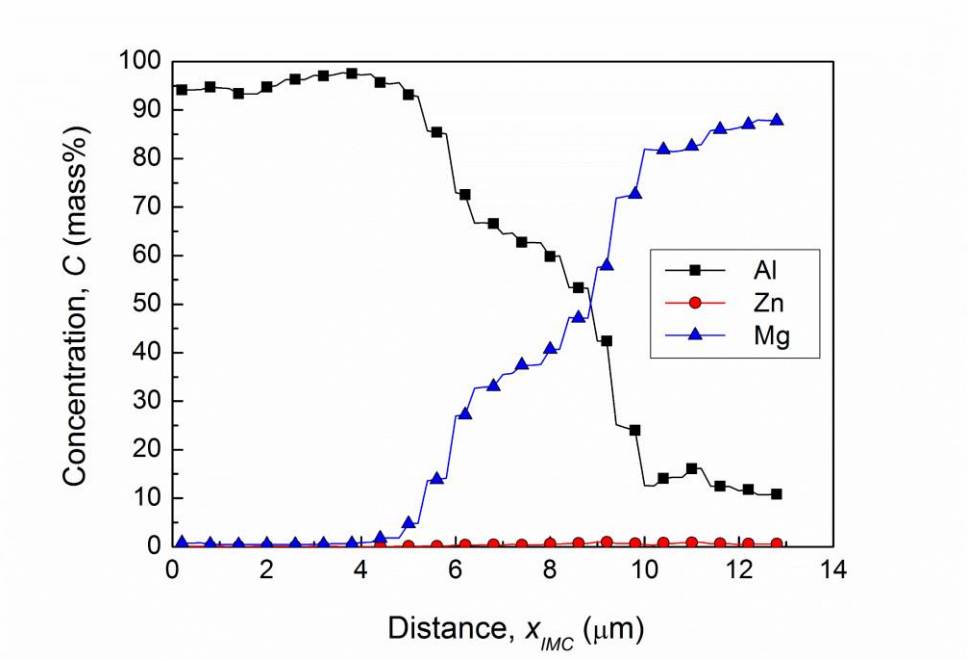

Fig. 2.5 Results of EPMA of IMC layer.

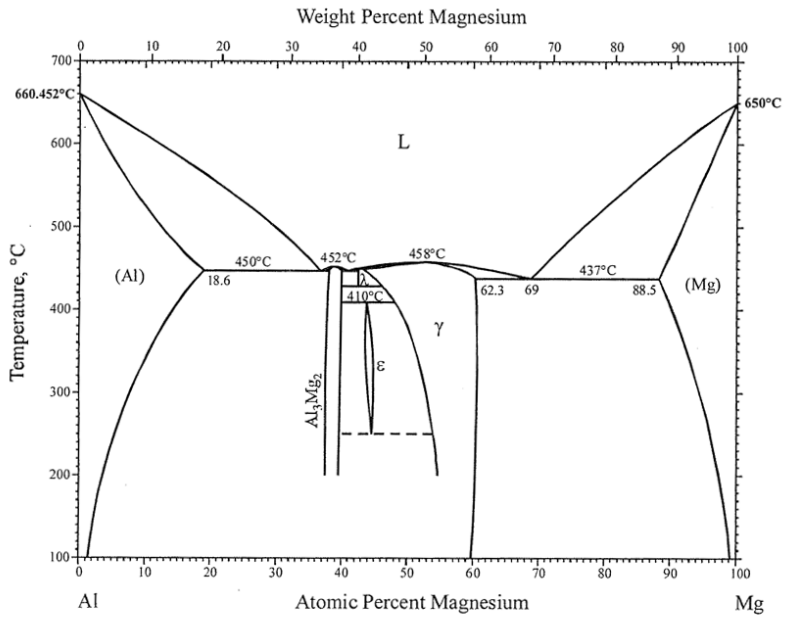

Fig. 2.6 Mg-Al binary phase diagram [2.2].

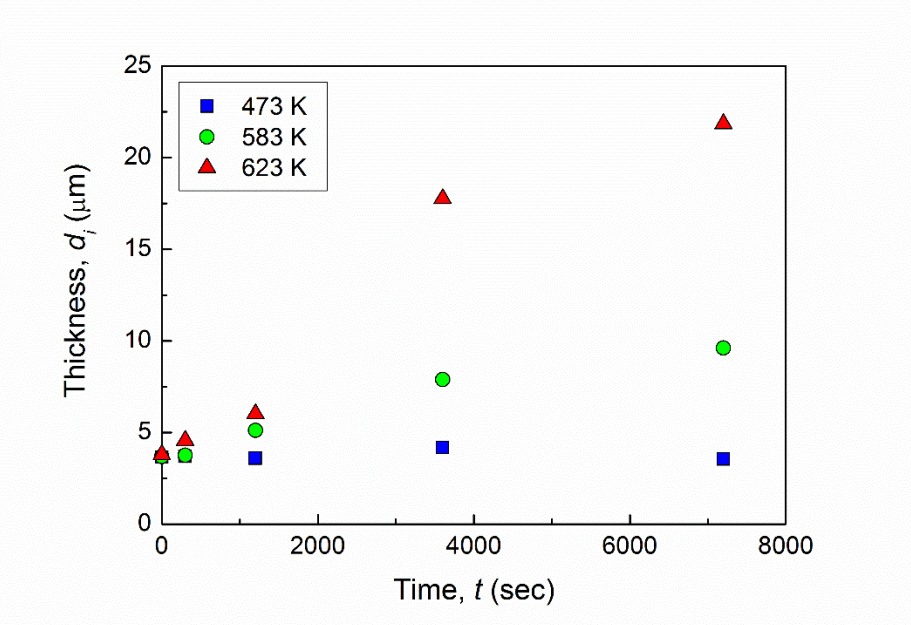

Fig. 2.7 Thickness change of IMC layer during heating at various temperatures.

2.3 Control of coating thickness

As was mentioned in Chapter 1, the precise control of the coating thickness is one of the most important issues in the present Al coating technique. Thus, in this section, the coating thickness uniformity is investigated under various conditions and the brief direction to the uniform thickness coating is indicated.

2.3.1 Effect of the die angle

The extrudate was sectioned every 10 mm in the extrusion direction and Al coating thickness was measured at 20 different arbitrary positions in each cross section and the average coating thickness was calculated.

Figure 2.8 illustrates the thickness change of the Al coating layer with respect to the distance from tip of the extrudate, produced with various die angles. When the die angle is small (θ = 90, 100 ^{o}), the coating thickness decreases with the distance, while when the die angle is large (θ = 120 ^{o}), the coating thickness gradually increases with the distance. Notably, when the die angle is 110 ^{o}, the change in coating thickness is very small in through a whole extrudate. These results indicate that the coating thickness uniformity can be significantly controlled by changing the die angle.

2.3.2 Effect of the initial thickness of the coating material plate

It was considered that the initial thickness of the coating material plate put on the billet material should affect the thickness of the coating layer of the extrudate. In order to investigate the effect of the initial thickness of the coating material plate on the coating thickness uniformity, the coating thickness of the extrudate produced with the variety of initial thickness of coating material plate was investigated. The initial thickness was set at 1, 2, 3 and 6 mm for a die angle of 100 ^{o}, while the initial thickness was set at 3 and 6 mm for die angles of 110 and 120 ^{o}.

Figure 2.9 illustrates the effects of the initial thickness of the coating material plate on the coating thickness for a die angle of 100 ^{o}. When the 1 mm-thick coating material plate was used, the coating was partially broken, which means that 1 mm is too thin to produce a good coating layer. However, there is no such defect in other initial thickness conditions. When the plate thickness was 3 mm, the coating thickness gradually decreases as extrusion

proceeds, while in the case of the initial thickness of 2 mm, the coating thickness is almost uniform through whole extrudate. Accordingly, it can be said that when the die angle is 100^{o}, the optimal initial thickness of the coating material plate is 2 mm.

Figures 2.10 and 2.11 illustrate the effects of the initial thickness of the coating material plate for die angles of 110 and 120 ^{o}, respectively. The coating thicknesses significantly increase when the plate thickness are doubled from 1 to 2 mm and from 3 to 6 mm for 110 and 120 ^{o}, respectively. When the die angle is 110 ^{o}, the coating thickness is almost uniform in both initial thickness conditions. However, when the die angle is 120 ^{o}, the perfectly uniform thickness coating is not achieved. When the plate thickness is 3 mm, the coating thickness gradually increases as extrusion proceeds, and when the plate thickness is 6 mm, the coating thickness is quite uniform from the middle part of the extrudate, however, still the thickness increases slightly as extrusion proceeds. Consequently, it was found that the coating thickness is significantly influenced by the initial thickness of the coating material plate and it seems that the larger the die angle is, the thicker coating material plate is necessary to obtain the uniform thickness coating.

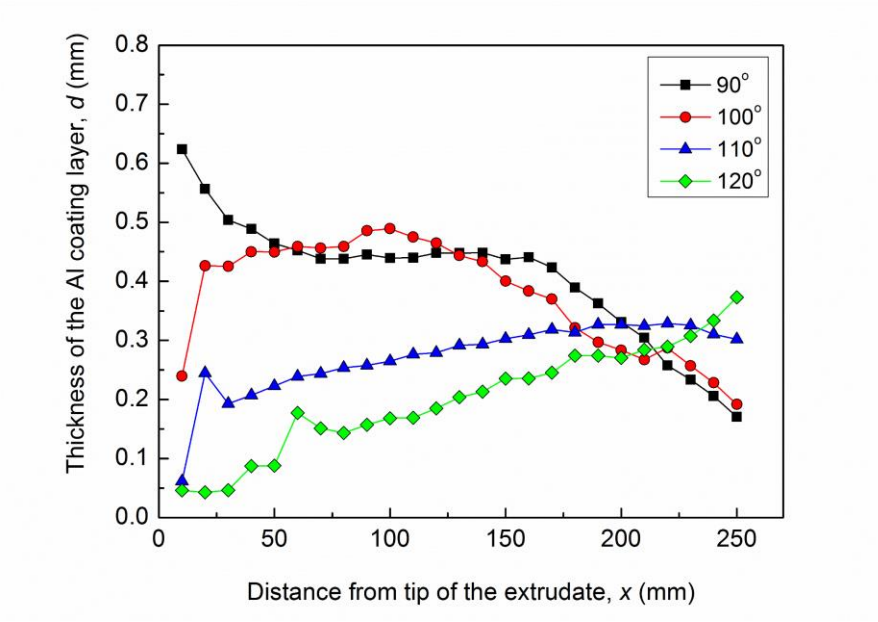

Fig. 2.8 Change of Al coating thickness with respect to the distance from tip of extrudates produced with dies having various die angles.

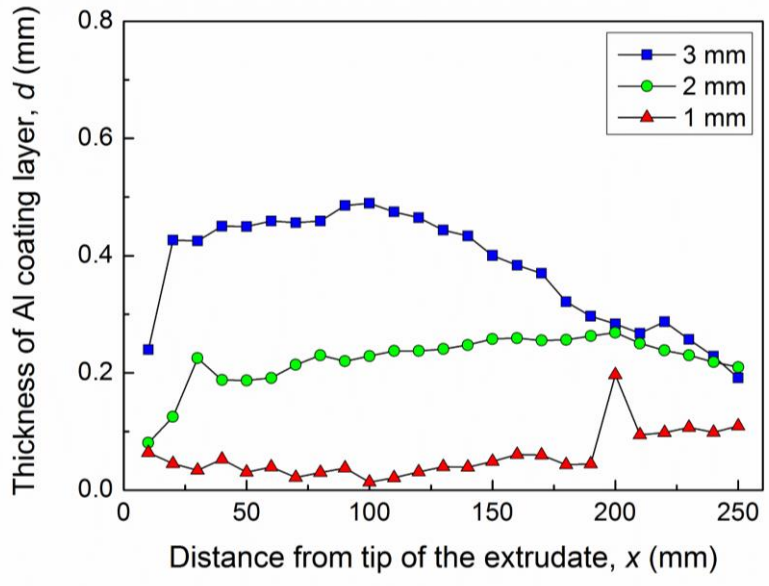

Fig. 2.9 Effect of the initial thickness of Al plate on the coating thickness (θ = 100 °).

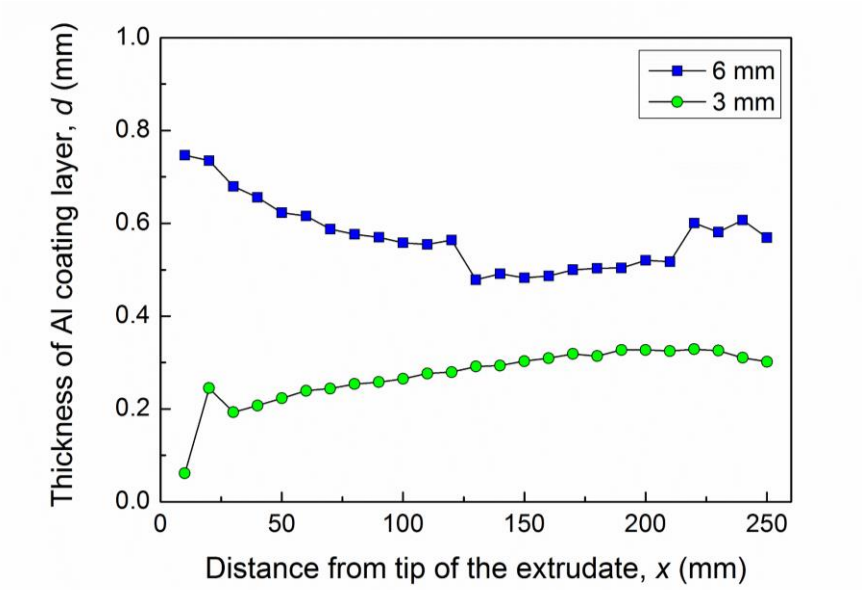

Fig. 2.10 Effect of the initial thickness of Al plate on the coating thickness (θ = 110 ^{o}).

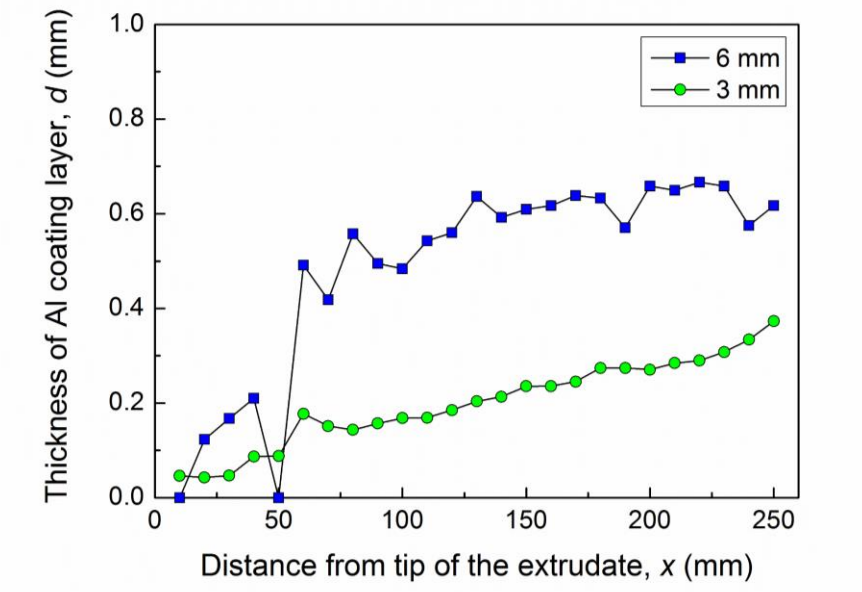

Fig. 2.11 Effect of the initial thickness of Al plate on the coating thickness (θ = 120 ^{o}).

2.4 Corrosion resistance

2.4.1 Experimental

The corrosion resistance of the produced Al-coated Mg alloy extrudate was evaluated. For the evaluation, weight loss per unit area of the extrudate was measured in a 5.0 mass%HCl aqueous solution at room temperature. The cross sections of the extrudate were covered with an epoxy adhesive in order for only the side surface to be exposed to the HCl aqueous solution. For comparison, the Mg alloy and Al used in this study as the billet and the coating material were also subjected to the corrosion test. The surfaces of the Mg alloy and Al samples mechanically polished with water-proof polishing paper up to #1500 in order to remove the surface oxide layer prior to the test. The surfaces of those samples were also covered partially to expose only almost the same area as that of the extrudate.

For further investigation, the corrosion resistance was additionally evaluated by measuring the electric potential. Since even a tiny defect of the Al coating such as a microcrack can be detected as a significant change in the electric potential, this investigation can evaluate the perfection of the coating strictly and accurately. The test was performed in a 3 mass%NaCl aqueous solution at room temperature. The cross-sectional surfaces of the extrudate were covered with the epoxy adhesive as explained above. A KCl agar salt bridge was used for the seclusion of the anode and cathode and an Ag/AgCl system was used for the reference electrode. The Mg alloy and Al samples were also subjected to this test for 30 minutes, while the Al-coated Mg alloy extrudate was tested for four days to investigate the durability of the coating. The data were recorded potentiostatically every 1 second.

2.4.2 Results and discussions

2.4.2.1 Weight loss measurement

Figure 2.12 exhibits the weight losses of the samples in the HCl aqueous solution with respect to immersion time. The Mg alloy significantly dissolved soon after immersion, while the Al-coated Mg alloy extrudate did not dissolve at all, which is exactly same as the behavior of Al. It is observed in the figure that the Al slightly exhibited negative value, the reason of which is considered to be the weight gain due to absorption of the aqueous solution by the epoxy adhesive.

2.4.2.2 Electrical potential measurement

Figure 2.13 illustrates the results of the electric potential measurements. The electric potential of the Al and Mg alloy used in this study were approximately 0.7 and 1.6 V, respectively. On the other hand, the extrudate indicates about 0.7 V in the potential which is the same level as the pure Al and the potential was almost constant for during the immersion period of four days, as shown in fig. 2.13. The slight oscillation of the potential data is because of the surface change, which is attributable to the reaction between the sample surface and the solution. This result clearly indicates that the Mg alloy was perfectly covered with the Al coating.

Consequently, it was indicated that the present technique based on hot extrusion provides the perfect Al coating on Mg alloy and that significant improvement in the corrosion resistance of the Mg alloy can be achieved with the present technique.

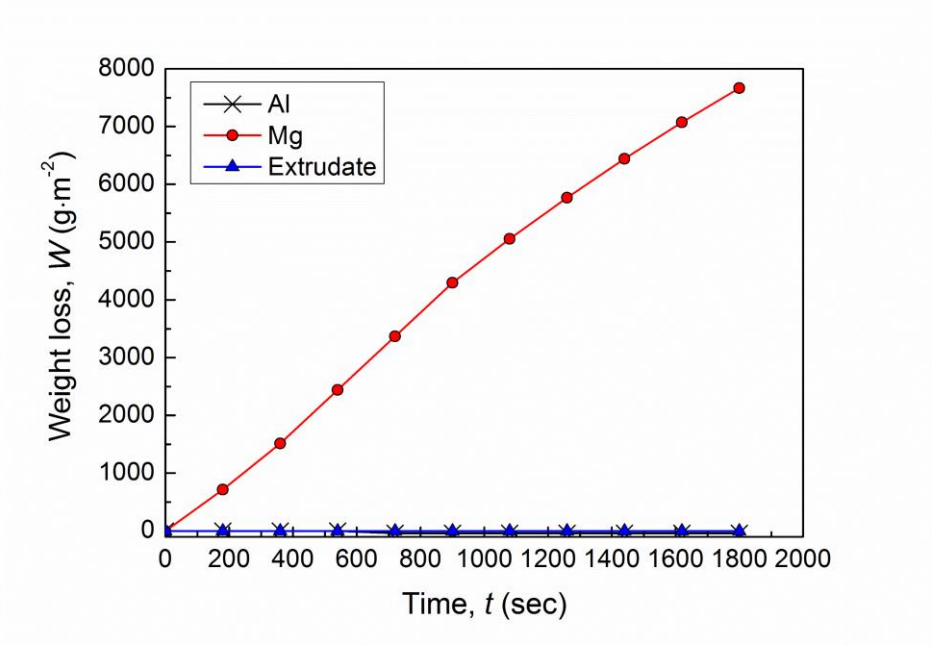

Fig. 2.12 Weight loss versus immersion time in 5.0 mass% HCl aqueous solution at room temperature.

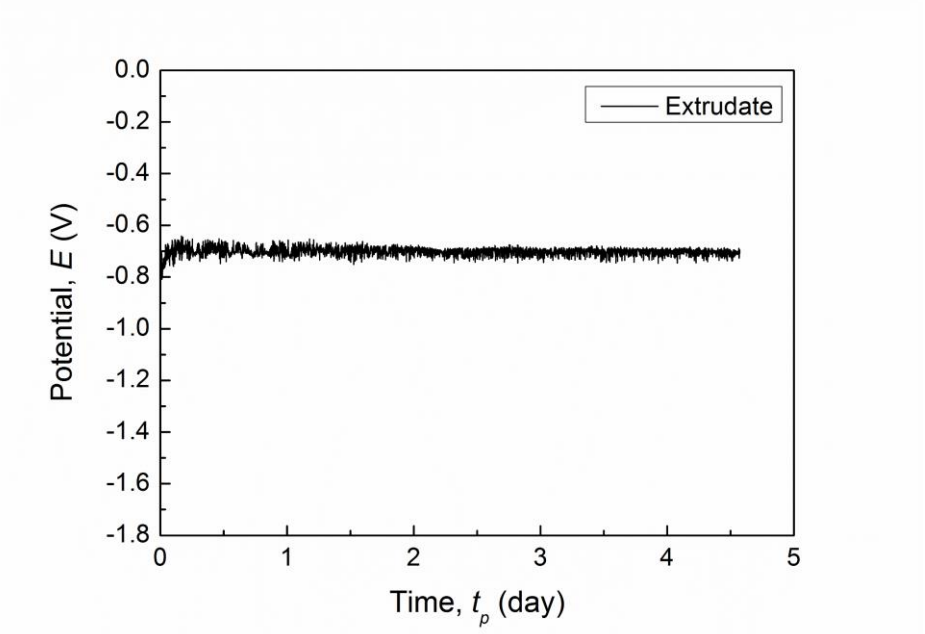

Fig. 2.13 Electrical potential change with respect to immersion time in 3.0 mass% NaCl aqueous solution at room temperature.

2.5 Microstructure

The cross section of the extrudate was mechanically polished and the microstructure of the Mg alloy substrate was observed. The grain size was measured with the area equivalent diameter and quadrature methods.

Figures 2.14 and 2.15 depict the microstructures of the Mg alloy before and after the extrusion, respectively. The extrudate in the figure is the one produced with a die having a die angle of 110 ^{o}. The grain size just before the extrusion was approximately 20 μm, and as is evident from those figures, the grain size decreases to approximately 2.5 μm after the extrusion. This grain refinement is owing to the severe plastic deformation through the hot extrusion and it was realized in all extrusion with any die angles used in the present study.

It is well known that the formability and mechanical properties of Mg alloys are extremely improved by grain refinement [2.3, 2.4]. Therefore, the present Al-coated Mg alloy can be expected to have not only the good corrosion resistance but also the good deformability. Moreover, considering the practical application, the deformability of the extrudate should be demonstrated. Thus, the mechanical properties of the sheet are investigated in the next section.

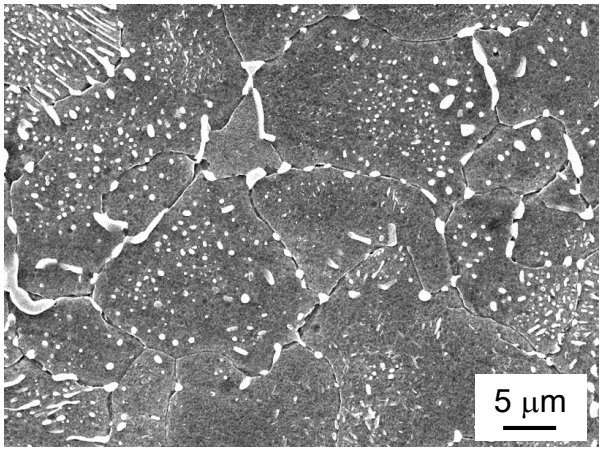

Fig. 2.14 Cross-sectional FE-SEM image of the microstructure of the Mg alloy just before the extrusion.

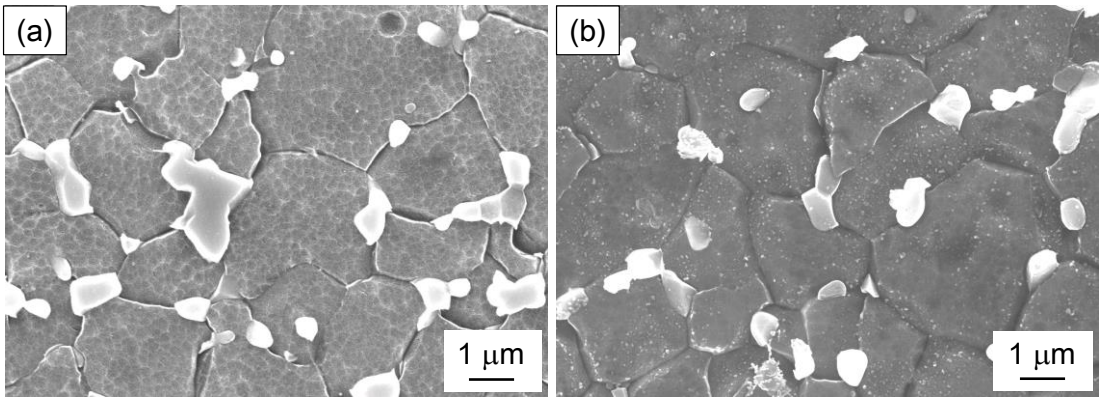

Fig. 2.15 FE-SEM images of the microstructure in the extrudate: (a) cross-sectional and (b) longitudinal sections

2.6 Mechanical properties

2.6.1 Experimental

A three–point bending test and a tensile test were carried out in order to investigate the deformability of the Al-coated Mg alloy extrudate.

The bending test was conducted with a fixed cross-head speed of 3.33 mm/sec. The distance between the supporting points was 75 mm and the final punch displacement was set at 70 mm. The bending specimens were extruded with the die shown in Fig. 2.1 (b) and had 135 mm in length, 5.5 mm in thickness and 20.6 mm in width. The tests were carried out at

room temperature (RT), 373, 473 and 573 K. In order to minimize the friction effect during the test, a graphite sheet was installed between the specimen and the rigid supports. For the tests at elevated temperatures, the specimens were heated up to the target temperatures by a heater equipped near the tensile test machine. The temperature was measured by a contact-type thermocouple and soon after reaching the surface temperature to the predetermined temperature, the specimen was quickly set on the machine and subjected to the test immediately. After the tests, the specimens were cut along the extrusion direction and the cross sections were observed.

For the tensile test, the specimen had its tensile axes parallel to the extrusion direction. The specimens were prepared based on JIS14B with a gauge length of 60 mm. The tensile test was conducted at room temperature and at an initial strain rate of 8.3×10^{-4} s^{-1}. The strain was calculated from the displacement of the crosshead.

2.6.2 Results and discussion

2.6.2.1 Bending test

Figure 2.16 illustrates the load-displacement curves obtained from the bending tests. Although the extrudates were fractured at room temperature, they were deformed to the maximum displacement of 70 mm without fracture at elevated temperatures. The bending load gradually decreases with the displacement after reaching the maximum value in all conditions. The maximum bending load decreases as the testing temperature increases. An instable behavior of the bending load at the last stage of the test conducted at 573 K, which is due to breaking of the carbon sheet placed under the specimen.

Figure 2.17 illustrates the Mg/Al interface near the fracture surface. At the interface far from the fractured part, InterMetallic Compound (IMC) shows many transverse cracks regularly, while at the fracture part, IMC was totally broken and as the results, the Al coating was debonded. It indicates that the coating debonding started from the fracture of IMC followed by the fracture of the Mg alloy substrate and Al coating.

The Mg/Al interface after the bending tests at elevated temperatures were observed and the results are shown in Fig. 2.18. Figures 2.18 (a) and (b), (c) and (d), and (e) and (f) show the specimens tested at 373 K, 473 K and 573 K, respectively. Figures 2.18 (a), (c) and (e) show the interface in the tensile side, while Figs. 2.18 (b), (d) and (f) show the interface in the compression side. The transverse cracks were observed in IMC at 373 K and at 473 K.

However, the cracks were filled with Al, therefore the cracks cannot be the initiation points of the fracture unlike with the results of the test at room temperature.

As can be seen in Figs. 2.18 (e) and (f), no cracks are observed in IMC in the specimen deformed at 573 K. This result indicates that IMC was able to be plastically deformed at 573 K. Furthermore, IMC is elongated linearly in the tensile side of the specimen and pressed and curved in the compression side and no voids or cracks are observed at both interfaces.

Consequently, it can be summarized that the present Al-coated Mg alloy extrudate is capable of subsequent forming at temperatures above 373 K and the good bonding at Mg/Al interface can be maintained at 573 K.

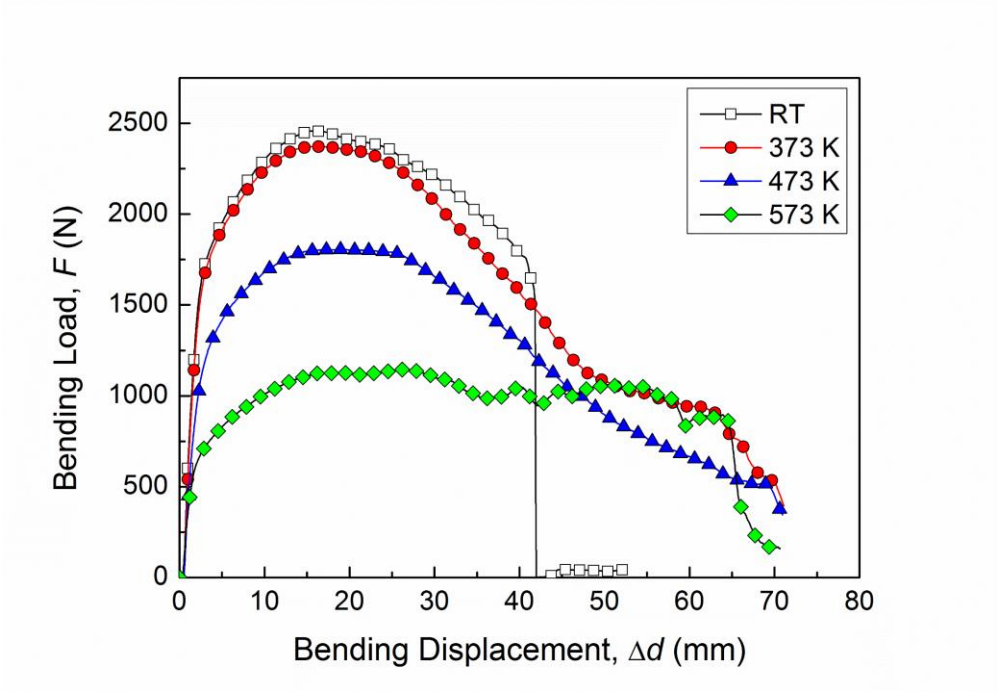

Fig. 2.16 Load-displacement curves obtained from the bending tests in various conditions.

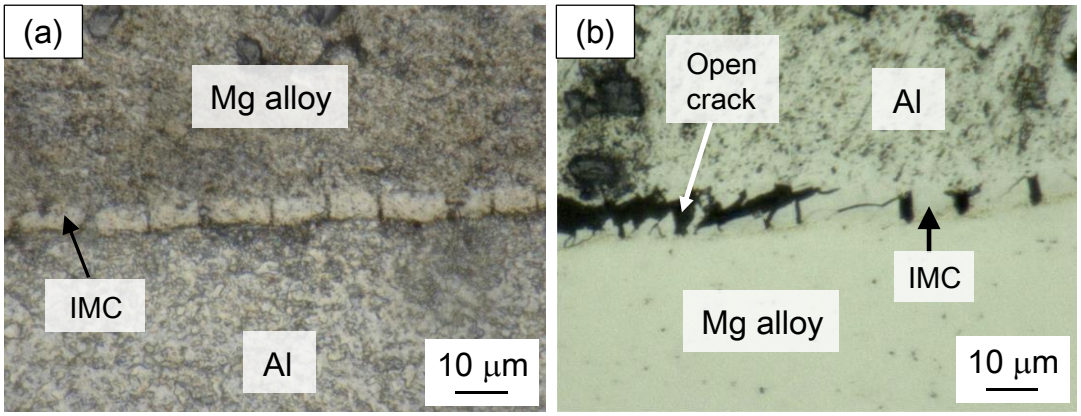

Fig. 2.17 Micrographs of IMC in the fractured specimen; (a) far from the fracture part, (b) near the fractured part.

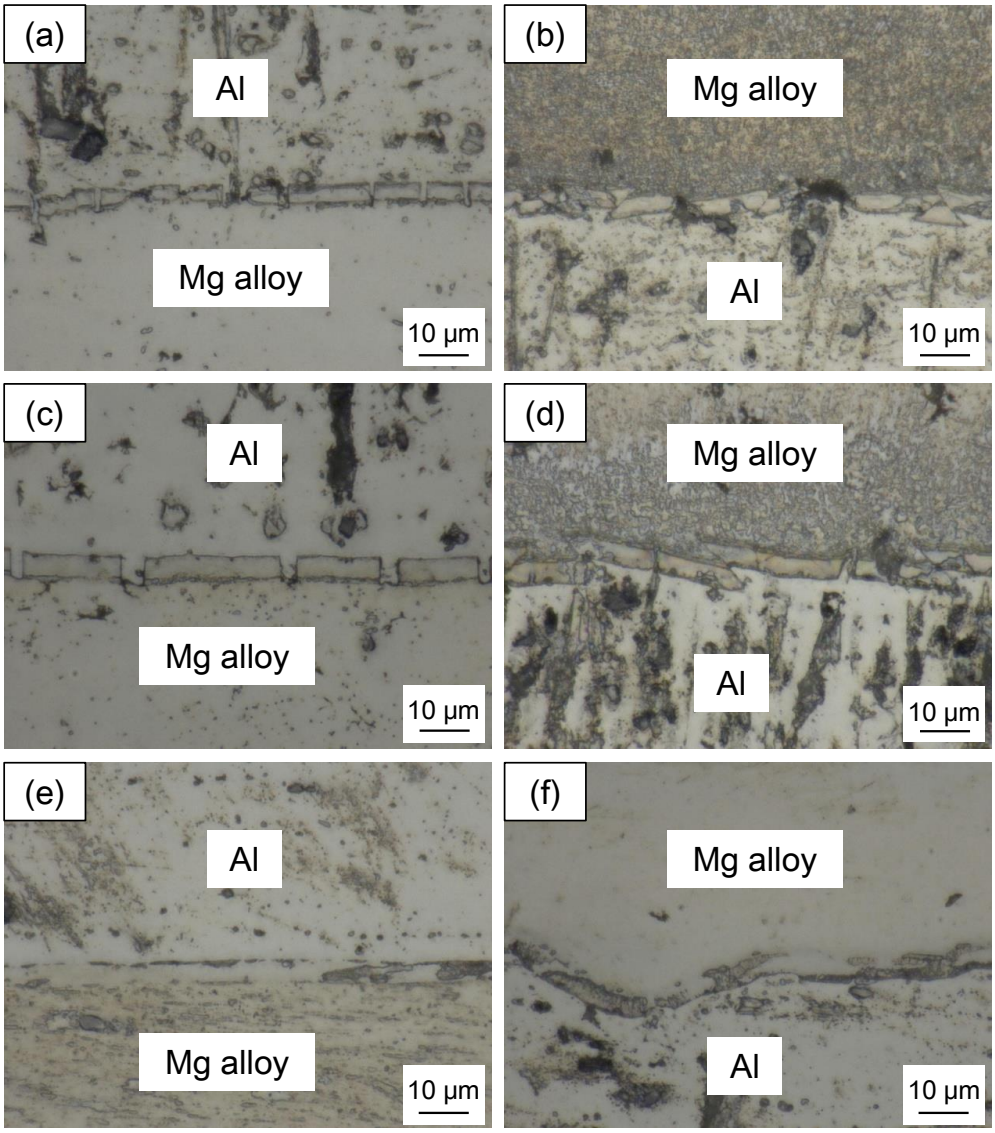

Fig. 2.18 Mg/Al interfaces in the extrudates after bending tests at 373 K for (a) and (b), at 473 K for (c) and (d), at 573 K for (e) and (f). Figures (a), (c) and (e) correspond to the tension side, while Figures (b), (d) and (f) correspond to the compression side.

2.6.2.2 Tensile test

Figure 2.19 shows the stress-strain curve obtained from the tensile test at room temperature. The tensile strength is about 320 MPa and plastic elongation is about 18 %. The typical values of tensile strength and the elongation of the Mg alloy, containing 8 % of Al, are approximately 138 to 325 MPa and 1 to 9 %, respectively [2.5], therefore, it can be said that the present Al-coated Mg alloy possesses as high strength as the ordinary Mg alloys with 8 % of Al and much higher elongation than the ordinary Mg alloys. As mentioned above, it is known that the mechanical properties of Mg alloys are significantly improved by grain refinement [2.3, 2.4]. Therefore, it is reasonable to consider that this improvement of the elongation is attributable to the grain refinement through the hot extrusion.

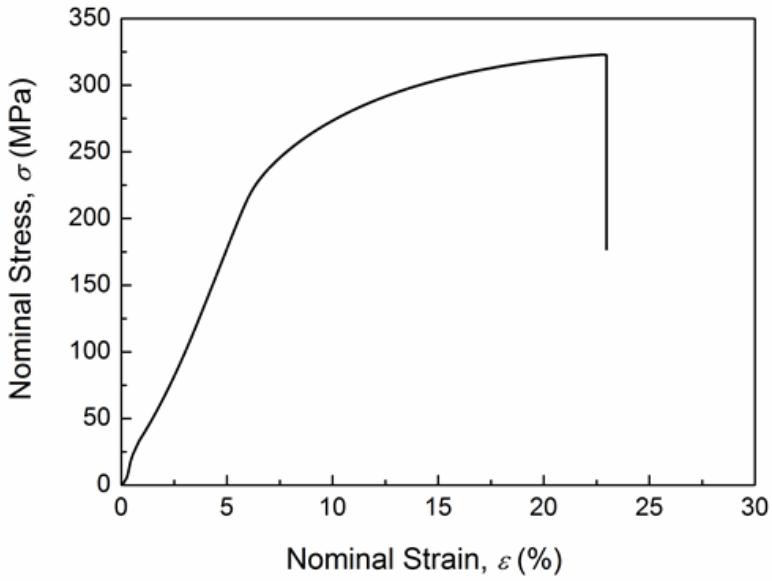

Fig. 2.19 Stress-strain curve of the Al-coated Mg alloy obtained from the tensile test at room temperature.

2.7 Summary

In this chapter, the Al coating technique for Mg alloys, developed in the author's preliminary study, has been explained. The characteristics of the Al-coated Mg alloy extrudate was investigated in detail and the following conclusions were obtained.

(1) Al coating on Mg alloy was realized by using the conventional hot extrusion technique.
(2) Inversely angled die with 110 ^{o} enables continuous uniform thickness coating for a long distance in the length direction. The fine microstructure can be simultaneously obtained through the whole extrudate.
(3) The Al-coated Mg alloy exhibits an excellent corrosion resistance comparable to that of pure Al because of the perfect coating.
(4) Although the Al-coated Mg alloy is fractured in the bending test at room temperature, it exhibits a good deformability at temperatures above 373 K. Furthermore, at 573 K, the intermetallic compound formed at the Al/Mg interface exhibits a good plasticity and the Al-coated Mg alloy showes an excellent plastic deformability.

In this chapter, it has been indicated that the coating thickness uniformity can be controlled by changing the die angle and initial thickness of the coating material plate. However, the coating thickness should be dependent on many process parameters not only those investigated in this chapter. Therefore, from the next chapter, the dependencies of the extrusion process parameters on the coating thickness uniformity in the present Al-coated Mg alloy is investigated.

References

[2.1] T. Tokunaga, K. Matsuura, M. Ohno, Aluminum coating on magnesium-based alloy by hot extrusion and its characteristics. *Mater. Trans.* **53** (2012) 1034-1041.

[2.2] H. Okamoto, Desk Handbook, Phase diagrams for binary alloys, second ed., ASM international, 2010.

[2.3] G.Z. Quan, T. Song, Y.J. Zhou, F.B. Wang, J. Zhou, Relationship between mechanical properties and grain size of AZ80 at 350 ^{o}C under different strain rates. *Trans. Nonferrous Met. Soc. China* **20** (2010) s584-s588.

[2.4] A. Yamashita, Z. Horita, T.G. Langdon, Improving the mechanical properties of magnesium and a magnesium alloy through severe plastic deformation. *Mater. Sci. Eng. A* **300** (2001) 142-147.

[2.5] G.K. Burgess, Circular of the bureau of standards, No. 346, Light metals and alloys – Aluminum, Magnesium. United States government printing office, Washington, 1927.

Chapter 3

Development of flow stress model for the coating process

3.1 Introduction

As was mentioned in earlier chapters, the control of coating thickness uniformity is one of the most important issues for the development of the coating technique for fabrication of the Al-coated Mg alloys. In Chapter 2, it was demonstrated that the coating thickness uniformity depends on both the die angle and the initial thickness of the coating material plate of Al. However, the coating thickness should also depend on many other process parameters such as extrusion temperature, ram speed and the strengths of core and coating materials. Considering the widespread application of the present coating technique based on hot extrusion under the variety of environment, those dependencies should be clarified to control the uniformity of the coating thickness. However, empirical elucidation of such dependencies requires a considerable amount of data, namely time and energy for performing a lot of experiments. Thus, in the present study, in order to clarify the dependencies of the coating thickness on the process parameters, the sensitivity analysis is performed with the help of numerical simulation for the data collection.

The reliability of numerical simulation is strongly dependent on the accuracy of a flow stress model, which describes the rheological properties of the materials. Basically, the flow stress model consists of a number of parameters and coefficients, therefore, it is very hard to determine the model only by experimental tests. Some simple and widely-accepted approaches e.g. the least-square method are often used for the determination, however, there is still a concern about the accuracy of the model. This is because such developed models are directly obtained from the mechanical tests, so the models may be affected by experimental errors and inconsistencies such as effects of friction and inhomogeneities of strain, stress and temperature.

In order for the simulations of the present Al coating process, the flow stress model for AZ80 Mg alloy is required. Some models for AZ80 Mg alloys have been developed and proposed. However, those models were developed in the direct manner as mentioned above [3.1-3.4]. Here, inverse analysis is capable of developing a model such that the real

properties of the focused materials are described independently of above-mentioned disturbances from the mechanical tests [3.5]. Therefore, in the present study, the flow stress model of AZ80 Mg alloy is developed by means of the inverse analysis combined with the optimization process based on the compression test results used as input information.

In this chapter, firstly the basic algorithm and procedure of the inverse analysis are explained. Then, the rheological parameters in the three selected constitutive models are identified by the inverse analysis and optimization process. Finally, this approach is verified by comparing the simulated load-displacement curves using the constitutive models incorporating the identified parameters to the experimental curves obtained from compression tests.

3.2 Direct and inverse problems [3.2]

First of all, in order to understand the basic idea of the inverse analysis, the direct and inverse problems are explained briefly in this section.

Generally, deformation process can be described by a set of equations as below;

$$\mathbf{d} = F(\mathbf{x}, \mathbf{p}) \tag{3.1}$$

where $\mathbf{d} = \{d_1, \ldots, d_r\}$ is a vector of measured output parameter, $\mathbf{x} = \{x_1, \ldots, x_l\}$ is a vector of model parameter and $\mathbf{p} = \{p_1, \ldots p_k\}$ is a vector of process variable. In short, **d** can be simply considered as a set of output, while F(**x**, **p**) as a set of input. In the case of the present study, examples of the foregoing vectors are; temperatures and loads monitored during the compression tests can be **d**, coefficients of the stress-strain curves can be **x** and strain and strain rate can be **p**. When **d** is unknown, the problem to seek **d** is called *direct problem* while when **x** is unknown, the problem is called *inverse problem*. The inverse analysis deals with this inverse problem; the objective of the inverse analysis is to evaluate the optimal values of vector **x** components. The detailed explanation is given in the following sections.

3.3 Inverse algorithm

As already mentioned, the main purpose of this chapter is the identification of rheological parameters in the flow stress model for AZ80 Mg alloy. The identification process consists of the following three stages;

1. Compression tests: Input data collection for the inverse analysis.
2. Numerical simulation of compression test: As a direct problem based on the finite element method (FEM)
3. Process parameter optimization

The above procedures are explained in sequence in the following sections.

3.3.1 Experimental investigation

3.3.1.1 Experimental method

The rheological parameters in the flow stress model are identified based on the mechanical test results. In the present study, the uniaxial compression test was conducted to obtain the base data.

For the compression tests, commercial round bar of AZ80 Mg alloy with a diameter of 42 mm was extruded into a rod having a diameter of 12 mm. The rod was mechanically machined to produce specimens having 8 mm in diameter and 10 mm in height. The compression direction of the test corresponds to the extrusion direction. The detailed chemical composition of the Mg alloy is shown in Table 2.1 in Chapter 2. The specimens were solution-treated at 673 K for 5 hours, and then precipitation-treated again at 623 K for 1 hour to achieve the same microstructure as the one subjected to the extrusion process for the Al coating.

The constant strain rate compression tests were conducted with the Gleeble 3800 simulator at temperatures of 523, 573 and 623 K and at strain rates of 0.01, 0.1 and 1 s^{-1}. The ram speed was continuously and automatically adjusted during the compression tests to obtain the constant strain rates. Two specimens were subjected to each test condition to confirm the repeatability. During the tests, temperature of the specimen was continuously monitored with a thermocouple spot-welded to the side surface of the specimens at the center of the height.

3.3.1.2 Results

Figure 3.1 shows the load-displacement curves obtained from the compression tests. The flow stress decreases as the test temperature increases and as the strain rate decreases. Those curves illustrate the typical compression curves and no peculiar characteristics are observed.

Figure 3.2 shows the temperature changes monitored during the tests. The reasonably stable temperatures were maintained in the tests at lower strain rates (0.01 and 0.1 s^{-1}), while in the tests at a higher strain rate (1 s^{-1}), temperature increases at the beginning of the test and drops at the last stage of the test. Those temperature changes during the tests are due to the heat generation attributable to the plastic deformation, the heat transfer to the environment and the automated control by the Gleeble 3800 simulator. Those temperature changes are introduced as Dirichlet boundary condition to the FE model of the compression tests.

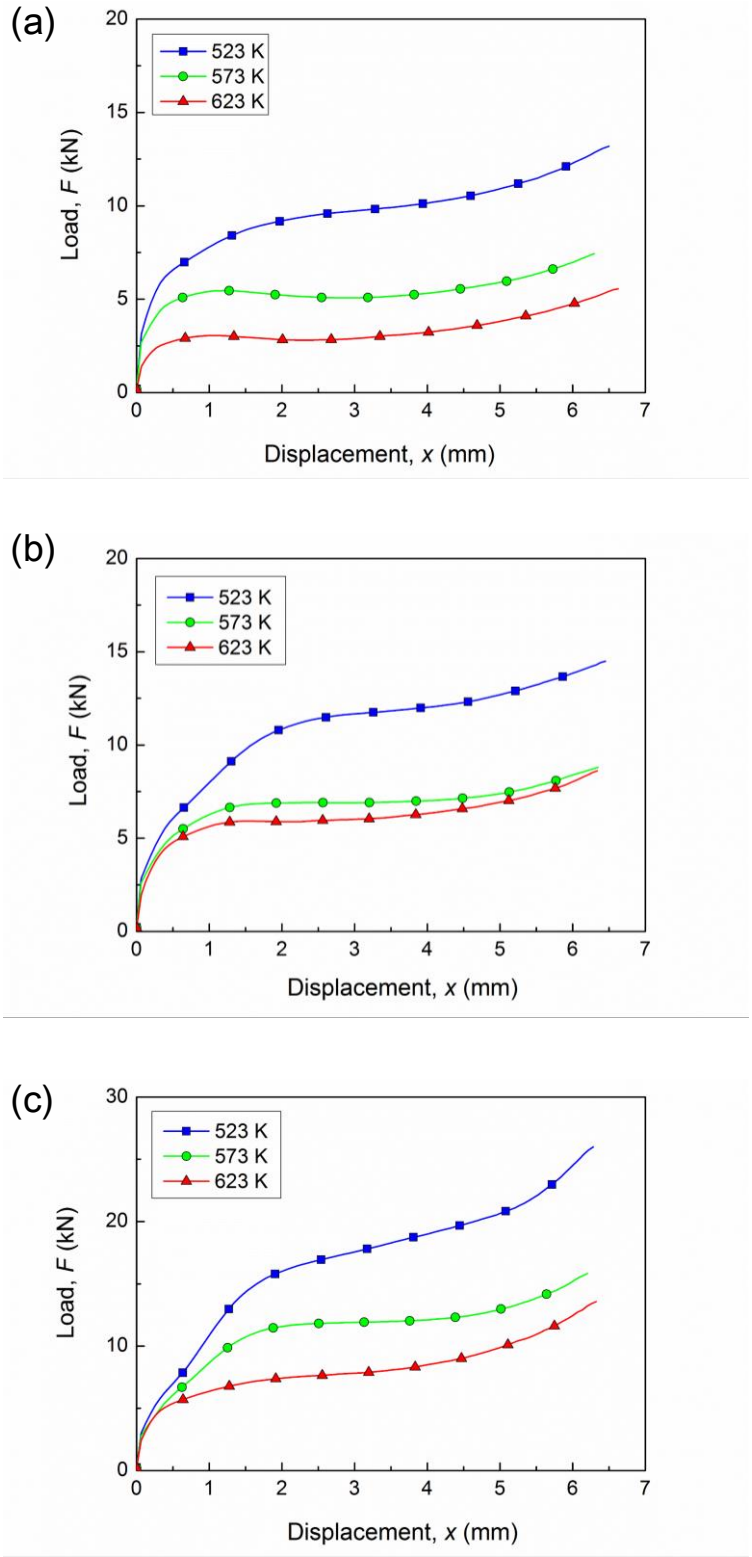

Fig. 3.1 Load-displacement curves obtained from the uniaxial compression tests of AZ80 Mg alloy at various temperatures and at strain rates of (a) 0.01 s^{-1}, (b) 0.1 s^{-1} and (c) 1 s^{-1}.

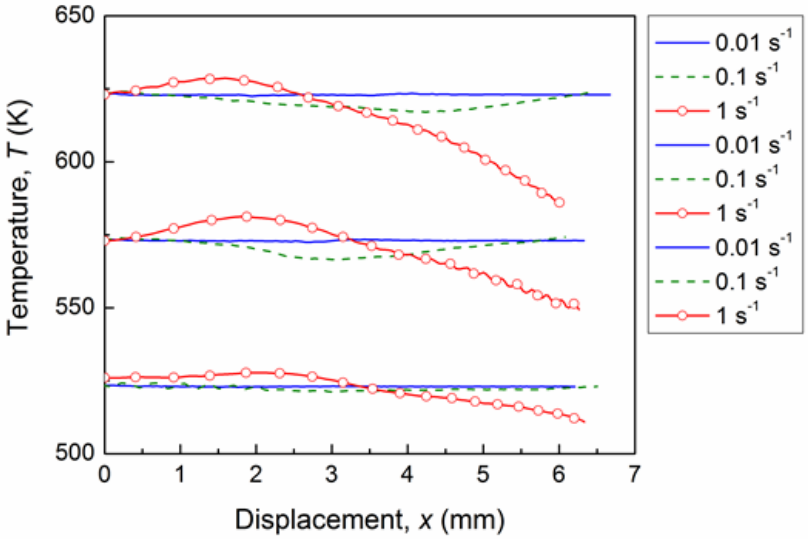

Fig. 3.2 Temperatures monitored during the compression tests at different test temperatures.

3.3.2 Numerical simulation as direct problem [3.5, 3.6, 3.7]

In the present study, the direct problem is defined as a numerical simulation of the uniaxial compression test based on FEM. The behavior of a deformed solid, which occupies a domain Ω (t) at time t, is governed by the momentum balance equation;

$$\nabla\boldsymbol{\sigma} + \rho\mathbf{g} = \rho\ddot{\boldsymbol{u}} \tag{3.2}$$

where $\boldsymbol{\sigma}$ is the stress tensor, ρ is density, **g** is gravity acceleration vector and **u** is vector of displacements. Comparing to the internal forces, the bulk force, inertia and thermal effects are very little and often considered to be negligible [3.8]. Furthermore, for a large plastic deformation problem, the flow formulation approach can be adopted. Thus, the nodal displacements, **u**, and strains, ε, are substituted by nodal velocities, **v**, and strain rates, $\dot{\varepsilon}$, respectively, and the virtual work-rate principle is used. Therefore, Eq. (3.2) can be expressed in the quasi-static formulation as follows [3.8];

$$\int_{\Omega} \nabla\boldsymbol{\sigma}\mathbf{w}\mathrm{d}\Omega = 0 \tag{3.3}$$

where **w** is vector of weight functions.
By applying the Green's theorem, Eq. (3.3) can be rewritten as;

$$\int_{\Omega} \nabla\boldsymbol{\sigma}\mathbf{w}\mathrm{d}\Omega = \int_{\Gamma} \boldsymbol{\sigma}\mathbf{n}\mathbf{w}\mathrm{d}\Gamma - \int_{\Omega} \boldsymbol{\sigma}\nabla\mathbf{w}^{\mathrm{T}}d\Omega \tag{3.4}$$

where **n** is the unit vector normal to the surface. Each weight function in the vector **w** is selected in a such way that it is zero on the boundary, Γ_D, where Dirichlet condition is applied. Thus, considering the suppressible boundary condition *viz.* $\boldsymbol{\sigma}\cdot\mathbf{n} = \mathbf{f}$ on Γ_N and the essential boundary condition *viz.* $\delta\mathbf{v} = 0$ on Γ_D, the first term in the right hand side in Eq. (3.4) is expressed as follows;

$$\int_{\Omega} \nabla\boldsymbol{\sigma}\mathbf{w}d\Omega = \int_{\Gamma_N} \mathbf{f}\mathbf{w}d\Gamma_N - \int_{\Omega} \boldsymbol{\sigma}\nabla\mathbf{w}^{\mathrm{T}}d\Omega \tag{3.5}$$

Substitute Eq. (3.5) into Eq. (3.3);

$$\int_{\Omega} \boldsymbol{\sigma}\nabla\mathbf{w}^{\mathrm{T}}\mathrm{d}\Omega = \int_{\Gamma_N} \mathbf{f}\mathbf{w}d\Gamma_N \tag{3.6}$$

Based on the virtual work-rate principle, the weight functions can be considered as $\mathbf{w} = \mathbf{v}$ and $\nabla\mathbf{w}^{\mathrm{T}} = \dot{\varepsilon}$. Additionally, taking into account the symmetry of the stress tensor and the divergence theorem, the following equation can be obtained;

$$\int_{\Omega} \boldsymbol{\sigma}\cdot\dot{\varepsilon}\mathrm{d}\Omega - \int_{\Gamma_N} \mathbf{f}\cdot\mathbf{v}d\Gamma_N = 0 \tag{3.7}$$

When plastic deformation is considered, the following relation should be introduced into Eq. (3.7);

$$\boldsymbol{\sigma} = \boldsymbol{\sigma}' + \boldsymbol{\sigma}_m \tag{3.8}$$

where $\boldsymbol{\sigma}'$ and $\boldsymbol{\sigma}_m$ are the deviatoric and hydraulic stress tensors. Additionally, the following assumptions are also considered;

$$\boldsymbol{\sigma}_m = \mathrm{tr}(\boldsymbol{\sigma})$$

$$\dot{\boldsymbol{\varepsilon}} = \dot{\varepsilon}_i$$

where σ_i is effective stress, σ_p is flow stress and $\dot{\varepsilon}_i$ is effective strain rate. Consequently, the weak form for the plastic deformation is obtained as below;

$$\int_{\Omega} \boldsymbol{\sigma}'\dot{\boldsymbol{\varepsilon}} d\Omega + \lambda \int_{\Omega} \mathrm{tr}(\boldsymbol{\sigma})\dot{\boldsymbol{\varepsilon}} d\Omega - \int_{\Gamma_N} \mathbf{f}\mathbf{v} d\Gamma_N = 0 \tag{3.9}$$

where $\dot{\varepsilon}_V$ is volumetric strain rate and λ is Lagrange coefficient. λ is a variable and on the solution it gives the average stress, $\sigma_{\boldsymbol{m}}$. The second term in Eq. (3.9) illustrates the incompressibility condition.

Mechanical part is coupled with the thermal model, which is described as the heat transport equation as follows;

$$\nabla k \nabla T + Q = \rho c_p \frac{\partial T}{\partial t} \tag{3.10}$$

where T is temperature, k is conductivity, Q is rate of heat generation due to plastic work, ρ is density, c_p is specific heat and t is time. Additionally, the obtained temperature has to fulfill the following Neumann boundary condition;

$$k \nabla T = \alpha (T - T_a) \tag{3.11}$$

where T_a is ambient temperature or tool temperature and α is heat transfer coefficient.

Mechanical equations and thermal equations are solved separately in each time step and the results are iterated between the two solutions. Specifically, the temperature obtained from the last time step calculation is applied to calculate the flow stress in the current time step, while the stress and strains obtained from the mechanical solution in the previous time step is used for calculation of the Q and consequently for T in the current time step. The calculation of Q is performed with the following equation;

$$Q = a\sigma\dot{\varepsilon} \tag{3.12}$$

where a is constant.

In the present simulation, quadrangle elements were used and bilinear and quadratic shape functions were used for mechanical and temperature calculations, respectively. A set of nonlinear equations is obtained and it is solved by the Newton-Raphson technique. The Newton-Raphson technique is explained in Appendix 1.

Considering the flow theory of plasticity, strain rate, $\dot{\boldsymbol{\varepsilon}}$, is related to stress, $\boldsymbol{\sigma}$, by the Levy-Mises flow rule, which is expressed as follows;

$$\boldsymbol{\sigma} = \frac{2\sigma_p}{3\dot{\varepsilon}_{\text{eff}}}\dot{\boldsymbol{\varepsilon}} \tag{3.13}$$

where σ_p is scalar value of the flow stress and $\dot{\varepsilon}_{\text{eff}}$ is effective strain rate. Specifically, $\boldsymbol{\sigma}$ and $\dot{\boldsymbol{\varepsilon}}$ are the vectors containing components of the stress and strain rate tensors, respectively and the flow stress model, which is developed in this chapter, provides the material constant, σ_p.

3.3.3 Inverse analysis

Inverse analysis is used to correct the flow stress of AZ80 Mg alloy against the undesirable effects of strain and temperature variations in the compression tests. In the present study, efficient two-step inverse algorithm was adopted. Firstly, the rheological parameters in a model are identified separately for each compression test condition (Step 1) and then the obtained model with the optimized parameters is approximated to be able to fully cover the range of temperatures and strain rates for all the test conditions (Step 2). The detailed algorithm of those steps is explained below.

3.3.3.1 Step 1

The input parameters for the Step 1 are the loads and displacements obtained from the compression tests. Firstly, the flow stress, σ_{p}, used in the Levy-Mises flow rule, presented in Eq. (3.13) in FE model, is calculated with the coefficient *a* in the following relationship;

$$\sigma_{\text{p}} = a\sigma_{\text{e}} \tag{3.14}$$

where σ_e is the flow stress calculated directly from the experimental data as;

$$\sigma_{\text{e}} = \frac{F_m}{S} \tag{3.15}$$

where *S* is the loaded contact area, which is calculated based on the assumption such that the barreling is not occurred. However, actually, the undesirable variations of the strain rate and temperature by position exist in the experimental samples due to the deformation inhomogeneity and deformation heating. Those variations can be compensated by

introducing an additional multiplier to Eq. (3.14), and thus, the actual equation to be solved is expressed as;

$$\sigma_{\mathrm{p}} = a\sigma_{\mathrm{e}} \frac{\dot{\varepsilon}^m}{\dot{\varepsilon}_n^m} \exp\left[\frac{Q}{R}\left(\frac{1}{T} - \frac{1}{T_n}\right)\right] \tag{3.16}$$

where R is the gas constant, $\dot{\varepsilon}_n$ and T_{n} are the nominal values of strain rate and temperature for the selected test, while $\dot{\varepsilon}$ and T are the current local values for strain rate and temperature. The strain rate coefficient, m, and the activation energy, Q, are graphically calculated from the measured loads. The flow stress in Eq. (3.16) is applied to the Levy-Mises equation and subsequently, corresponding load and displacement are obtained.

In this step, the coefficient a in Eq. (3.16) is optimized with respect to the following goal function;

$$\Phi = \sqrt{\left(\frac{F_{ij}^m - F_{ij}^c}{F_{ij}^m}\right)^2} \tag{3.17}$$

where F_{ij}^m and F_{ij}^c are measured and calculated loads in every time step j in the i^{th} compression test condition, respectively. The optimization starts from a =1, therefore, σ_{e} is the starting point for the evaluation of σ_{p}.

After the optimization for the coefficient a, the obtained stress-strain curves are subjected to the further optimization process with arbitrary constitutive models, $\sigma_p = \sigma_p(T, \dot{\varepsilon}, \varepsilon, \dots)$, which are capable of covering a whole range of temperatures and strain rates in the compression tests. The goal function of this optimization process is;

$$\Phi = \sqrt{\frac{1}{N_t N_s} \sum_{i=1}^{N_t} \sum_{j=1}^{N_s} \left(\frac{\sigma_{cij} - \sigma_{ij}}{\sigma_{ij}}\right)^2} \tag{3.18}$$

where N_t is the number of performed test, N_{s} is the number of time step, σ_{cij} is calculated stress with the selected model, σ_{ij} is the stress determined in the earlier optimization process with the goal function of Eq. (3.17).

At this stage, an arbitrary constitutive model can be used, however, it is worth noting that the accuracy of the final model strongly depends on the structure of the selected model, that is, careful selection of the model is strongly required. In the present

study, three constitutive models are nominated for this optimization step and those selected models are introduced in the next section.

3.3.3.2 Constitutive models

It is known that Mg alloys are prone to exhibit the dynamic recrystallization (DRX) during hot deformation [3.9]. Therefore, the influence of DRX, that is, softening and saturation, should be considered in the constitutive models.

One of the attempts to describe materials behaviour considering the effect of DRX is Hansel-Spittel equation [3.11, 3.12];

$$\sigma_p = g_1 \varepsilon^{g_2} \dot{\varepsilon}^{g_3} \exp\{-g_4(T-273)\}\exp(-g_5\varepsilon) \tag{3.19}$$

where ε is strain, g_1, g_2, g_3, g_4 and g_5 are coefficients. This model is capable of describing both the hardening and softening effects. However, due to its strong softening effect, calculated flow stress can converge to zero as the strain increases [3.10, 3.11]. This is inappropriate and is the main drawback of this model. In the real DRX process, in fact, the flow stress exhibits a decline followed by a saturation, attributable to the compensation of the softening and strain hardening [3.12]. Therefore, the following flow stress model, which can take into account both the softening and saturation effects, is involved [3.13];

$$\sigma_{\mathrm{p}} = \sqrt{3}\left[W h_1 \varepsilon^{\mathrm{h}_2} \exp\left(\frac{-h_4}{T}\right) + (1-W) h_5 \exp\left(\frac{h_6}{T}\right)\right]\left(\sqrt{3}\dot{\varepsilon}\right)^{h_3} \tag{3.20}$$

$$W = \exp(-h_7\varepsilon)$$

where h_1, h_2, h_3, h_4, h_5, h_6 and h_7 are coefficients. The terms multiplied by *W* and (1-*W*) indicate the hardening and softening effects, respectively.

Lastly, the following equation [3.14, 3.15] is nominated as a candidate in the present study, which allows both the softening and saturation effects, and is selected as the most advanced and flexible model in the present study;

$$\sigma_{\mathrm{p}} = \sigma_0 + \left(\sigma_{\mathrm{ss(e)}} - \sigma_0\right)\left[1 - \exp\left(-\frac{\varepsilon}{\varepsilon_{\mathrm{r}}}\right)\right]^{\frac{1}{2}} - X \tag{3.21}$$

$$\text{where } X = \begin{cases} 0 & \varepsilon \le \varepsilon_{\mathrm{c}} \\ \left(\sigma_{\mathrm{ss(e)}} - \sigma_{\mathrm{ss}}\right)\left[1 - \exp\left(-\left[\frac{\varepsilon-\varepsilon_{\mathrm{c}}}{\varepsilon_{\mathrm{xr}}-\varepsilon_{\mathrm{c}}}\right]^2\right)\right] & \varepsilon > \varepsilon_{\mathrm{c}} \end{cases},$$

$$\sigma_0 = \frac{1}{\alpha_0}\sinh^{-1}\left(\frac{Z}{A_0}\right)^{\frac{1}{n_0}}, \qquad \sigma_{\mathrm{ss}} = \frac{1}{\alpha_{\mathrm{ss}}}\sinh^{-1}\left(\frac{Z}{A_{\mathrm{ss}}}\right)^{\frac{1}{n_{\mathrm{ss}}}},$$

$$\sigma_{\mathrm{ss(e)}} = \frac{1}{\alpha_{\mathrm{sse}}}\sinh^{-1}\left(\frac{Z}{A_{\mathrm{sse}}}\right)^{\frac{1}{n_{\mathrm{sse}}}}$$

$$\varepsilon_{\mathrm{r}} = \frac{1}{3.23}\left[q_1 + q_2\left(\sigma_{\mathrm{ss(e)}}\right)^2\right],\ \varepsilon_{\mathrm{xr}} - \varepsilon_{\mathrm{c}} = \frac{\varepsilon_{\mathrm{xs}} - \varepsilon_{\mathrm{c}}}{1.98},\ \varepsilon_{\mathrm{c}} = C_{\mathrm{c}}\left(\frac{Z}{\sigma^2_{\mathrm{ss(e)}}}\right)^{N_{\mathrm{c}}} \text{ and}$$

$$\varepsilon_{\mathrm{xs}} - \varepsilon_{\mathrm{c}} = C_{\mathrm{x}}\left(\frac{Z}{\sigma^2_{\mathrm{ss(e)}}}\right)^{N_{\mathrm{x}}}.$$

where A_0, A_{ss}, A_{sse}, n_0, n_{ss}, n_{sse}, α_0, α_{ss}, α_{sse}, q_1, q_2, N_c, N_x, C_c and C_x are coefficients. Z indicates the Zener-Hollomon parameter, which is often used to describe the relation between the tendency of DRX and process conditions, and is expressed as follows [3.16];

$$Z = \dot{\varepsilon}\exp\left(\frac{Q_{\mathrm{def}}}{RT}\right) \tag{3.22}$$

where $\dot{\varepsilon}$ is strain rate, Q_{def} is activation energy for deformation. The lower Z value indicates the higher tendency of DRX.

3.3.3.3 Step 2

Coefficients obtained from the last optimization in Step 1 are set at the initial coefficients for Step 2. In this step, the final optimization is performed on the same constitutive models as the last optimization, based on the Nelder-Mead simplex method with the goal function of Eq. (3.18). The Nelder-Mead simplex method is explained in Appendix 2.

By this final optimization process, the optimal coefficients for each model are determined and consequently, the optimal model among those three is selected as the constitutive model for the AZ80 Mg alloy. In order to find the optimal model, all the models are verified as explained below.

3.3.4 Verification

The coefficients of the constitutive models, Eqs. (3.20), (3.21) and (3.22), are summarized in Table 3.1. The converged goal functions obtained from the final optimization process are also presented in the table. The goal function represents the accuracy of the model, namely, the smaller the function is, the better accuracy the model has.

Table 3.1 Obtained coefficients in Eqs. (3.20), (3.21) and (3.22) and the converged goal functions, Φ.

Equation (3.20)	Φ = 0.1257					
g_1	g_2	g_3	g_4	g_5	-	-
3724.4	0.274	0.158	0.00832	1.061	-	-
Equation (3.21)	Φ = 0.1097					
h_1	h_2	h_3	h_4	h_5	h_6	h_7
5.923	0.538	0.1592	2313.4	0.444	2820.7	5.304
Equation (3.22)	Φ = 0.079					
A_0	n_0	α_0	A_{sse}	n_{sse}	α_{sse}	A_{ss}	n_{ss}
0.302×10^{14}	480.6	0.0445	0.167×10^{13}	6.344	0.0064	0.41×10^{14}	7.622
α_{ss}	q_1	q_2	C_c	N_c	C_x	N_x	Q_{def}
0.008	0.369	1×10^{-10}	0.0698	0.0304	0.0008	0.358	145700

In order to verify the present approach and the obtained models, the simulated force-displacement curves by using the selected models incorporating the identified parameters, are compared with the experimental curves obtained from the compression tests. Figures 3.3, 3.4 and 3.5 show the verifications for Eqs. (3.20), (3.21) and (3.22), respectively. Although a perfect accuracy was not achieved for the whole ranges of strain rate and temperature with any of the equations, quite a good agreement was obtained with Eq. (3.22), which showed the lowest goal function, and also, reasonably good agreement was obtained with Eq. (3.21). However, there is a concern about Eq. (3.22) that because of the conditionals in Eq. (3.22), subsequent calculations will be extremely difficult and computation cost will be high. Therefore, simpler Eq. (3.21) was selected as the flow stress model for the subsequent extrusion simulation in the present study.

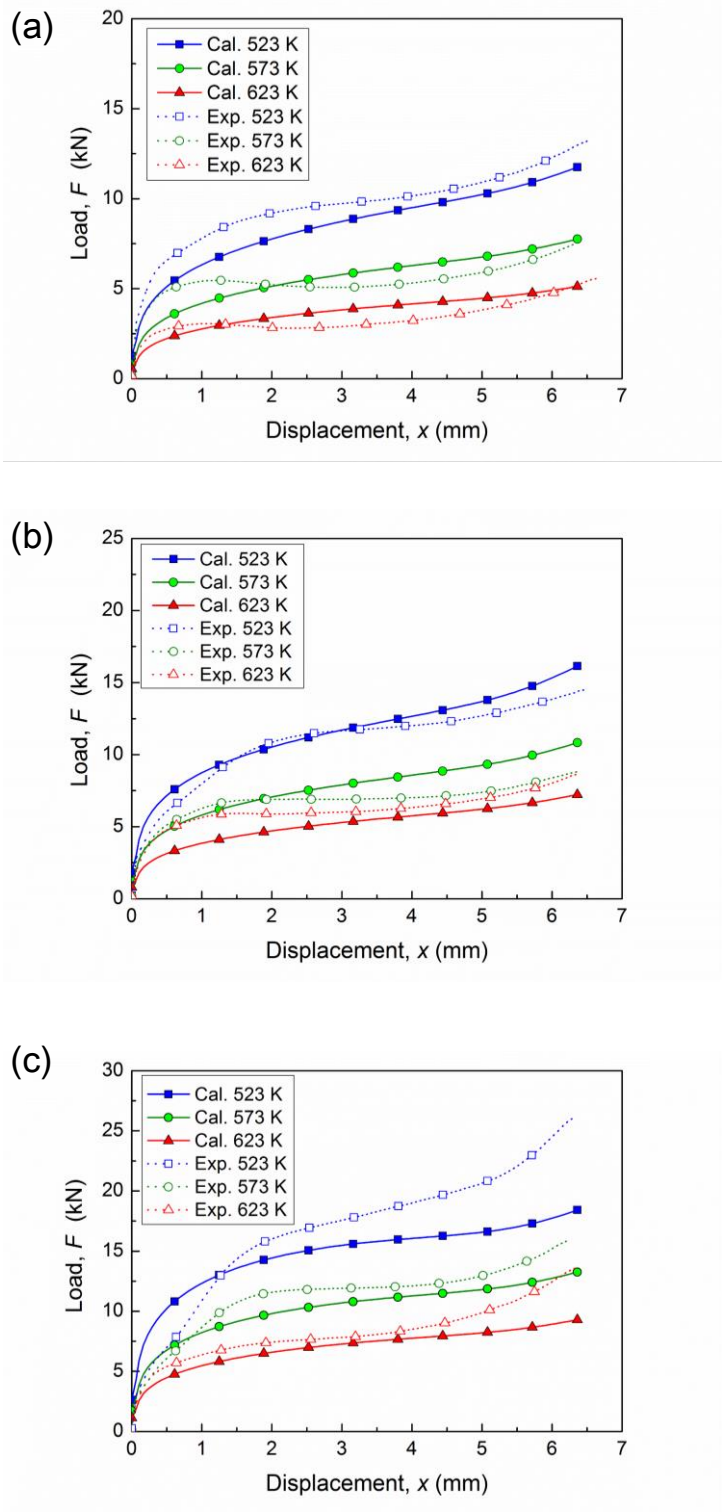

Fig. 3.3 Verifications of measured forces (filled markers) and forces calculated by using FE code with Eq. (3.20) (open markers) at the strain rates of (a) 0.01 s^{-1}, (b) 0.1 s^{-1} and (c) 1 s^{-1}.

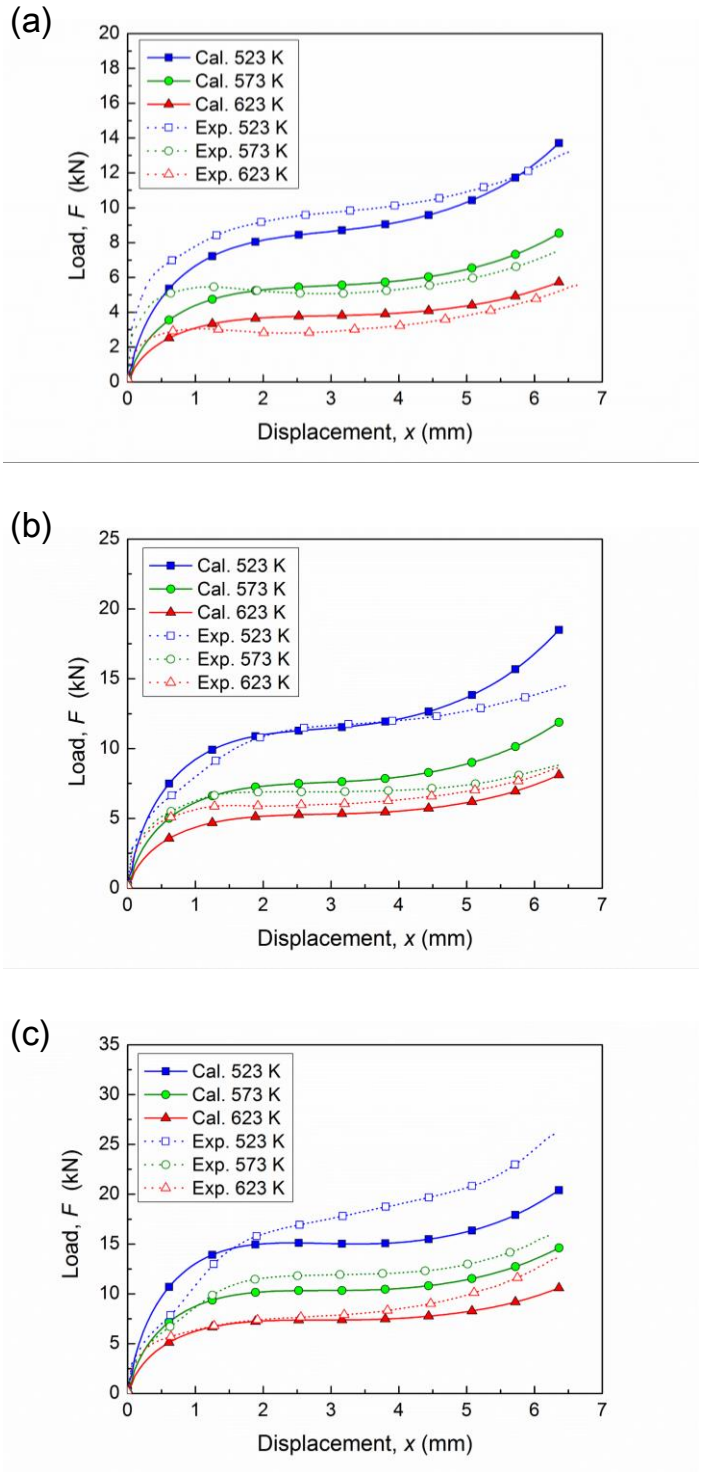

Fig. 3.4 Verifications of measured forces (filled markers) and forces calculated by using FE code with Eq. (3.21) (open markers) at the strain rates of (a) 0.01 s^{-1}, (b) 0.1 s^{-1} and (c) 1 s^{-1}.

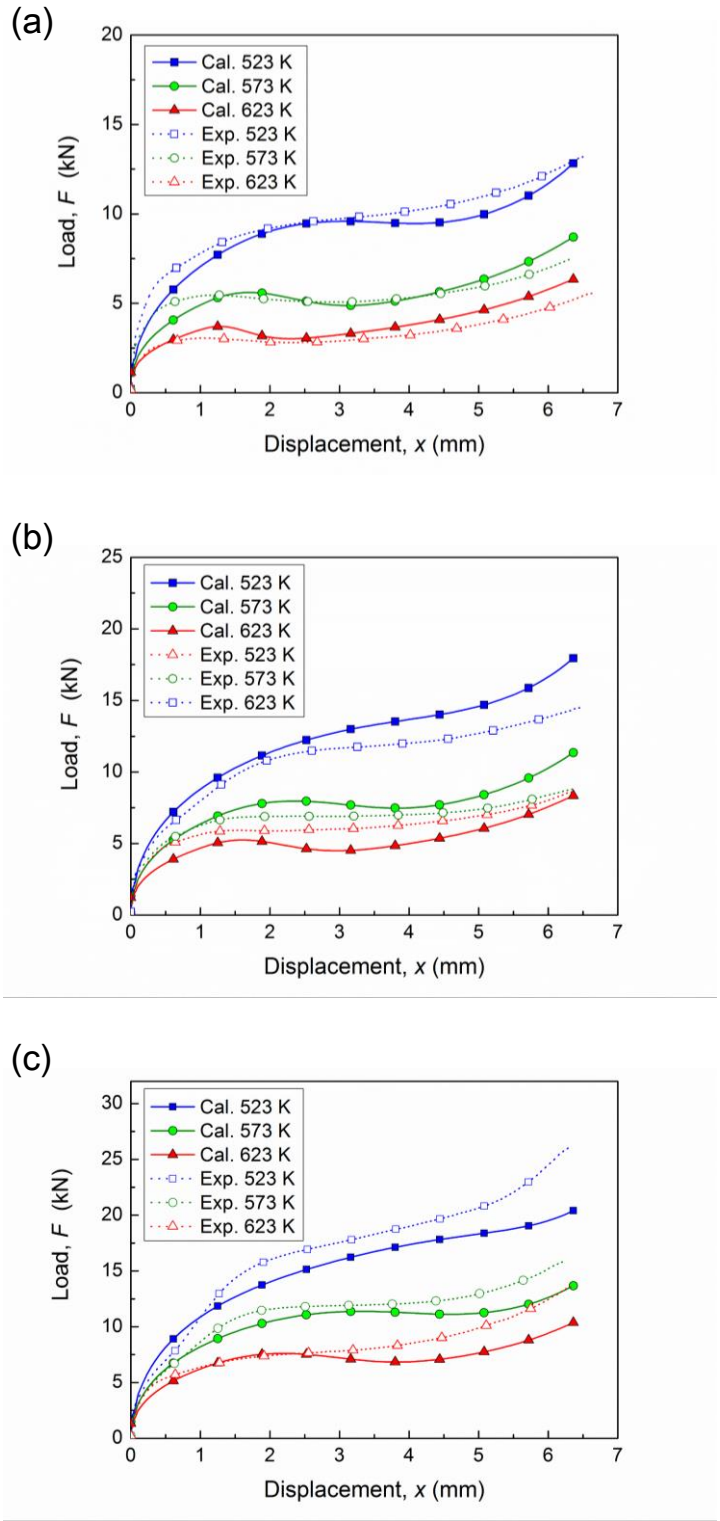

Fig. 3.5 Verifications of measured forces (filled markers) and forces calculated by using FE code with Eq. (3.22) (open markers) at the strain rates of (a) 0.01 s^{-1}, (b) 0.1 s^{-1} and (c) 1 s^{-1}.

3.4 Summary

In this chapter, flow stress model for the AZ80 Mg alloy was developed by the inverse analysis combined with optimization process. Three selected constitutive models were subjected to the optimization process and thereafter, reasonably good agreements between the measured and calculated results were obtained with equations which can take into account not only the softening but also the saturation of the flow stress due to the dynamic recrystallization. By considering the computer-friendliness, the following flow stress model of the AZ80 Mg alloy for the subsequent simulation in the present study was selected;

$$\sigma_{\mathrm{p}} = \sqrt{3}\left[\exp(-5.304\cdot\varepsilon)\cdot 5.923\varepsilon^{0.538}\exp\left(\frac{-2313.4}{T}\right) + \{1-\exp(-5.304\cdot\varepsilon)\}\cdot 0.444\exp\left(\frac{2820.7}{T}\right)\right]\left(\sqrt{3}\dot{\varepsilon}\right)^{0.1592}$$

where ε is strain, T is temperature and $\dot{\varepsilon}$ is strain rate.

In the next chapter, in order to elucidate the dependencies of the coating thickness on the process parameters, the extrusion process for the Al coating is numerically simulated, introducing the currently-developed flow stress model, followed by the sensitivity analysis. The optimal conditions to achieve the uniform thickness coating is described.

References

[3.1] Q.G. Zheng, T. Ying, Z. Jie, Dynamic softening behavior of AZ80 magnesium alloy during upsetting at different temperatures and strain rates. *Proc. Inst. Mech. Eng. Part B-J. Eng. Manuf.* **224** (2010) 1707-1716.

[3.2] H.T. Zhou, Q.B. Li, Z.K. Liu, S.F. Wen, Q.D. Wang, Hot workability characteristics of magnesium alloy AZ80 – A study using processing map. *Mater. Sci. Eng. A* **527** (2010) 2022-2026.

[3.3] G.Z. Qua, Y. Shia, Y.X. Wang, B.S. Kang, T.W. Ku, W.J. Song, Constitutive modeling for the dynamic recrystallization evolution of AZ80 magnesium alloy based on stress-strain data. *Mater. Sci. Eng. A* **528** (2011) 8051-8059.

[3.4] G.Z. Quan, Y. Shi, C.T. Yu, J. Zhou, The improved Arrhenius model with variable parameters of flow behavior characterizing for the as-cast AZ80 magnesium alloy. *Mater. Res.* **16** (2013) 785-791.

[3.5] D. Szeliga, J. Gawad, M. Pietrzyk, Inverse analysis for identification of rheological and friction models in metal forming. *Comput. Meth. Appl. Mech. Eng.* **195** (2006) 6778-6798.

[3.6] D. Szeliga, M. Pietrzyk, Identification of rheological and tribological parameters, metal forming science and practice, in: J.G. Lenard (Ed.), A State-of-art Volume in Honour of Professor J.A. Schey's 80th Birthday, Elsevier, Amsterdam, 2002, pp.227-258.

[3.7] M. Pietrzyk, Finite-element simulation of large plastic deformation. *J. Mater. Process. Technol.* **106** (2000) 223-229.

[3.8] V. Szentmihali, K. Lange, Y. Tronel, J.L. Chenot, R. Ducloux, *J. Mater. Process. Technol.* **43** (1994) 279-291.

[3.9] H.T. Zhou, Q.B. Li, Z.K. Zhao, Z.C. Liu, S.F. Wen, Q.D. Wang, Hot workability characteristics of magnesium alloy AZ80—A study using processing map. *Mater. Sci. Eng. A* **527** (2010) 2022-2026.

[3.10] M.E. Mehtedi, F. Musharavati, S. Spigarelli, Modelling of the flow behaviour of wrought aluminium alloys at elevated temperatures by a new constitutive equation. *Mater. Des.* **54** (2014) 869-873.

[3.11] B. Tang, Z. Yuan, G. Cheng, L. Huang, W. Zheng, H. Xie, Experimental verification of tailor welded joining partners for hot stamping and analytical modeling of TWBs rheological constitutive in austenitic state. *Mater. Sci. Eng. A* **585** (2013) 304-318.

[3.12] C.M. Sellars, Physical metallurgy of hot working, in: *Hot working and forming processes*, (eds), Sellars, C.M., Davies, G.J., The Metals Soc., London, 1979, pp. 3-15.

[3.13] A. Gavrus, E. Massoni, J.L. Chenot, An inverse analysis using a finite element model for identification of rheological parameters. *J. Mater. Process. Technol.* **60** (1996) 447-454.

[3.14] S.B. Davenport, N.J. Silk, C.N. Sparks, C.M. Sellars, Development of constitutive equations for the modelling of hot rolling. *Mater. Sci. Technol.* **16** (1999) 1-8.

[3.15] B. Kowalski, C.M. Sellars, M. Pietrzyk, Development of a computer code for the interpretation of results of hot plane strain compression tests. *ISIJ Int.* **40** (2000) 1230-1236.

[3.16] R. Bhattacharya, B.P. Wynne, Flow softening behavior during dynamic recrystallization in Mg–3Al–1Zn magnesium alloy. *Scr. Mater.* **67** (2012) 277-280.

Chapter 4

Investigation of process parameters on the coating behaviors by computer simulation of hot extrusion

4.1 Introduction

As has been well-described in the earlier chapters, the precise control of coating thickness uniformity is an important issue in the present study. Thus, with a view to the practical applications, the individual effects of the process parameters on the coating thickness uniformity are examined by means of the sensitivity analysis with the help of numerical simulation for the data collection.

In the previous chapter, the flow stress model for AZ80 Mg alloy was developed. Therefore, firstly in the present chapter, the coating process is modelled by using the flow stress model. Subsequently, the sensitivity analysis is performed to find out the process parameter having dominant influence on the coating thickness uniformity. The procedures and algorithms of numerical simulation and sensitivity analysis are explained and consequently, the optimal condition for the uniform thickness coating has been demonstrated.

4.2 Numerical simulation of the coating process

In order for the efficient data collection for the sensitivity analysis, numerical simulation is adopted. In the present study, finite element method (FEM) is performed and the procedures for the FEM calculation based on the present coating process is given below.

4.2.1 Methodology

4.2.1.1 Finite element model

The FE model of the coating process was developed with the commercial Forge 2011 software, which is capable of the thermo-mechanical simulation [4.1]. The applied weak formulation was explained in section 3.2.2 in Chapter 3. In the present simulation, viscoplastic deformation was considered and the elastic deformation was assumed to be

negligible. Thus, the rheological description of the materials in Forge is based on the Norton-Hoff behavior law written in the following tensorial form [4.2];

$$\boldsymbol{s} = 2K\left(\sqrt{3}\dot{\bar{\varepsilon}}\right)^{m-1}\dot{\boldsymbol{\varepsilon}} \tag{4.1}$$

where $\boldsymbol{s}$ is the deviatoric stress tensor, K is material consistency, m is the strain rate sensitivity and $\dot{\boldsymbol{\varepsilon}}$ is the strain rate tensor. $\dot{\bar{\varepsilon}}$ is the effective strain rate, which is described as;

$$\dot{\bar{\varepsilon}} = \left(\frac{2}{3}\sum_{i,j}\dot{\varepsilon}_{ij}^{2}\right)^{\frac{1}{2}} \ . \tag{4.2}$$

4.2.1.2 Finite element discretization

Figure 4.1 illustrates the elements used in Forge for the discretization stage. The element is a four-node tetrahedron with linear interpolation of velocity and pressure. The additional velocity node, which is called the bubble field, is positioned at the center of the element for the stabilization. The bubble field is linear in each of the sub-tetrahedron formed by this central node and three of other nodes in the element. Additionally, in the present simulation, the automatic remeshing algorithm was adopted in order to avoid the element distortion and to keep the accurate simulation.

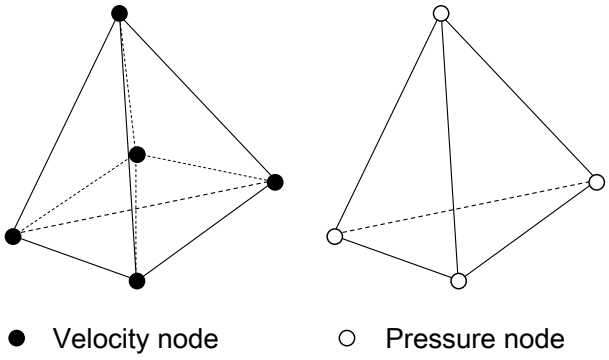

Fig. 4.1 Tetrahedral element in Forge.

4.2.1.3 Extrusion model

The initial geometries for the coating process were created to be the same as the ones used in the experiment explained in Chapter 2. Figure 4.2 shows the initial meshes of the Mg alloy billet, the Al coating material plate and the extrusion tools of the container and die. Considering the symmetry of the geometries, a 2D axisymmetric hot extrusion module was adopted. The meshes in the container and die were set uniformly, while those in the billet and coating material plate were not uniform, being finer in the vicinity of the die aperture, where severe deformation occurs. The bearing of this die is slightly tilted and the corner radius of the die aperture is set at 0.5 mm. The meshes were set finely also at the corner of the die and container wall when the dies are angled.

Table 4.1 illustrates the input parameters used in the simulation. The specific heat, density, thermal conductivity, thermal expansion coefficient and emissivity, were referred to the literature data of pure Mg.

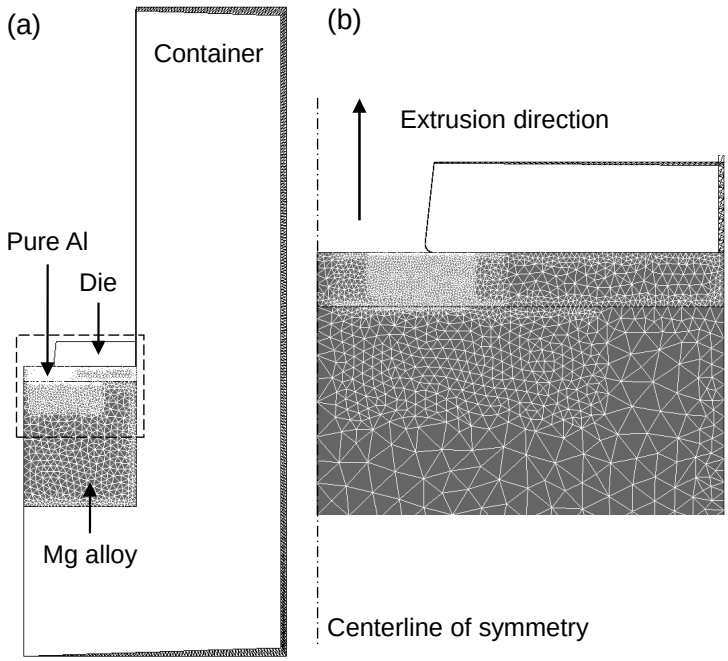

Fig. 4.2 Initial meshes of (a) the Mg alloy billet, Al coating material plate, container and the die having an angle of 90 ◦ and (b) the enlargement of the dotted box in (a).

Table 4.1 Input parameters used for the simulation.

	Billet material	Coating material
Properties	AZ80 Mg alloy	Pure Al (99.6)
Billet/Coating radius (mm)	22.5	22.5
Billet/Coating thickness (mm)	25	3
Initial temperature (^oC)	310	310
Specific heat (J / kg °C)	1159.2	1230
Density (kg / m^3)	1738	2800
Thermal conductivity (W / m ^oC)	122	250
Thermal expansion coefficient (K^{-1})	2.6×10^{-7}	0
Emissivity	0.12	0.05
Tooling temperature (^oC)	310	
Ambient temperature (^oC)	25	
Ram speed (mm/sec)	0.033	
Reduction ratio	14 : 1	
Friction factors at container/billet, container/coating and die/coating interfaces	μ = 0.17, m = 0.34	
Friction factor at billet/coating interface	Bilateral sticking	
Heat transfer coefficient between billet and die/container, billet and coating material and coating material and die/container (W/(m^2·°K))	1.1×10^4	
Tool effusivity between billet and die, billet and container, billet and coating material, coating material and die and coating material and container (W·$s^{1/2}$/K·m^2)	1.176362×10^4	

4.2.1.4 Material consistencies

The flow stress model of the present AZ80 Mg alloy, developed in Chapter 3, is expressed as follows;

$$\sigma_{Mg} = \sqrt{3}\left[\exp(-5.304\cdot\varepsilon)\cdot 5.923\varepsilon^{0.538}\exp\left(\frac{-2313.4}{T}\right) + \{1-\exp(-5.304\cdot\varepsilon)\}\cdot 0.444\exp\left(\frac{2820.7}{T}\right)\right](\sqrt{3}\dot{\varepsilon})^{0.1592} \quad (4.8)$$

where ε is strain, T is temperature and $\dot{\varepsilon}$ is strain rate. This model was assigned to Eq. (4.1) for describing the evolution of the material consistency, K, with respect to the temperature and the strain, and the evolution of m with respect to the temperature. This consistency was given as a tabular form of flow stress as a function of strain, strain rate and temperature.

The flow stress model of the pure Al, as the coating material, was taken from the Forge database as a industrial pure Al (99.6%: Al-0.125Si-0.175Fe-0.025Zn-0.025Cu-0.015Mn-0.015Mg-0.015Ti), which is expressed with Hansel-Spittel law [4.3] as follows;

$$\sigma_{Al} = 268.88875\exp(-0.00539T)\varepsilon^{0.17012}\dot{\varepsilon}^{0.15041}\exp\left(\frac{-0.00018}{\varepsilon}\right). \quad (4.9)$$

The applicable temperature range of this model is 523-823 K, which fully covers the extrusion temperature in the present study.

4.2.1.5 Contact conditions

In this study, friction at all interfaces was controlled by a Coulomb limited Tresca law which is expressed by the following relations;

$$\tau = \mu\sigma_n\frac{\Delta\boldsymbol{v}}{\Delta v} \text{ if } \mu\sigma_n < \bar{m}\frac{\sigma_0}{\sqrt{3}} \quad (4.10)$$

and

$$\tau = \bar{m}\frac{\sigma_0}{\sqrt{3}}\frac{\Delta\boldsymbol{v}}{\Delta v} \quad \text{if} \quad \mu\sigma_n > \bar{m}\frac{\sigma_0}{\sqrt{3}} \quad (4.11)$$

where τ is the shear stress, μ is the Coulomb's friction coefficient, σ_n is the normal stress vector, $\bar{m}$ is the shear friction coefficient and $\Delta\boldsymbol{v}$ and Δv are differences in velocities between two solids in vector and scalar representation, respectively. As explained in Chapter 2, in the experimental extrusion process, boron nitride (BN) powder was sprayed on the container wall and die surfaces for lubrication. The friction parameter of the BN powder, μ, is reported as 0.17 [4.4] and it is empirically known that the friction coefficient, μ, is approximately half of the coefficient $\bar{m}$ [4.5]. Therefore, the friction coefficients μ and $\bar{m}$ were set at 0.17 and 0.34, respectively, at the interfaces of container/billet, container/coating material and die/coating material in the present simulation. Since the billet and coating

materials are bonded together after flowing out through the die aperture, the interface between the billet and coating material was assumed to be bonded from the beginning, thus the nodes at the interface stick together whole through the simulation.

The ambient temperature was set at 298 K and the initial temperatures of the container, die, billet and coating material were set at 583 K. The die and container were assumed to be perfectly rigid, and for simplicity, the friction and thermal coefficients at all interfaces were assumed to be constant through the whole extrusion process.

4.2.2 Model verification

In order to verify the extrusion model, the simulated coating thickness change in the longitudinal direction of the extrudate was compared with the experimental one.

4.2.2.1 Methodology

The methodology of coating thickness measurement in the experiment was explained in Chapter 2. For the evaluation of the simulated coating thickness, an automated thickness measurement option in Forge was adopted. In the option, each node at the interface side and the surface side was taken and the distance between the closest nodes were taken as the thickness. The thickness was smoothed by using the moving-average method every 20 points and then compared with the experimental results for the various die angles.

4.2.2.2 Results

Figure 4.3 illustrates the comparison between the experimental and simulated coating thicknesses with respect to the distance from tip of extrudates for various die angles. Although the errors between the experimental and simulated results gradually increase as the extrusion proceeds, the current extrusion model successfully reproduces the experimental results in the early stage of the extrusion, in general. Furthermore, in the sensitivity analysis, the focused coating thickness should be only the one produced in the steady state, therefore, the quite a large error in the last part of the extrusion process can be negligible as a very unusual part and it can be said that this model can be applied to the sensitivity analysis.

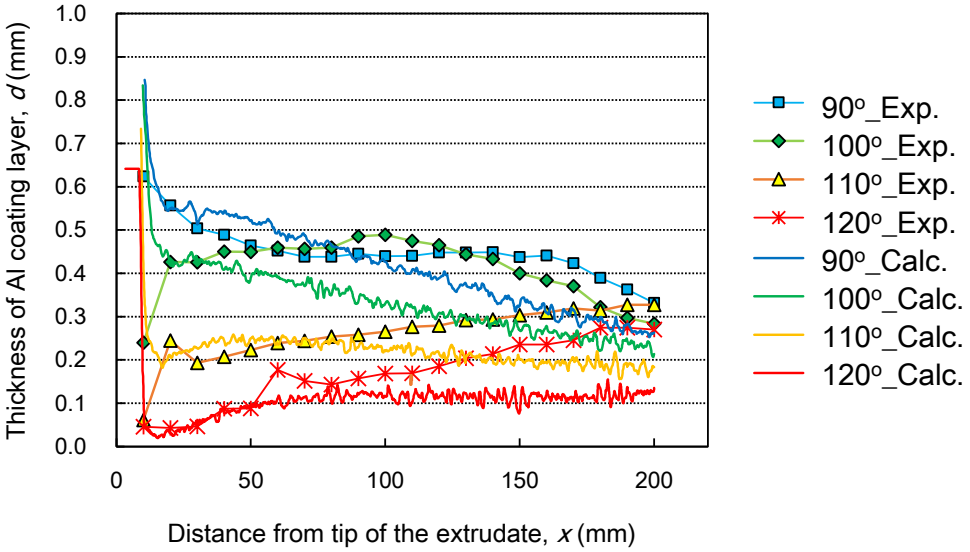

Fig. 4.3 Comparison between the experimental and simulated results for the changes in coating thickness with respect to the distance from the tip of extrudates with various die angles.

4.3 Effective strain distribution

As mentioned above, in the sensitivity analysis, the coating thickness produced only in the steady state should be focused. Thus, in order to determine this focused range *viz.* the steady state range, the effective strain distribution is investigated here. Figure 4.4 illustrates the effective strain distributions after 100 and 250 mm of extrusion. There are slightly inhomogeneous strain distributions in circumferential direction at the tip of extrudates, in Figs. 4.4 (a) to (d), while at the last part of the extrudates in Figs. 4.4 (e) to (h). Therefore, the region extruded between from 50 to 90 mm was selected as the steady state and this range was subjected to the sensitivity analysis in the present study.

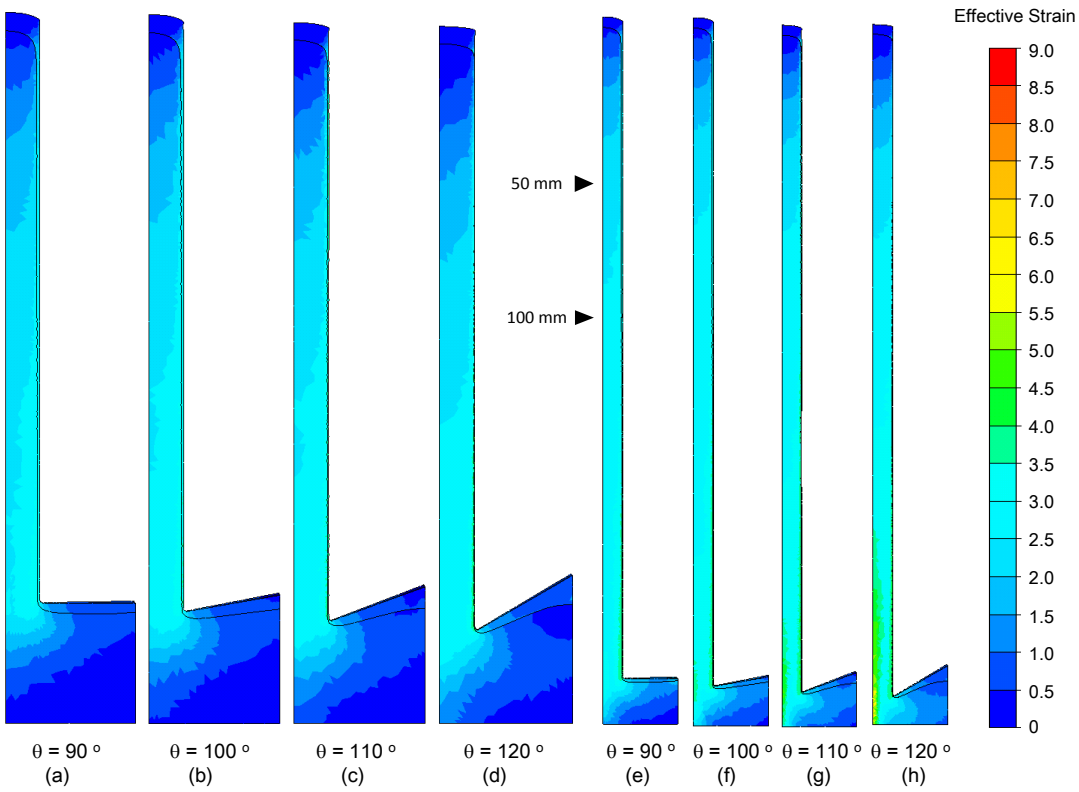

Fig. 4.4 Effective strain distributions. Figs. (a) to (d) show the effective strain distributions after 100 mm of extrusion, while Figs. (e) to (h) show the effective strain distributions after 250 mm of extrusion.

4.4 Sensitivity analysis

The sensitivity analysis can be used to assess the relative importance of input parameter values to the observed output [4.6]. In other words, the sensitivity analysis can indicate the input parameter which has a strong influence on the output.

In the present study, the sensitivity analysis has been performed to investigate which extrusion process parameter contributes most significantly to the uniformity of coating thickness. Additionally, the average coating thickness is also the important information for the products. Therefore, the sensitivity of the average coating thickness with respect to the selected parameters has also been investigated in the present study.

4.4.1 Methodology

For the sensitivity analysis, a full two-level factorial design was adopted owing to the low computational costs [4.7]. In the present study, the sensitivities with respect to the

following five parameters have been evaluated; (1) the initial thickness of the coating material plate, $l_{initial}$, (2) the extrusion temperature, T, (3) the ram speed, V_{ram}, (4) the die angle, θ and (5) the ratio of simulated flow stress to the experimental one for Al, a, being defined as;

$$a = \frac{\sigma_{\mathrm{FD}}}{\sigma_{\mathrm{Al}}} \tag{4.13}$$

where σ_{FD} is the flow stress used in the sensitivity analysis and σ_{Al} is the flow stress of Al. The parameter levels were empirically chosen and are summarized in Table 4.2. In the two-level factorial design, only the two levels, upper and lower levels, are necessary as the input, therefore, 32 simulations with the possible combinations of those parameters were performed, by following the methodology described in the previous sections.

The obtained coating thickness was linearly approximated by the least-square method and the coating thickness was output every 5 mm in the longitudinal direction of the extrudate. The degree of non-uniformity, y, which is assigned to the sensitivity analysis, is defined as follows;

$$y = \frac{\sum_{i=1}^{n}(d_{\mathrm{i}} - d_{\mathrm{ave}})^2}{d_{\mathrm{ave}}^2} \tag{4.12}$$

where d_{i} is the coating thickness at the i^{th} position numerated in the measured range, n is the number of the measurement points and d_{ave} is the average coating thickness.

In the two-level factorial design, the average response from high-level runs is compared with the average response from the low-level runs and the influences of the process parameters, E, are determined as follows;

$$E = \frac{\sum y^{+}}{m^{+}} - \frac{\sum y^{-}}{m^{-}} \tag{4.14}$$

where y is the model output, "+" and "–" indicate the upper and lower limits of the parameter range, respectively and m is the number of simulations at each level.

Furthermore, in order to investigate the influence of each extrusion parameter on the average coating thickness, the sensitivity analysis for the average coating thickness was also performed. The average coating thickness was used as an output, y, and E was calculated by using Eq. (4.14) in the same way as above.

Table 4.2 Factors and levels used in the factorial design.

	Parameters	Low-level	High-level
($l_{initial}$)	Initial thickness of the Al coating material plate (mm)	2	5
(T)	Extrusion temperature (K)	523	623
(V_{ram})	Ram speed (mm/sec)	0.033	1
(θ)	Die angle (deg)	90	110
(a)	Ratio of simulated flow stress to the experimental one for Al	0.9	1.2

4.4.2 Results and discussion

Table 4.3 summarizes all the results with respect to the uniformity of the coating thickness and the average coating thickness. The coating thickness uniformity and the average coating thickness are ranked and are presented in ascending order of the uniformity and thickness. Namely, the first place for the uniformity is the results with the highest uniformity, and the first place for the average coating thickness is the result with the thinnest average coating thickness. From the table, it is clear that the optimal condition with respect to the uniform thickness coating in the present parameter range was obtained in Simulation #25 *viz.* the condition of which is given by the die angle of 110 ^{o}, the initial thickness of the coating material plate of 2 mm, the extrusion temperature of 623 K, the ram speed of 1 mm/s and the ratio of the flow stress of 0.9.

The detailed discussion with respect to the influences of each extrusion parameter on the coating thickness uniformity and average coating thickness is well-described in the following sections.

Table 4.3 Summary of the sensitivity analysis.

Simulation number	Initial thickness of the coating material plate, $l_{initial}$ (mm)	Extrusion temperature, T (K)	Extrusion velocity, V_{ram} (mm/sec)	Die angle, θ (deg)	Flow stress of the coating material, a	Coating thickness uniformity	Uniformity (Rank)	Average coating thickness (μm)	Average thickness (Rank)
1	2	523	0.033	90	0.9	0.01997	18	325.85	15
2	5	523	0.033	90	0.9	0.08922	31	959.45	31
3	2	623	0.033	90	0.9	0.02073	20	307.18	11
4	2	523	1	90	0.9	0.04331	26	339.38	16
5	2	523	0.033	90	1.2	0.01946	17	308.91	12
6	5	623	0.033	90	0.9	0.05905	28	885.14	27
7	5	523	1	90	0.9	0.11257	32	990.37	32
8	5	523	0.033	90	1.2	0.05608	27	895.60	28
9	2	623	1	90	0.9	0.02287	22	311.29	13
10	2	623	0.033	90	1.2	0.01862	16	286.48	9
11	2	523	1	90	1.2	0.03046	23	322.35	14
12	2	623	1	90	1.2	0.01550	14	297.33	10
13	5	523	1	90	1.2	0.07832	30	931.24	30
14	5	623	0.033	90	1.2	0.03565	24	809.14	25
15	5	623	1	90	0.9	0.06825	29	898.25	29
16	5	623	1	90	1.2	0.04196	25	828.42	26
17	2	523	0.033	110	0.9	0.00219	3	155.02	6
18	5	523	0.033	110	0.9	0.00810	7	556.24	23
19	2	623	0.033	110	0.9	0.00347	4	150.96	4
20	2	523	1	110	0.9	0.02051	19	169.76	8
21	2	523	0.033	110	1.2	0.00054	2	153.44	5
22	5	623	0.033	110	0.9	0.00991	9	489.73	19
23	5	523	1	110	0.9	0.01359	13	607.53	24
24	5	523	0.033	110	1.2	0.00783	6	498.94	20
25	2	623	1	110	0.9	0.00003	1	149.11	3
26	2	623	0.033	110	1.2	0.00629	5	142.08	1
27	2	523	1	110	1.2	0.00891	8	169.41	7
28	2	623	1	110	1.2	0.01040	10	147.87	2
29	5	523	1	110	1.2	0.02247	21	542.89	22
30	5	623	0.033	110	1.2	0.01089	11	438.35	17
31	5	623	1	110	0.9	0.01343	12	504.24	21
32	5	623	1	110	1.2	0.01649	15	450.88	18

4.4.2.1 Coating thickness uniformity

The degree of non-uniformities obtained in the sensitivity analysis are illustrated in Fig. 4.5. The shaded and non-shaded bars illustrate the results obtained with the initial thickness of the Al coating material plate of 2 and 5 mm, respectively. The smaller value of the degree of non-uniformity, *y*, means the higher uniformity. Therefore, it is clear that when the initial thickness of the Al coating material plate is thinner, the higher uniformity was obtained. Furthermore, considering that the simulations numerated from 1 to 16 are the results with 90 ^{o} of die angle, while from 17 to 32 are with 110 ^{o}, it is worth noting that the higher uniformity is obtained when the die angle is larger.

Figure 4.6 exhibits the sensitivities of the coating thickness uniformity with respect to the process parameters. The higher absolute value of the *E* indicates that the parameter has the more significant influence on the coating thickness uniformity. It is clear from this figure that the die angle has the most significant influence on the coating thickness uniformity and

the initial thickness of the Al coating material plate also has a great influence. This result well-reflects the results shown in Fig. 4.5. The extrusion temperature, ram speed and flow stress ratio do not have very significant influences compared to the above two parameters.

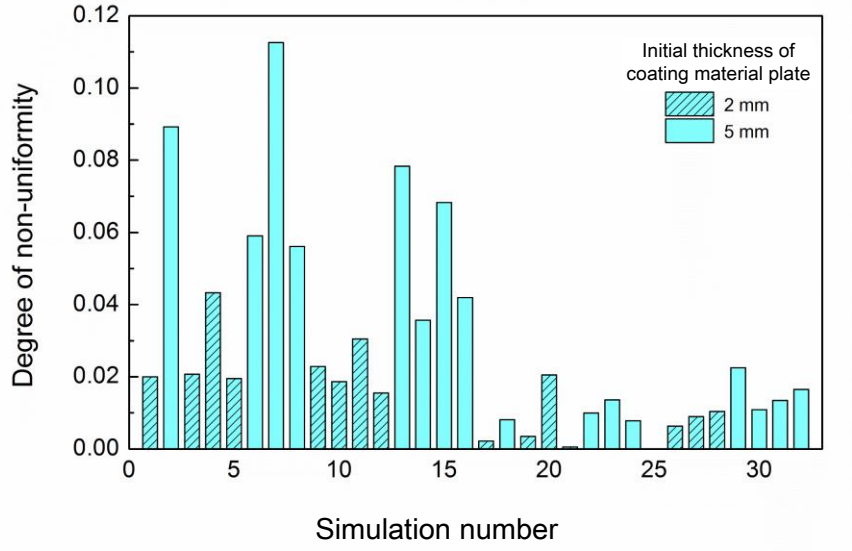

Fig. 4.5 Degree of non-uniformity in the coating thickness in simulations under many different conditions. The shaded and non-shaded bars illustrate the results obtained with the initial thickness of the coating material plate of 2 and 5 mm, respectively. The numbers shown on the horizontal data label express the simulation numbers shown in Table 4.3. The smaller value of the degree of non–uniformity, *y*, means the higher uniformity.

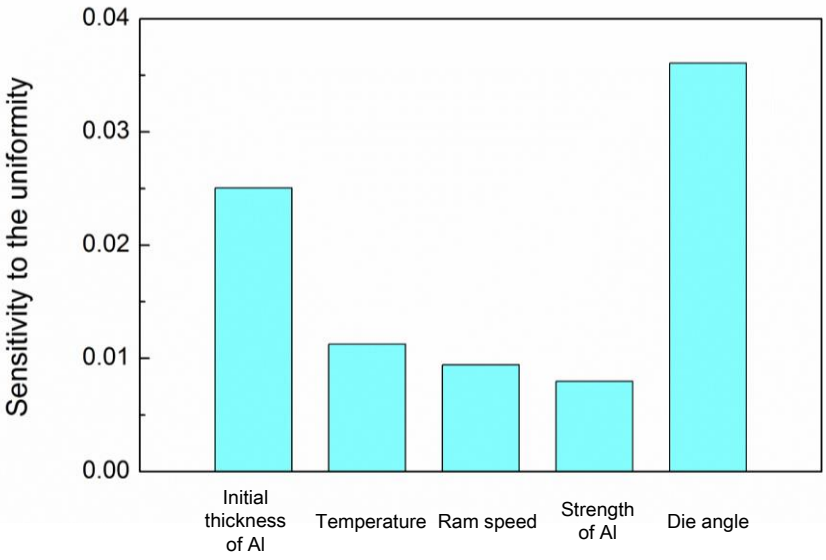

Fig. 4.6 The effects of the parameters on the coating thickness uniformity.

4.4.2.2 Average coating thickness

Figure 4.7 exhibits the average coating thicknesses obtained from all the simulations. The shaded and non-shaded bars correspond to the results obtained with the initial thickness of the Al coating material plate of 2 and 5 mm, respectively. From the figure, naturally, it is clear that the average coating thickness is much thicker when the initial thickness of the coating material plate is thicker. These results agree with the experimental results presented in Chapter 2.

Figure 4.8 exhibits the results of sensitivity analysis with respect to the average coating thickness. The higher absolute value of the sensitivity indicates the parameter has the higher influence on the average coating thickness. From the figure, it can be seen that the average coating thickness is influenced most by the initial thickness of the coating material plate and the die angle also has a great influence. On the other hand, the extrusion temperature, ram speed and flow stress ratio do not have very significant influences. These results show the same tendency as the results of sensitivity analysis for the coating thickness uniformity.

Consequently, it can be concluded that the important parameters, with respect to the coating thickness characteristics for the present Al coating technique, are the initial thickness of the coating material plate and the die angle.

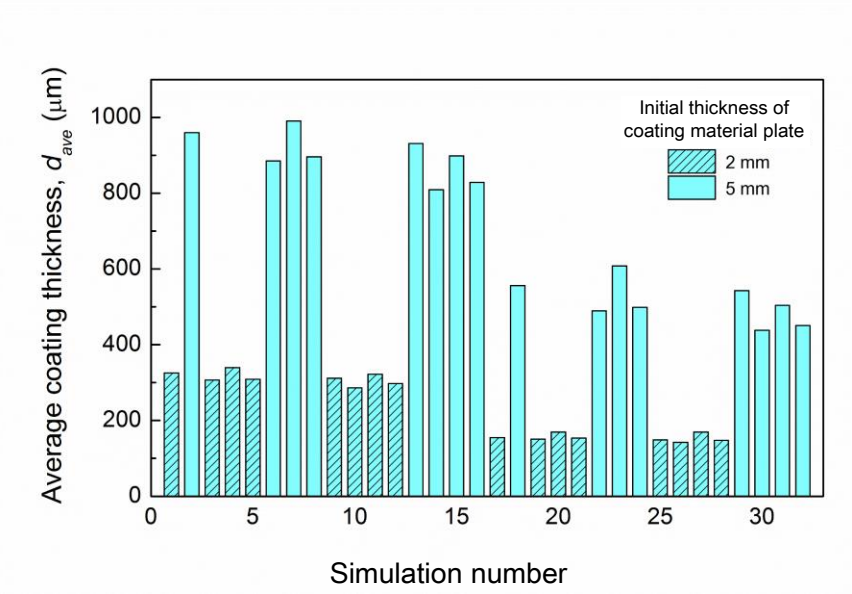

Fig. 4.7 Average coating thickness in simulations under many different conditions. The shaded and non-shaded bars illustrate the results obtained with the initial thickness of the coating material plate of 2 and 5 mm, respectively. The numbers shown on the horizontal data label express the simulation numbers shown in Table 4.3. The smaller value of the degree of non–uniformity, *y*, means the higher uniformity.

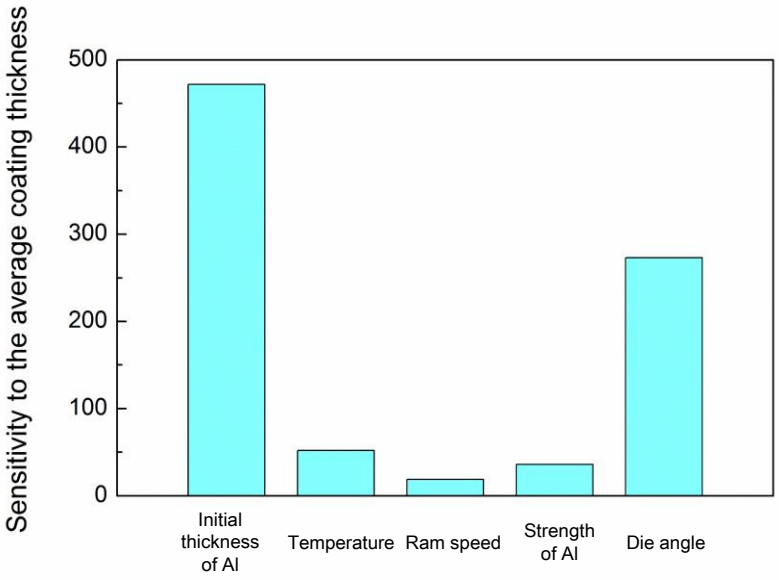

Fig. 4.8 The effects of the parameters on the average coating thickness.

4.4.2.3 Velocity field

The metals flow of the Al plate and the Mg alloy billet inside the container can be considered to have a direct influence on the coating thickness. Thus, in order for the further understanding of the present sensitivity analysis results, the velocity fields in the container were investigated. Figure 4.9 illustrates the velocity in transverse direction after the extrusion of 90 mm. Figures 4.9 (a) and (b) illustrate the results with a ram speed of 0.033 and 1 mm/sec, respectively. The numbers shown under each figure represent the simulation numbers shown in Table 4.3. The pictures are presented in ascending order, thus the results showing the highest uniformity is positioned in the left top, while the results showing the lowest uniformity are positioned in the right bottom corner.

It can be seen that the coating thickness results in non-uniform when metals flow directly to the die aperture, while the uniform coating thickness was obtained when the metal flows around in the container. Specifically, the uniform coating can be obtained when the metal flow near the die surface is suppressed, while on the other hand, the coating thickness is not uniform when the metals near the die surface flow preferentially. From the figures, it is clear that those suppressions of the metal flow are largely attributable to the die angle. Therefore, the sensitivity analysis results, indicating the die angle has significant influence on the coating thickness uniformity, have been explained by the metals flow inside the container.

Furthermore, as shown in earlier sections, when the initial thickness of the Al coating material plate is thinner, the coating thickness results in uniform. This can be explained from the viewpoint of the velocity field as follows. Because when the initial Al coating material plate is thinner, the amount of Al affected by the velocity field is relatively small. Therefore, the amount of the Al, flowing through the die hole, can be stable through the whole process of extrusion and uniform thickness coating can be obtained.

Consequently, it is demonstrated that the flows of the metals near the die surface have significant influence on the coating thickness uniformity, and the die angle and initial thickness of coating material plate involve the flows deeply, which coincides the sensitivity analysis results well.

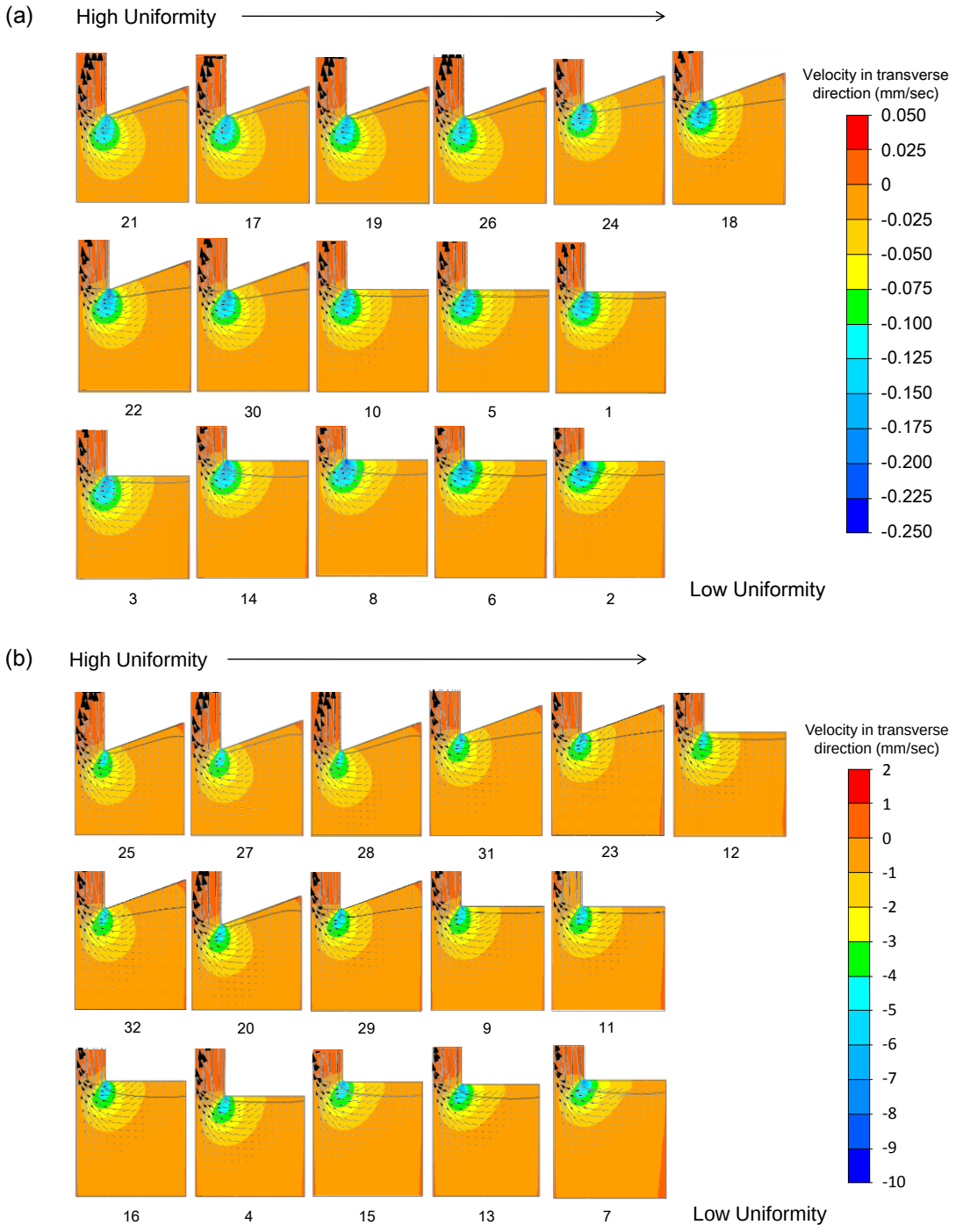

Fig. 4.9 Velocity distributions in transverse direction after 90 mm of extrusion; (a) with a ram speed of 0.033 mm/sec, (b) with a ram speed of 1 mm/sec. The numbers shown under each figure correspond to the simulation numbers shown in Table 4.3.

4.5 Summary

In this chapter, the sensitivities of both coating thickness uniformity and average coating thickness with respect to the process parameters in the present coating technique were evaluated.

The 2D FE model of the extrusion process for the present Al coating technique for Mg alloys was developed and it was confirmed that the model successfully reproduces the experimental results in terms of the coating thickness change. From the sensitivity analysis, it was found that the die angle and the initial thickness of the Al coating material plate have the most significant influence on both the coating thickness uniformity and the average coating thickness. Additionally, from the investigation of the velocity field, it was demonstrated that the flows of the metals near the die surface have significant influence on the coating thickness uniformity and the die angle and initial thickness of coating material plate involve the flows deeply. This indicated relationship explained the results of the sensitivity analysis well.

References

[4.1] G. Banaszek, S. Berski, H. Dyja, A. Kawalek, Theoretical modelling of metallurgical defect closing-up processes during forming a forging. *J. Iron Steel Res. Int.* **20** (2013) 111-116.

[4.2] J.L. Chenot, M. Bellet, The viscoplastic approach for the finite-element modelling of metal forming processes. in: P. Hartley, I. Pillinger, C.E.N. Sturgess (Eds) Numerical Modelling of Material Deformation Processes, Springer-Verlag, London, Berlin, 1992, pp. 179-224.

[4.3] M.El. Mehtedi, F. Musharavati, S. Spigarelli, Modelling of the flow behaviour of wrought aluminium alloys at elevated temperatures by a new constitutive equation. *Mater. Des.* **54** (2014) 869–873.

[4.4] T. Funahashi, T. Koitabashi, R. Uchimura, T. Koshida, A. Yoshida, T. Ogasawara, Development and Application of High-Purity Hexagonal Boron Nitride (h-BN) Powder. *Kawasaki Steel Giho.* **24** (1992) 135–141.

[4.5] Q. Zhang, E. Feldera, S. Bruschib, Evaluation of friction condition in cold forging by using T-shape compression test. *J. Mater. Process. Technol.* **209** (2009) 5720-5729.

[4.6] A. Saltelli, T. Homma, Sensitivity analysis for model output, performance of black box techniques on three international benchmark exercises. *Comput. Stat. Data Anal.* **13** (1992) 73–94.

[4.7] A. Saltelli, K. Chan, E.M. Scott, Sensitivity analysis. Wiley, New York, 2000.

Chapter 5

Fabrication of Al-coated Mg alloy sheet by hot forging

5.1 Introduction

The Al coating technique for Mg alloys was successfully developed by using hot extrusion in the present author's study and the produced bars and plates exhibited excellent corrosion resistance, as explained in Chapter 2. However, in practice, Mg alloys are often used industrially as sheet materials rather than bars and plates for making the best use of their lightness. Therefore, the feasibility of sheet fabrication based on the present technique is important information, which demonstrates the practical applicability of the present technique. In this chapter, therefore, the fabrication of Al-coated Mg alloy sheet is attempted and its characteristics are investigated. Generally sheet formation is performed by the hot rolling process. However, sufficient equipment for the rolling process is not available in the author's laboratory, therefore, hot forging is selected as a replacement sheet forming process of the high speed continuous hot rolling.

5.2 Experimental

Fabrication of Al-coated Mg alloy sheets were attempted by hot forging of the Al-coated Mg alloy plates produced by the present hot extrusion technique. The hot forging equipment is illustrated in Fig. 5.1. A commercial extruded bar of AZ80 Mg alloy, having the same chemical composition as the one dealt in Chapter 2, was used for the substrate material, while an industrially pure Al ingot having 99.99 mass% purity was used for the coating material. The materials were extruded together at 553 K and at a ram speed of 2 mm/min. For this extrusion, a die shown in Fig. 5.2 was used.

The extruded plate, having a width of 20 mm and a thickness of 10 mm, was sectioned perpendicular to the extrusion direction at positions of every 7 mm from the tip of extruded plate, in order to produce small samples for hot forging. Before hot-forging of these small samples, a dummy sample, having a hole with a thermocouple, was set between the hot forging dies every time. The dummy sample was utilized to monitor the heating curve, to determine how long the real sample without the thermocouple should be held there to reach the forging temperature. After determination of the holding time, the real samples were put

between the dies, held for a pre-determined time, and then hot-forged at 523 K. The cross-head speed was 8.4 mm/sec, which is equivalent to an initial strain rate of 0.84 s^{-1}, and the sample thickness was reduced from 10 to 1.5 mm, namely, 85 % in thickness reduction. The die surfaces were lubricated with BN powder before installation.

After the hot forging, the produced sheets were cut and the cross sections were

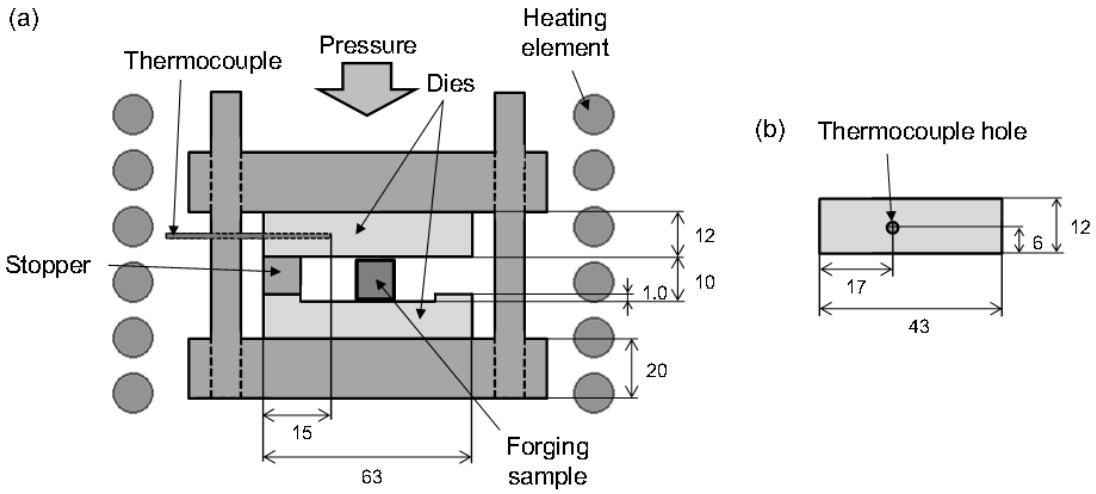

Fig. 5.1 (a) Schematic drawing of the equipment for hot forging (b) dimensions of the upper die and position of the thermocouple hole (all dimensions are in mm).

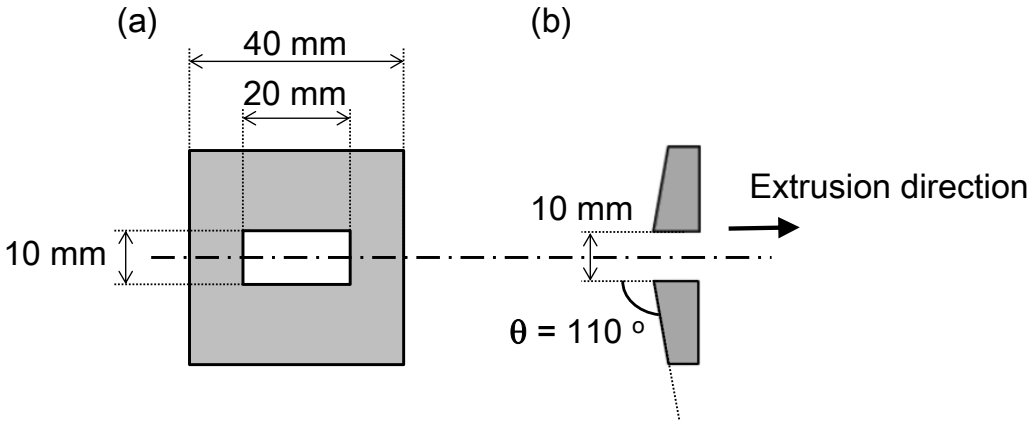

Fig. 5.2 Schematic drawing of the die for sheet fabrication; (a) overhead view of the die and (b) cross section of the die.

macroscopically observed by an optical microscope and the EBSD (electron backscatter diffraction) analysis was performed to observe the microstructures of both the Al coating layer and the Mg alloy substrate.

5.3 Al-coated Mg alloy sheet

5.3.1 Macroscopic observation

Figure 5.3 exhibits the cross-sectional pictures of the Al-coated Mg alloy plate (Fig. 5.3 (a)) and the sheet produced from the plate by hot forging (Fig. 5.3 (b)). Even after the severe plastic deformation of the hot forging, the Al coating layer covers the Mg alloy substrate and no debondings are found. Thus, it can be said that the Al-coated Mg alloy sheet was successfully fabricated by hot forging and it was indicated that the Al-coated Mg alloy extrudate is capable of subsequent forming.

5.3.2 Microstructure observation

The microstructures and crystallographic orientations of the Al layer and the Mg alloy substrate in the sheet are depicted in Figs. 5.4 (a) and (b), respectively. The black and white boundary lines represent high (more than 15 ^{o}) and low (2 ^{o} to 15 ^{o}) angle grain boundaries. The average grain sizes of the Al and Mg alloy are approximately 2.6 μm and 2.0 μm, respectively. Since before the hot forging, the grain sizes of the Al and Mg alloy were 5.2 and 2.5 μm, respectively, it was found that the further grain refinement was achieved by hot forging. The grains are mostly surrounded by the high angle boundaries and the grains are equiaxed in both the Al and Mg alloy even after undergoing the 85 % thickness reduction. Therefore, it is evident that both the Al and Mg alloy were recrystallized owing to the hot forging. Furthermore, Figs. 5.4 (c) and (d) show the {111} and {0001} intensity plots for each part of Al and Mg alloy in the sheet. The RD in these figures corresponds to the forging direction. In the Al part, the intensity plot indicates that the slip on {111} octahedral planes occurred in a major extent, while in the Mg alloy part, the plot illustrates that the majority of c-axes are aligned with the compression direction. Those textures are typical compression textures for each fcc and hcp metals and can be explained by the low critical resolved shear stresses of active slip systems.

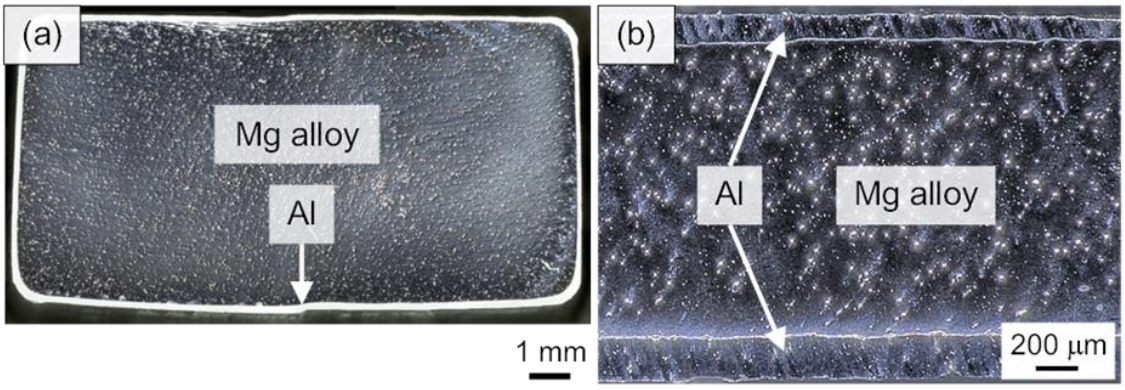

Fig. 5.3 Cross-sectional pictures of (a) Al-coated Mg alloy plate and (b) Al-coated Mg alloy sheet.

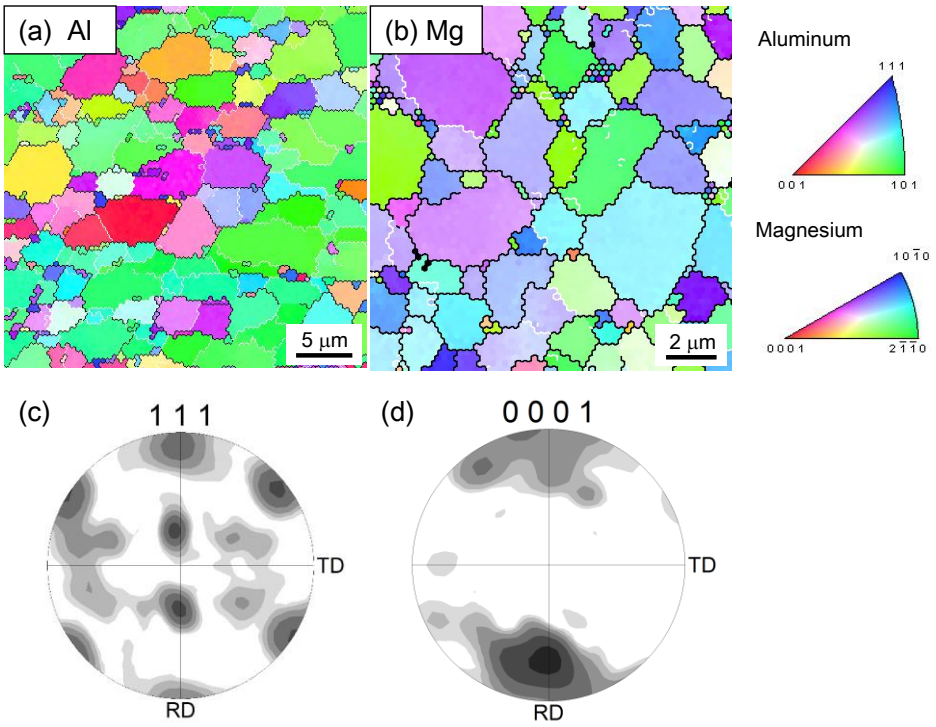

Fig. 5.4 EBSD orientation maps and intensity plots obtained from: (a) and (c) Al coating layer and (b) and (d) Mg alloy substrate in the Al-coated Mg alloy sheet. Forging direction is vertical and the extrusion direction is normal to this paper. The black and white boundary lines in (a) and (b) represent high (more than 15 °) and low (2 ° to 15 °) angle grain boundaries. In the intensity plots, RD and TD indicate the same directions as in (a) and (b).

5.4 Corrosion resistance

5.4.1 Experimental

The hot-forged Al-coated Mg alloy sheet, uncovered Mg alloy and pure Al used in this study were subjected to the corrosion test. The weight losses per unit surface area of the samples were measured in a 0.5 mass%HCl aqueous solution at room temperature. The detailed procedures are identical to the ones described in Chapter 2.

5.4.2 Results and discussion

Figure 5.5 exhibits the weight losses of the samples in the HCl aqueous solution with respect to immersion time. The uncovered Mg alloy started to dissolve severely soon after the sample immersion, while the fabricated Al-coated Mg alloy sheet did not dissolve at all, same as the pure Al. Consequently, it was found that the Al-coated Mg alloy sheet still possesses the satisfactory corrosion protection even after the severe forging deformation through the sheet formation.

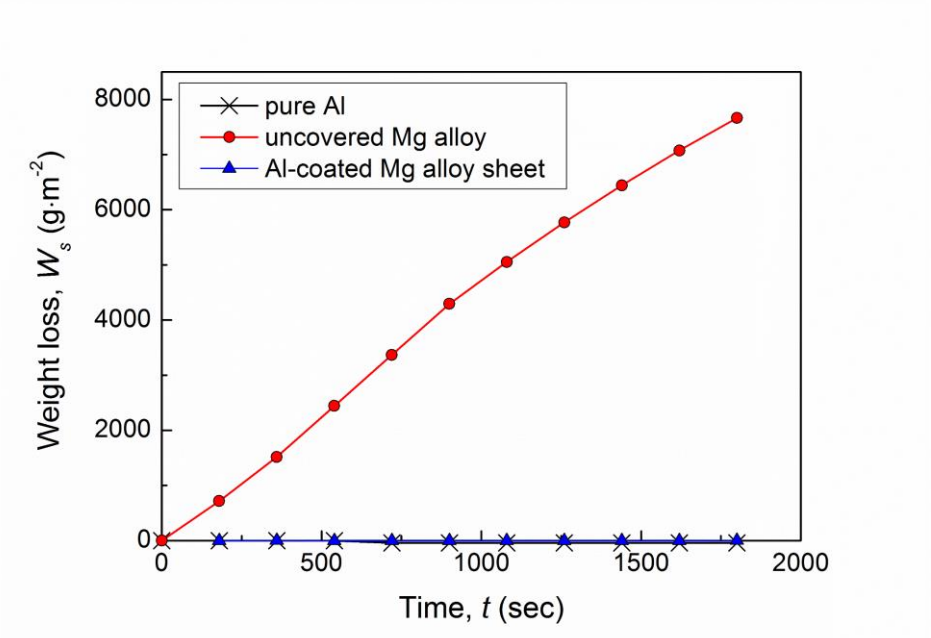

Fig. 5.5 Weight loss versus immersion time for various samples being immersed in 0.5 mass% HCl aqueous solution at room temperature.

5.5 Summary

In this chapter, the fabrication feasibility of the Al-coated Mg alloy sheet by hot forging was investigated. The Al coating remains on the Mg alloy substrate perfectly even after the severe plastic deformation of hot forging. The microstructure observation revealed that the grain refinement in both the Al coating layer and the Mg alloy substrate by recrystallization attributable to the hot forging process. Consequently, it was indicated that the Al-coated Mg alloy extrudate is capable of subsequent forming with maintaining the excellent corrosion resistance.

Considering industrial applications of the Al-coated Mg alloy sheet, the deformability of the sheet should be clearly specified. In Chapter 6, the mechanical property of the sheet is investigated by a tensile test and the sheet deformability is demonstrated.

Chapter 6

Tensile deformation behavior of Al-coated Mg alloy sheet

6.1 Introduction

In Chapter 5, it was demonstrated that the Al-coated Mg alloy sheet can be fabricated by hot extrusion followed by hot forging. Since the deformability and mechanical properties of the sheet are of primary importance to practical application of the sheet, the tensile properties of the Al-coated Mg alloy sheet should be investigated. In this chapter, the bondability and deformability of the Al coating layer during the tensile test are particularly focused and the deformability of the sheet is evaluated.

6.2 Experimental

The Al-coated Mg alloy sheet was wire-cut by using an electric discharge machine to prepare tensile specimens of 5.0 mm in gage length, 1.2 mm in width and 1.5 mm in thickness. The longitudinal direction of the tensile specimen is perpendicular to both the extrusion and forging directions. The tensile tests were conducted at five different initial strain rates of 1.0×10^{-2}, 7.5×10^{-3}, 5.0×10^{-3}, 3.0×10^{-3} and 1.0×10^{-3} s^{-1} and at six different temperatures of room temperature (RT), 473, 498, 523, 548 and 573 K. In all conditions, the tests were conducted more than two times to confirm the repeatability. The strain was calculated from the displacement of the crosshead. After the tensile tests, the specimens were embedded in a resin to preserve the coating form and then they were longitudinally sectioned and polished to observe the cross section and the Mg/Al interface.

6.3 Results and discussion

6.3.1 Deformability of the Al-coated Mg alloy sheet

Figures 6.1 (a) and (b) show the effects of temperature on the stress- strain curves of the tensile tests at strain rates of 1.0×10^{-2} s^{-1} and 1.0×10^{-3} s^{-1}, respectively. At room temperature, the stress immediately drops after reaching a peak at both the strain rates,

while at elevated temperatures, the stress gradually decreases as the strain increases after the peak. The peak stress decreases as the test temperature increases and as the strain rate decreases. The maximum elongation of 550 % was obtained when it was tensile-tested at 573 K and at 1.0×10^{-3} s^{-1}. Figure 6.1 (c) depicts the full images of the tensile specimens before and after the tensile test under a condition where the maximum elongation was obtained. From the pictures, it is clear that the Al-coated Mg alloy sheet exhibited a superior deformability.

6.3.2 Deformability of Al coating

Figure 6.2 shows the cross-sectional photographs of the specimen which showed 550 % of elongation at 573 K and at 1.0×10^{-3} s^{-1}. These photographs clearly illustrate that the Al coating continuously covers the Mg alloy substrate without breaking or debonding at the interface, despite such a large elongation. Furthermore, Fig. 6.3 illustrates the thickness change of the Al coating layer with respect to the distance from fracture surface. The average thicknesses of the Al coating layer after the hot extrusion [6.1] and hot forging are also presented. As is evident, the Al coating layer still has quite uniform thickness after 550 % of elongation owing to the homogeneous elongation of the whole specimen as shown in Fig. 6.1 (c). It is important to point out that not only the Mg alloy substrate but the Al coating layer was also elongated homogeneously.

Consequently, it can be concluded that the Al-coated Mg alloy sheet can be endure the subsequent forming process with perfect Al coating.

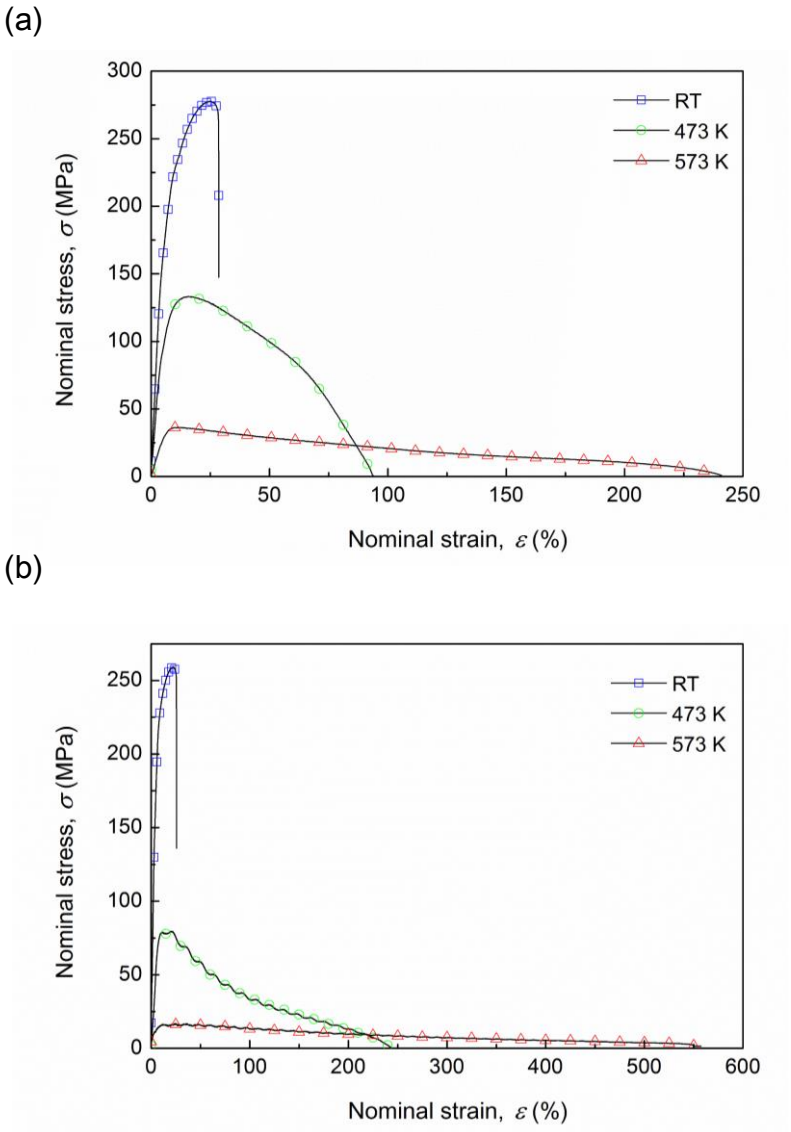

Fig. 6.1 Stress-strain curves of the Al-coated Mg alloy sheet, showing the temperature effect (a) at a strain rate of 1.0×10^{-2} s^{-1} and (b) at a strain rate of 1.0×10^{-3} s^{-1}. (c) The tensile specimens before and after the test showing the maximum elongation of 550 % at 573 K and at 1.0×10^{-3} s^{-1}.

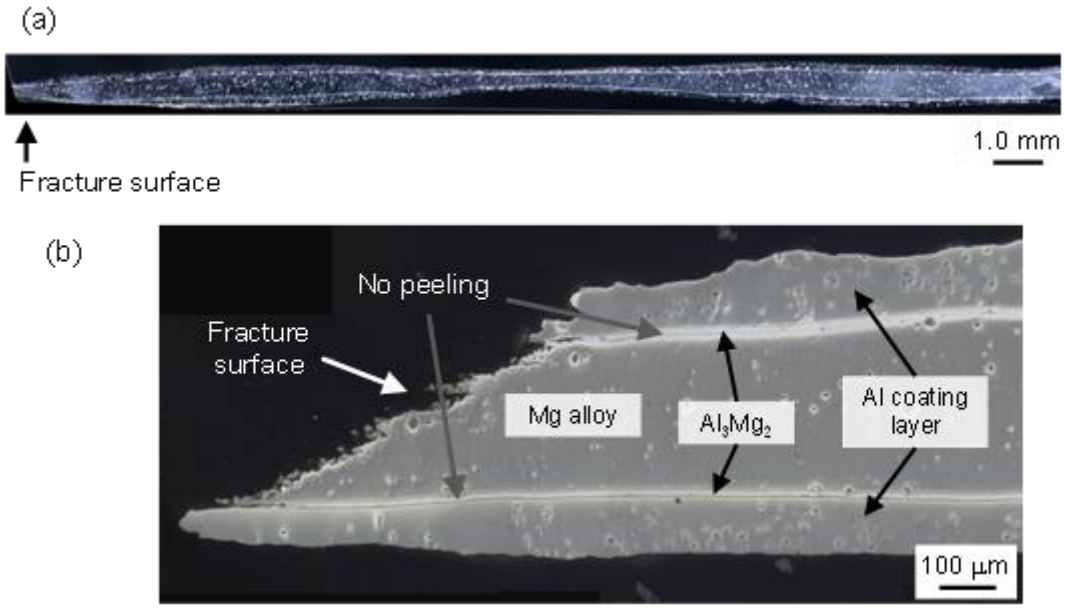

Fig. 6.2 Longitudinal cross section of the specimen elongated to 550 % at 573 K and at 1.0×10^{-3} s^{-1}; (a) global image and (b) Magnified image of the fractured part.

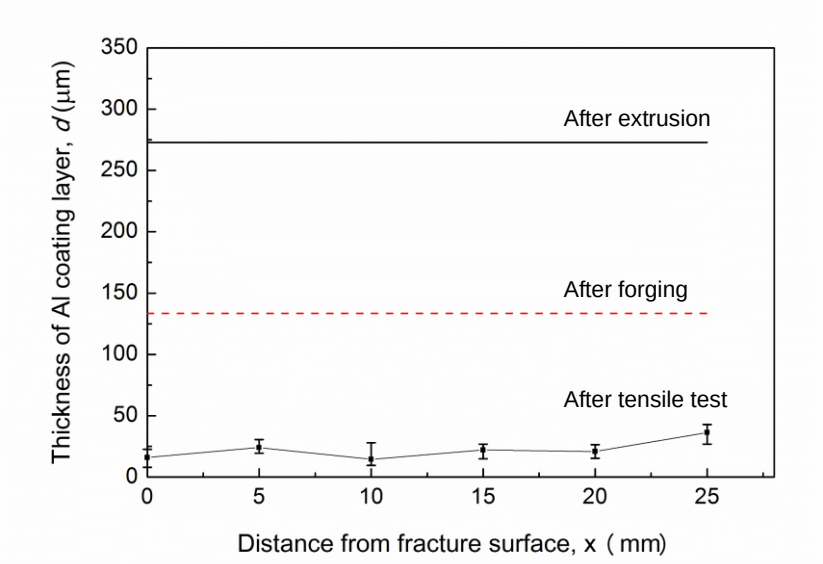

Fig. 6.3 Thickness change of Al coating layer with respect to the distance from the fracture surface in the tensile test at 573 K and at 1.0×10^{-3} s^{-1}. The average thicknesses of Al coating layer of the samples after the extrusion [6.4] and hot forging are also presented in the figure.

6.4 Summary

The tensile behavior of the Al-coated Mg alloy sheet has been investigated. The sheet exhibited a large elongation of 550 % at 573 K and at 1.0×10^{-3} s^{-1}. Notably, despite such a large elongation, the Al layer continuously and homogeneously coats the Mg alloy substrate without breaking or debonding and was elongated homogeneously.

Generally speaking, when metals exhibit such a large elongation at a high temperature and also at a low strain rate, one can consider that this composite material exhibits the superplasticity. In order to investigate if the focused deformation should be classified into the superplasticity or not, detailed study is performed in the next chapter. As summarized above, it was indicated that the Al coating layer exhibited such a large elongation together with the Mg alloy substrate. Although the superplastic characteristics in Mg alloys are quite well known, there has been no report of any pure Al superplasticity under the conditions used in this study regarding temperature, strain rate and grain size [6.2]. Therefore, in the next chapter, the deformation mechanisms of both Mg alloy and Al in the sheet are discussed in detail. In addition, in the next chapter, it is discussed how the intermetallic compound, formed at the interface between the Al layer and Mg alloy substrate, behaves during the tensile test.

References

[6.1] T. Tokunaga, K. Matsuura, M. Ohno, Aluminum coating on magnesium-based alloy by hot extrusion and its characteristics. *Mater. Trans.* **53** (2012) 1034-1041.

[6.2] H. Oikawa, Strain rate-temperature-grain size diagram of high-temperature deformation mechanisms for aluminum. *J. Jpn. Inst. Light Met.* **30** (1980) 376-383 (*in Japanese*).

Chapter 7

Deformation mechanism of the Al-coated Mg alloy sheet

7.1 Introduction

It is significantly important to understand and control the deformation behavior of the Al-coated Mg alloy sheet to industrially apply this composite sheet. As mentioned in Chapter 6, the Al-coated Mg alloy sheet exhibited a large and homogeneous elongation of 550 % at 573 K and at 1.0×10^{-3} s^{-1} without any breakings or debondings of the Al coating layer. Actually, such a large elongation recalls superplasticity phenomenon. Therefore, in the present chapter, firstly the sheet is evaluated to determine whether it meets the general definition of superplasticity or not. Subsequently, the deformation behavior of the sheet is examined in detail by means of the microstructure observation and crystallographic investigation. Consequently, the deformation mechanisms of both the constitutive materials of the sheet, Al and Mg alloy, are demonstrated.

7.2 Superplasticity evaluation of the Al-coated Mg alloy sheet

As stated above, the Al-coated Mg alloy sheet exhibited a large elongation, which is suggestive of superplasticity. Actually, it is well-known that when Mg alloys have fine microstructures, they are likely to exhibit superplasticity. However, it is still uncertain whether the large elongation of the present sheet can be classified as superplasticity or not. Therefore, in this section, the deformation behavior of the sheet is evaluated in terms of the strain rate sensitivity index. However, in order for the proper evaluation, it is important to understand the index, therefore, firstly the basic explanation of the index is given below.

7.2.1 Strain rate sensitivity index [7.1]

Superplasticity is characterized by the abnormally large elongation. It has been pointed out that in order to achieve such a large elongation, a strain-induced hardening is required to compensate the geometrical weakening, attributable to reduction in cross section *viz.* necking [7.1]. Phenomenologically, the hardening, leading to the necking suppression, has been explained with the strain rate and therefore, the strain rate

sensitivity index has been introduced as one of the criteria for superplasticity. In the following sections, the basic idea of the strain rate sensitivity index is explained and the Al-coated Mg alloy sheet is evaluated by this index. Consequently, the large elongation of the Al-coated Mg alloy sheet is evaluated whether it can be classified as superplasticity or not.

7.2.1.1 Definition of the strain rate sensitivity index

As briefly mentioned above, it has been suggested that the hardening, suppressing the necking initiation, should strongly depend on the strain rate. Therefore, the strain rate sensitivity index, *m*-value, has been introduced to provide a quantitative indication for the strain rate sensitivity of target materials [7.1]. The *m*-value can be obtained by evaluating *m* in the following empirically-developed rheological stress-strain relationship [7.1, 7.2];

$$\sigma = K\dot{\varepsilon}^m \tag{7.1}$$

where σ is the flow stress, *K* is a material constant and $\dot{\varepsilon}$ is the steady state strain rate. From Eq. (7.1), when temperature is constant, the *m*-value is defined as the slope of a double logarithmic plot of flow stress versus strain rate and can be expressed as [7.2];

$$m = \frac{\partial(\ln \sigma)}{\partial(\ln \dot{\varepsilon})} \tag{7.2}$$

Considering the definition of the stress, Eq. (7.1) can be rewrite as;

$$\sigma = K\dot{\varepsilon}^m = \frac{F}{A} \tag{7.3}$$

where *F* is force being transmitted through a cross-sectional area, *A*. Putting *l* as the initial length of a specimen, the strain can be expressed as follows;

$$\varepsilon = \frac{dl}{l} \tag{7.4}$$

Assuming that the target is an incompressible material, the strain rate at any point in the material is;

$$\dot{\varepsilon} = \frac{1}{l}\frac{dl}{dt} = -\frac{1}{A}\frac{dA}{dt} \tag{7.5}$$

Combining Eq. (7.3) and Eq. (7.5),

$$-\frac{dA}{dt} = \left[\frac{F}{K}\right]^{\frac{1}{m}} \left[\frac{1}{A^{\left(\frac{1-m}{m}\right)}}\right] \tag{7.6}$$

The left-hand side of Eq. (7.6) indicates the reduction rate of the cross-sectional area, therefore, as long as *m* is less than 1, the smaller the cross section is, the more rapidly it is reduced. As *m* approaches 1, the sensitivity of the cross section to the reduction rate decreases, that is, the material becomes stable toward the necking initiation.

7.2.1.2 Strain rate sensitivity index of the Al-coated Mg alloy sheet

Figure 7.1 depicts the double logarithmic plots of the stress versus strain rate at temperatures of 473 and 573 K in the present tensile tests. Here, the stress represents the stress at a strain, ε, of 0.1, which can be considered as the initiation point of steady state. From the figure, it was found that the *m*-values of the present Al-coated Mg alloy sheet were approximately 0.2 at 473 K and 0.4 at 573 K. Generally, the superplasticity is characterized by an elongation of more than 200 % and an *m*-value of more than 0.3 [7.3, 7.4]. Thus, the large elongation of the present Al-coated Mg alloy sheet at a temperature of 573 K and at a strain rate of 1.0×10^{-3} s^{-1} is classified into superplasticity.

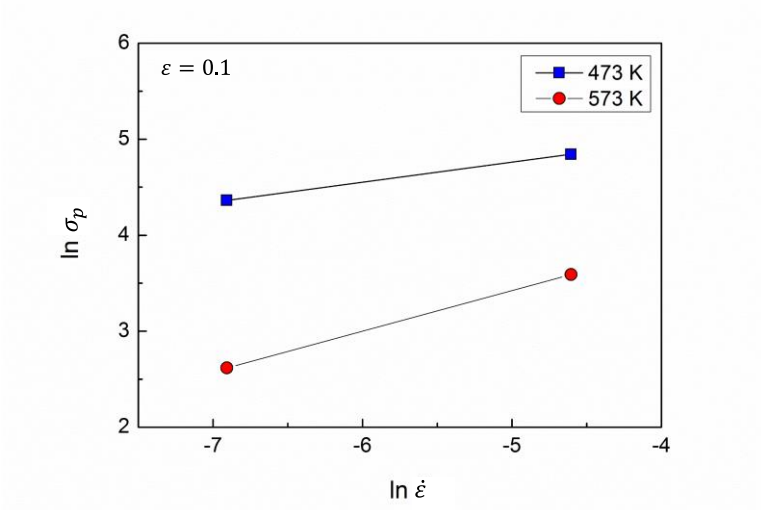

Fig. 7.1 Double logarithmic plots of stress (at ε = 0.1) versus strain rate at temperatures of 473 and 573 K.

7.3 Brief review of superplasticity

Superplasticity is characterized by an extremely large elongation without fracture. Such unusual behavior is of interest to many researchers and accordingly, superplasticity has been studied to a great extent. In the present section, in order for the better understanding of the deformation behavior of the present Al-coated Mg alloy sheet, superplasticity is reviewed briefly with a special attention to the deformation mechanisms.

7.3.1 Fundamental characteristics

Superplasticity occurs based on the internal factors such as fine, homogeneous, isotropic and heat-stable microstructures and also as well as the following external factors of a high temperature above a half of the melting point and relatively low strain rate in a range of about 1.0×10^{-4} to 1.0×10^{-3} s^{-1}. Accordingly, superplastic materials possess the specific characteristics such as a high *m*-value, high flow stress dependencies on the temperature and grain size, and texture randomization and equiaxed grains after deformation.

7.3.2 Deformation mechanisms

To date, a great deal of the deformation mechanisms have been proposed for superplasticity. However, there is only limited understanding for the deformation process and no solid deformation mechanism for superplasticity. Based on the many existing research works, it has been indicated that superplasticity cannot be described by a unique deformation mechanism of its own, but more likely to be interpreted by a combination of different mechanisms e.g. diffusional processes, dislocation and grain boundary migration and grain boundary sliding (GBS) [7.5]. Major models, which govern the superplastic deformation, are explained below.

7.3.2.1 Diffusion creep model

This model states that superplasticity can be explained with the atomic diffusion. Deformation occurs by the diffusion of vacancies and counterflux of atoms. This model can explain well the strain rates of the whole specimen, however, there are fatal drawbacks as follows;

1. Only very little grain elongation can occur, not sufficient for superplasticity.

2. This model cannot explain the grain rotation motion which is usually observed experimentally.

3. Because of the grain elongation and consequent increase of diffusion path, this model is self-extinguishing model and cannot account for the large elongation of superplasticity.

Consequently, this diffusion creep model cannot be considered as a dominant deformation mechanism of superplasticity.

7.3.2.2 Dislocation motion model

This model accounts for the deformation of superplasticity with the dislocation motion. A number of researches have been conducted, however, this model cannot sufficiently explain the observed facts of superplasticity e.g. texture randomization and equiaxed grain development after deformation. Therefore, this model also has not been considered as a possible model.

7.3.2.3 Grain boundary sliding model

This model explains the deformation with GBS, which conforms to a number of experimental facts. Actually, there are several evidential tracks of GBS such as marker experiment results and texture measurements, and therefore, this model has been considered as the most reasonable model to describe superplasticity.

7.3.3 Grain boundary sliding with accommodation processes [7.5-7.9]

From the reviews above, GBS seems to be the dominant deformation process for superplasticity. However, GBS cannot fully explain superplasticity alone because of some geometric inconsistency. As shown in Fig. 7.2, when GBS arises, because of the nature of the grains, keeping their shapes, the grain overlapping or void generation should occur inevitably near the triple-junction or grain boundaries. Thus, for the solid continuity, an accommodation process is required. Accordingly, the deformation mechanisms of superplasticity can be sorted by the accommodation processes associated with GBS. Thus, the deformation mechanisms with the dominant accommodation processes are explained as follows.

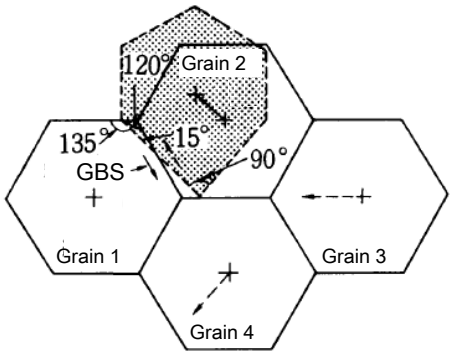

Fig. 7.2 Geometrical relationship of the grains before (open) and after (shaded) the grain boundary sliding [7.6].

7.3.3.1 Grain boundary sliding with accommodation by dislocation motion

This model accounts for the accommodation process with dislocation motion in the grains. Because GBS leads to stress concentration, dislocations are generated and piled-up in the grain boundary, and subsequently GBS stops as depicted in Fig. 7.3. However, climb and dissipation of the dislocations can restart GBS and resolve the inconsistency originating from GBS. Consequently, such dislocation behavior is considered as the rate controlling process in this model. However, there has been no evidential support of this model such as dislocation pile-ups, therefore, this model is still under consideration.

7.3.3.2 Grain boundary sliding with accommodation by diffusion creep

The model explained with GBS accommodated by diffusion creep is schematically illustrated in Fig. 7.4 (a). In this model, the aforementioned inconsistency is accounted for the material motion by the diffusion creep; Coble creep based on the grain boundary diffusion (Fig. 7.4 (b)) or the Nabarro-herring creep based on the lattice diffusion (Fig. 7.4 (c)). This model is based on the so-called “grain switching event”. This grain switching can be topologically characterized by the change of neighbor grains, which allows the large elongation of the specimen without requiring any grain elongations. In fact, this grain switching has been observed during in-situ deformation of the Zn-Al eutectoid alloy in the high-voltage electron microscope [7.5]. Therefore, this model can be a considerable promise as an accommodation process for GBS.

As a developed model of the aforementioned grain switching model, with a three dimensional point of view, “grain emerging process” model shown in Fig. 7.5, has been

proposed. Firstly, a small amount of deformation generates a small and narrow space (Fig. 7.5 (a)). Then this gap is enlarged and filled by the enlarged grain coming from the lower plane (Fig. 7.5 (b)) and finally, the grain-boundary network adjusts to maintain correct dihedral angles (Fig. 7.5 (c)).

As demonstrated in this section, a number of models have been proposed, and basically those models are combined with diffusional phenomena. In the next section, the deformation mechanism of the Al-coated Mg alloy sheet is discussed.

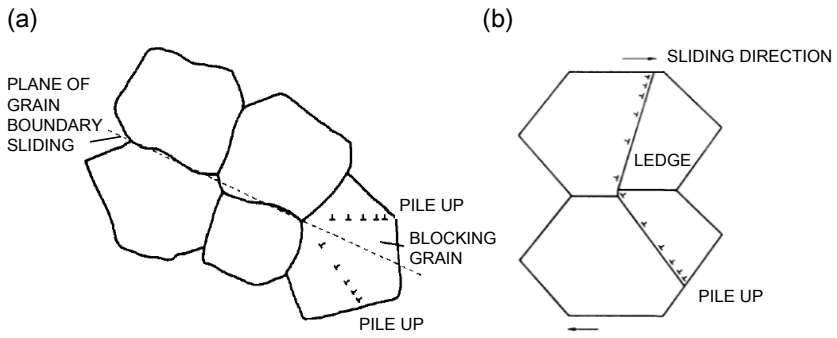

Fig. 7.3 Dislocation pile up models; (a) Ball & Hutchinson model and (b) Mukherjee model [7.5, 7.6].

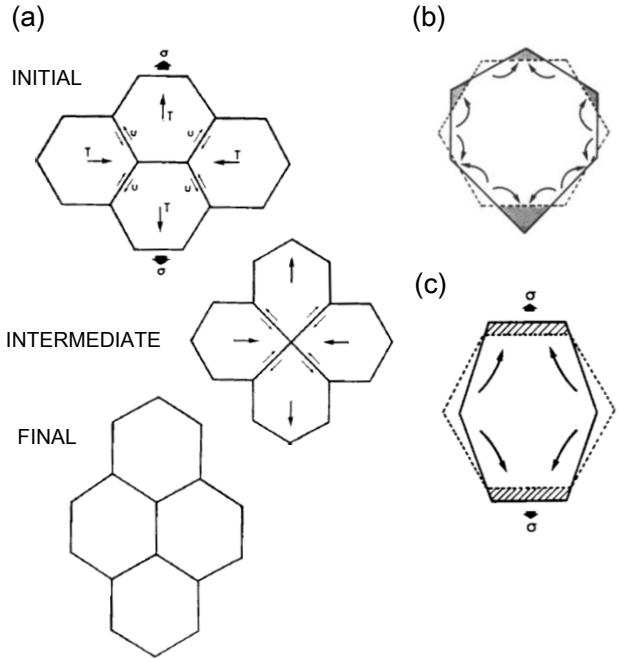

Fig. 7.4 Schematic drawings of (a) grain switching model, (b) and (c) diffusional accommodation at the intermediate stage of the switching process in (a) [7.7].

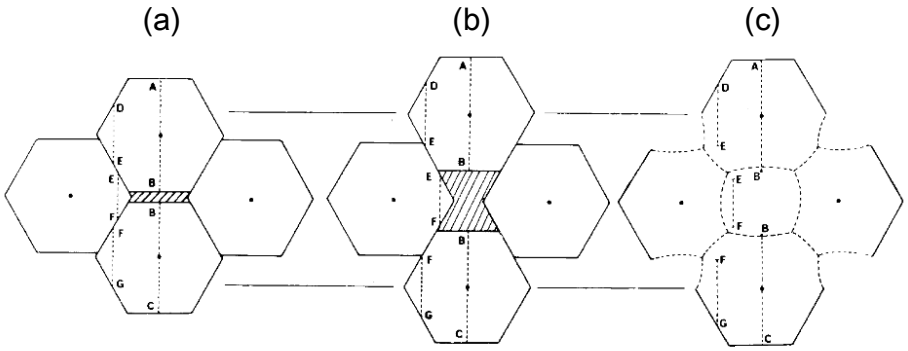

Fig. 7.5 Grain emerging process model [7.8].

7.4 Deformation mechanism of the Al-coated Mg alloy sheet

In the earlier sections, it has been demonstrated that the present Al-coated Mg alloy sheet exhibited superplasticity. As explained in section 7.3.2, a number of processes seem to be involved during superplasticity. Thus, in this section, in order to investigate the dominant deformation mechanism of the Al-coated Mg alloy sheet, the microstructure and crystallographic observations are conducted.

Since the majority material of the present Al-coated Mg alloy sheet is Mg alloy, the volume fraction of which was about 82 %, it has been considered that the deformation mechanism of the sheet is dominated by that of the Mg alloy substrate. Therefore, the deformation mechanism of the Mg alloy substrate is investigated as the representative of the whole sheet, in this section.

7.4.1 Deformation behavior of Mg alloy substrate

7.4.1.1 Crystallographic observation

In order to investigate the deformation mechanism, the microstructure and crystallographic evolutions observed in the tensile test are investigated on the Mg alloy substrate.

Figures 7.6 (a) and (b) illustrate the inverse pole figures, obtained from the electron backscatter diffraction (EBSD) analysis for the Mg alloy substrate before and after the tensile test, respectively. The specimen, which exhibited superplasticity, was selected to be investigated as a representative. The black and white boundary lines represent high (more than 15 ^{o}) and low (2 ^{o} to 15 ^{o}) angle grain boundaries respectively, and the forging and tensile directions correspond to the vertical and transverse directions in the figures,

respectively. From the figures, grain coarsening is clearly observed with the grain size change from 2.0 to 8.1 μm. Notably, the grains are not elongated and still equiaxed even after the 550 % of elongation of the specimen. Figures 7.6 (c) and (d) depict the {0001} pole figures, vertically-corresponding to the above inverse pole figures. As illustrated in Fig. 7.6 (c), after the hot forging, Mg alloy possesses the compression texture and the *c*-axes are aligned with the forging direction, while after the tensile test, the texture was randomized as is clear from Fig. 7.6 (d). The generation of the equiaxed grains and texture randomization after the tensile test indicate that the deformation was accompanied by GBS. Therefore, it was confirmed that the Al-coated Mg alloy sheet exhibited the superplasticity with the help of GBS during the tensile test at 573 K and at 1.0×10^{-3} s^{-1} [7.2].

Although, it was found that the dominant deformation is GBS during the superplastic deformation, as mentioned earlier, the accommodation processes should be carried out at the same time. Therefore, for the deeper understanding of the deformation mechanisms of the Al-coated Mg alloy sheet, fractography analysis is performed next.

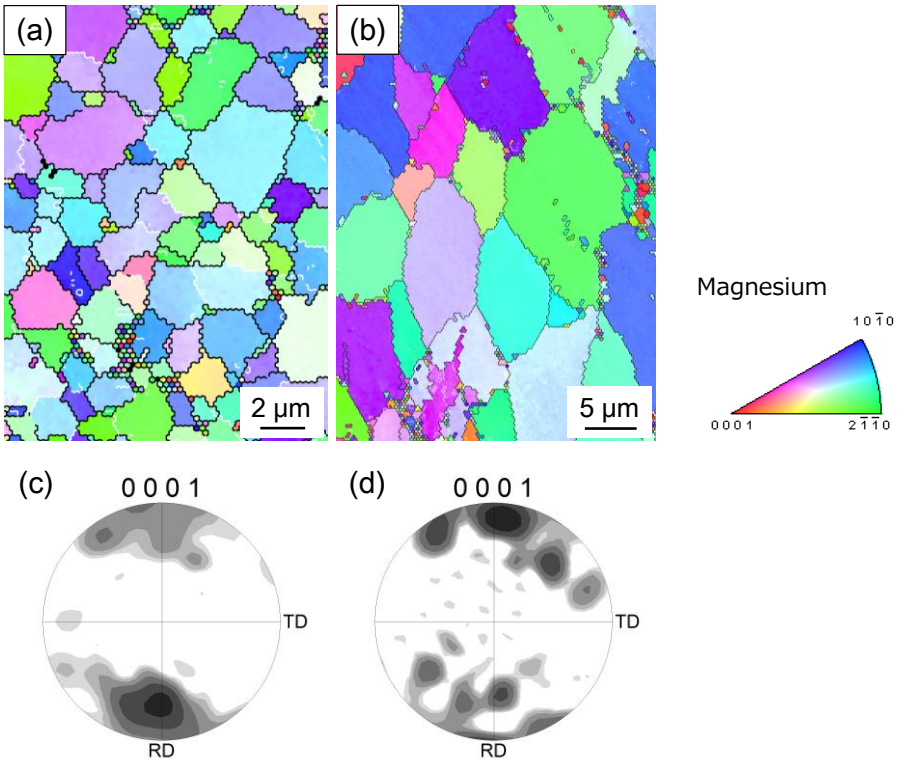

Fig. 7.6 (a) and (b); Inverse pole figures of the Mg alloy substrate in as-forged sheet and after 550 % of elongation. (c) and (d); pole figures obtained from (a) and (b). Tensile direction is transverse, forging direction is vertical and the extrusion direction is normal to this paper. The black and white boundary lines in (a) and (b) represent high (more than 15 °) and low (2 ° to 15 °) angle grain boundaries. In the pole figures, RD and TD indicate the same directions as in (a) and (b).

7.4.1.2 Fractography

Figure 7.7 depicts the scanning electron microscope (SEM) images of the fracture surface of the tensile specimen showing the superplastic elongation of 550 %. Figures 7.7 (a), (b) and (c) exhibit the low magnified image of the fracture surface, high magnified image of the Mg alloy part in the fracture surface and the higher magnified image of the region indicated by a square in (b), respectively. As can be seen in Fig. 7.7 (a), many large and small holes exist in the Mg alloy substrate. It is known that the cavity nucleation occurs during superplasticity and the fracture follows the connections of the cavities [7.10-7.15]. Therefore, it can be deduced that the large holes formed in the cavity interlinkage stage and small holes formed in the final fracture stage. In Figs. 7.7 (b) and (c), the surfaces of individual grains are clearly visible, which is typical for the superplastic materials. Those grains can be classified into two types of grains, which have

smooth and rough surfaces. These grains are indicated as Grain S and Grain R in Fig. 7.7 (c). It is reported that this rough surface forms in the final stage of the deformation [7.15]. Thus, it can be considered that Grain R separated from other grains just before the fracture initiation, while Grain S are believed to have separated due to the cavity formation. It is known that GBS triggers cavity formation, thus this result can also support the deformation mechanism of GBS for superplasticity [7.14].

Additionally, filaments were observed on the grains in the fracture surface as indicated by arrows in Fig. 7.7 (c). Formation of the filaments is known as one of the micro-superplasticity phenomena [7.16]. This phenomena have been observed in a number of superplastically deformed materials [7.16-7.29] and several mechanisms for the filament formation have been reported; (1) viscous flow due to the existence of liquid-like or semi-liquid phase [7.17-7.25]; (2) single crystalline plasticity [7.26, 7.27]; (3) severe elongation of cavities under the tensile stress [7.28]; (4) diffusion creep [7.29]. The test temperature, 573 K, is no higher than $0.81T_m$ of the eutectic temperature of Mg-Al alloy, 710 K. Thus, the viscous flow resulted from the partial melting was impossible in the present study. Moreover, the present fracture surface did not show O-shaped cavities among the filaments, which is characteristic of the cavity elongation mechanism (3). Therefore, single crystalline plasticity mechanism (2) or diffusion creep (4) are the most likely mechanisms to realize the filament growth in the present alloy. However, it is noteworthy here that it has been suggested that the rough surface of Grain R formed during dislocation creep, which has the same basic mechanism as diffusion creep [7.15]. Considering this as a supportive evidence, it can be concluded that the filament gradually formed when the fracture occurred due to the diffusion creep [7.29].

Consequently, it has been demonstrated that the sheet exhibited superplasticity based on GBS with conceivable accommodation processes of diffusion creep and dislocation motion. In the next section, in order to understand the sheet deformation in more detail, the rate-controlling process is evaluated based on the activation energy.

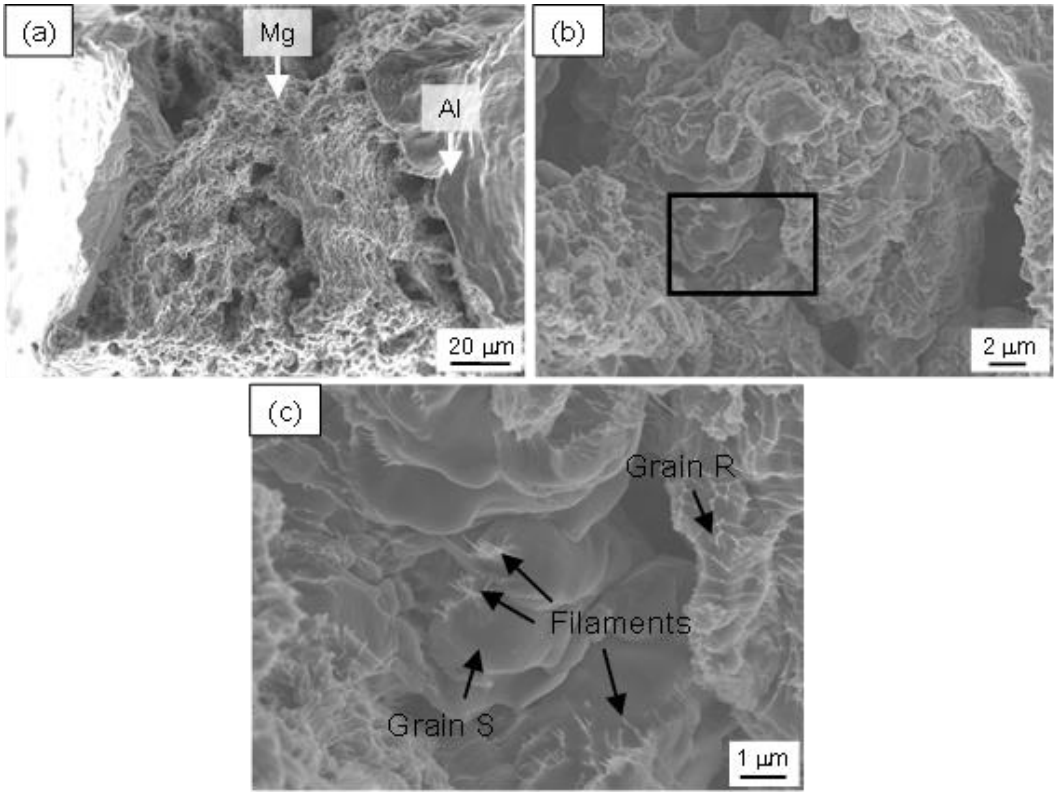

Fig. 7.7 SEM fractographs of the tensile fracture surface of the specimen after 550 % of elongation: (a) low magnified image, (b) high magnified image of the Mg alloy part and (c) higher magnified image of the region indicated by square in (b). The grains having smooth and rough surfaces are indicated by arrows as Grain S and Grain R, respectively.

7.4.2 Activation energy

In order to investigate the rate-controlling process, the apparent activation energy for the superplastic deformation of the sheet is investigated. In the thermally activated mechanism of superplasticity, the strain rate can be generally described as [7.30];

$$\dot{\varepsilon} = \left(\frac{AGb}{kT}\right)\left(\frac{\sigma}{G}\right)^{n} \exp\left(-\frac{Q}{RT}\right) \tag{7.7}$$

where A is a constant, G is shear modulus, b is burgers vector, k is Boltzmann constant, n is stress exponent (=1/m), R is gas constant, T is temperature and Q is the activation energy, which is dependent on the rate-controlling process. Figure 7.8 shows the plots of natural logarithm of stress versus reciprocal of temperature at strain rates of 1.0×10^{-2} and 1.0×10^{-3} s^{-1}. The stress values were taken at the strain of 0.1 like in the previous section. From

Eq. (7.7), the slopes of those lines, shown in Fig. 7.8, express Q/nR. Therefore, the apparent activation energies for the Al-coated Mg alloy sheet are 101 and 141 kJ/mol at strain rates of 1.0×10^{-2} and 1.0×10^{-3} s^{-1}, respectively. It is reported that the activation energies for pure Mg are 92 and 135 kJ/mol [7.31] and approximately 80 and 170 kJ/mol [7.32-7.34] for AZ80 Mg alloy, for pipe diffusion and lattice diffusion, respectively. Therefore, it seems that the present superplastic deformation of the Al-coated Mg alloy sheet is controlled by pipe diffusion at lower temperatures and by lattice diffusion at higher temperatures.

Up to here, the deformation mechanism of the Al-coated Mg alloy sheet has been demonstrated that the sheet exhibited superplasticity with the dominant deformation mechanism of GBS with the rate-controlling process of lattice diffusion. However, there is a concern about Al coating, which was deformed superplastically together with Mg alloy substrate. Although the superplasticity of Mg alloys are well-known, there has been no report of any pure Al showing superplasticity under the conditions used in this study regarding temperature, strain rate and grain size [7.33]. Therefore, in the next section, the deformability of the present pure Al and Mg alloy are confirmed individually.

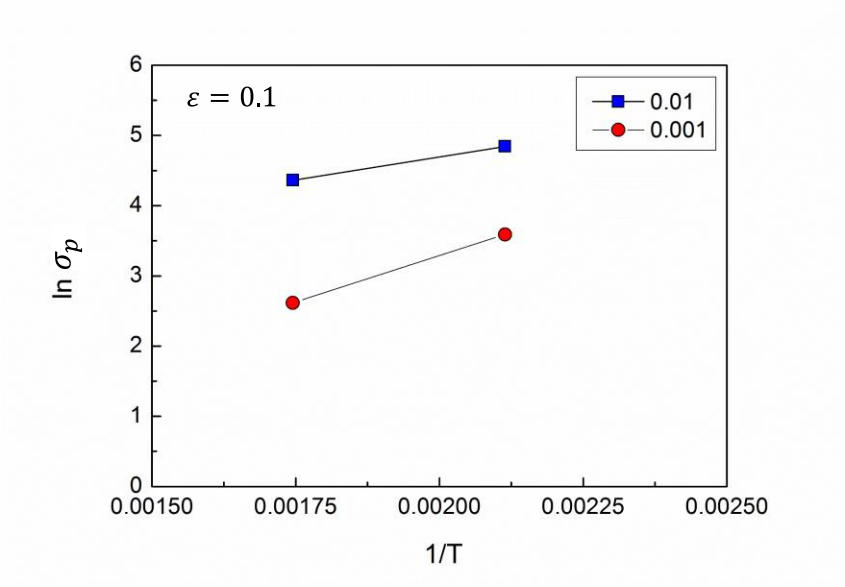

Fig. 7.8 Plots of natural logarithm of stress versus reciprocal of temperature at strain rates of 1.0×10^{-2} and 1.0×10^{-3} s^{-1}.

7.5 Individual deformation behavior of Mg alloy and pure Al

7.5.1 Experimental

For the fabrication of the tensile specimens, both Mg alloy and pure Al billet were separately extruded and then each of them was hot-forged. The tensile specimens of each material were fabricated in the same manner as for the Al-coated Mg alloy composite, explained in Chapters 5 and 6.

The tensile tests were conducted at seven different initial strain rates of 1.0×10^{-2}, 5.0×10^{-3}, 2.0×10^{-3}, 1.5×10^{-3}, 1.0×10^{-3}, 6.0×10^{-4} and 2.0×10^{-4} s^{-1} and at six different temperatures of room temperature (RT), 473, 498, 523, 548 and 573 K. All the test conditions are summarized in Table 7.1. The strain was calculated from the displacement of the crosshead. In order to evaluate the deformation, *m*-value and the activation energy, *Q*, were investigated.

Table 7.1 Tensile test conditions for each Mg alloy and pure Al.

Al		Mg	
Temperature (K)	Strain rate (s^{-1})	Temperature (K)	Strain rate (s^{-1})
473	2×10^{-3}	RT	1×10^{-2}
	1.5×10^{-3}		1×10^{-3}
498	1×10^{-3}	473 523 573	1×10^{-2}
523	6×10^{-4}		5×10^{-3}
548	2×10^{-4}		2×10^{-3}
573	2×10^{-3}		1.5×10^{-3}
	1.5×10^{-3}		1×10^{-3}
	1×10^{-3}		6×10^{-4}
	4×10^{-4}	498 548	2×10^{-3}
	2×10^{-4}		1.5×10^{-3}
			1×10^{-3}
			6×10^{-4}
			2×10^{-4}

7.5.2 Results

7.5.2.1 Mg alloy

Figure 7.9 illustrates the stress- strain curves obtained with Mg alloy. For the visual

simplification, only the selected results are presented here. All the obtained elongations are summarized in Table 7.2 and the maximum elongations at each temperature are highlighted using shaded letters. The largest elongation of 992 % was obtained at 548 K and at 6.0×10^{-4} s^{-1}. Basically, it can be said that as temperature increases and as strain rate decreases, the lager elongation and the smaller peak stress are obtained. From Table 7.2, it is clear that when the temperatures are low, the lower the strain rate is, the larger elongation is obtained, however, notably, the temperatures are high, the highest elongation is obtained not at the lowest strain rate, but at the second lowest strain rate. It can be considered this is due to the grain coarsening during the tensile tests.

Furthermore, from Fig. 7.9, significant sensitivity of the shape of the curves to the temperature can be seen at each strain rate. When the temperatures are lower, and especially at higher strain rates, the curves clearly show the sharp peaks, however, on the other hand, at higher temperatures, the flow stresses show the stable values and there are no sharp peaks observed. Furthermore, it is worth noting that the oscillations in the stress-strain curves arose at most of the conditions. Basically, these oscillations are considered as the evidence of Dynamic Recrystallization (DRX) and therefore, it can be considered that this Mg alloy exhibited DRX owing to the fine microstructures, like the one in the Al-coated Mg alloy sheet.

Figure 7.10 illustrates the double logarithmic plots of the true stress versus strain rate for the *m*-value. The results are summarized in Table 7.3. Here, the true stress represents the peak value at each tensile condition and was calculated under the assumption that the volume was fixed. All the plots are reasonably fitted to the linear relationship. From the plots, it seems that the specimens tensile-tested at 573 K and at lower strain rates exhibited a particular behavior, however, the condition at this strain rate is over the interest of this study, therefore further investigation has not conducted. From these data, it was found that the *m*-values are over 0.3 at temperatures of 498 and 548 K and in other conditions, *m*-values are over 0.25 except at 573 K. Consequently, it can be said that basically the present Mg alloy exhibited high *m*-values and possesses the potential for the superplastic deformation under the present study conditions.

Figure 7.11 illustrates the plots for the activation energy, *Q*, and the obtained activation energies at each temperature are summarized in Table 7.4. As mentioned in the preceding paragraph, the deformation mechanism at a strain rate of 6.0×10^{-4} s^{-1} seems to be different from the others, therefore, only the linearly-fit values were utilized here for the calculation of *Q*. It can be seen that activation energies show almost the same values at all strain rates and the average activation energy is 135 kJ/mol, which is identical to the one for the lattice diffusion of pure Mg.

Consequently, the present Mg alloy exhibited superplasticity at 498 and 548 K and deformed with the rate controlling process of lattice diffusion. Furthermore, the obtained results here are quite similar to the ones obtained with the Al-coated Mg alloy sheet. Therefore, it has been confirmed that the assumption that the Mg alloy mainly governs the deformation behavior of the sheet is appropriate.

(a)

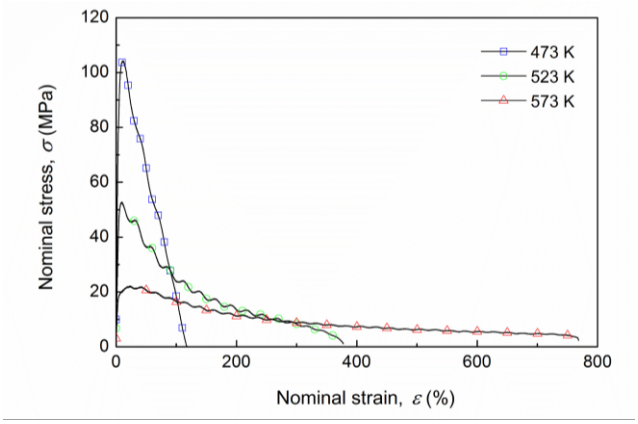

(b)

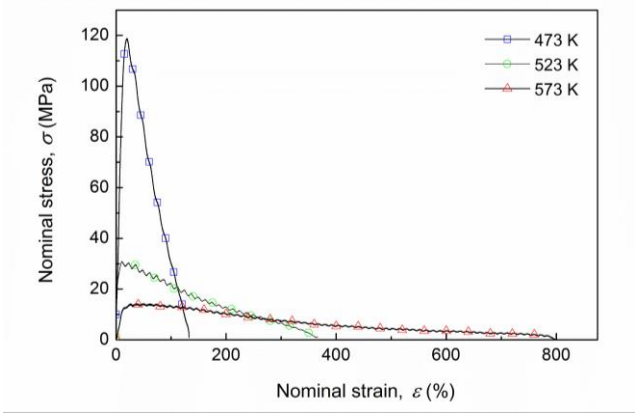

(c)

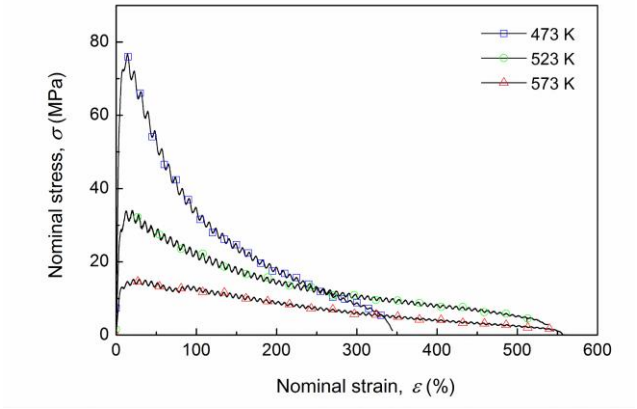

Fig. 7.9 Stress-strain curves obtained from the tensile tests of Mg alloy at variety of temperatures and at (a) 2×10^{-3}, (b) 1×10^{-3} and (c) 6×10^{-4} (s^{-1}).

Table 7.2 Summary of the total elongations at all conditions for the Mg alloy.

Mg alloy					
Temperature (K)	Strain rate (s^{-1})	Elongation (%)	Temperature (K)	Strain rate (s^{-1})	Elongation (%)
573	1.0×10^{-2}	530	498	2.0×10^{-3}	217
	5.0×10^{-3}	597		1.5×10^{-3}	203
	1.5×10^{-3}	695		1.0×10^{-3}	305
	1.0×10^{-3}	800		6.0×10^{-4}	364
	6.0×10^{-4}	560		2.0×10^{-4}	372
	2.0×10^{-4}	358	473	1.0×10^{-2}	137
548	2.0×10^{-3}	437		5.0×10^{-3}	103
	1.5×10^{-3}	714		2.0×10^{-3}	118
	1.0×10^{-3}	808		1.5×10^{-3}	307
	6.0×10^{-4}	992		1.0×10^{-3}	133
	2.0×10^{-4}	556		6.0×10^{-4}	345
523	1.0×10^{-2}	122			
	5.0×10^{-3}	217			
	1.5×10^{-3}	314			
	1.0×10^{-3}	366			
	6.0×10^{-4}	538			

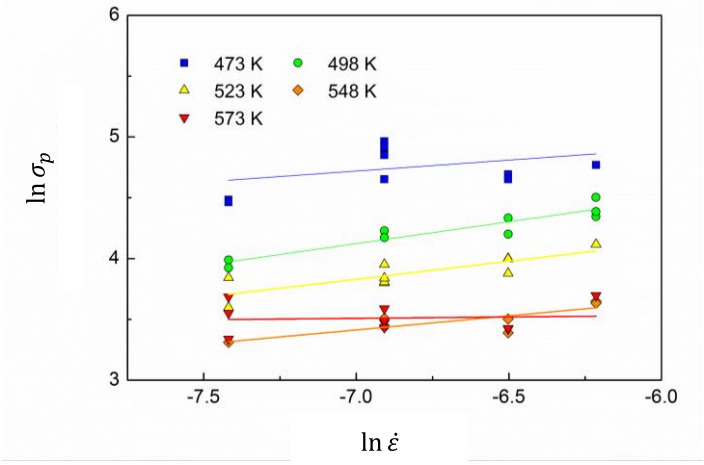

Table 7.3 Summary of *m*-value for the Mg alloy.

Temperature (K)	*m*-value
473	0.26
498	0.38
523	0.25
548	0.32
573	0.12

Fig. 7.10 Double logarithmic plots of true stress versus strain rate for the Mg alloy.

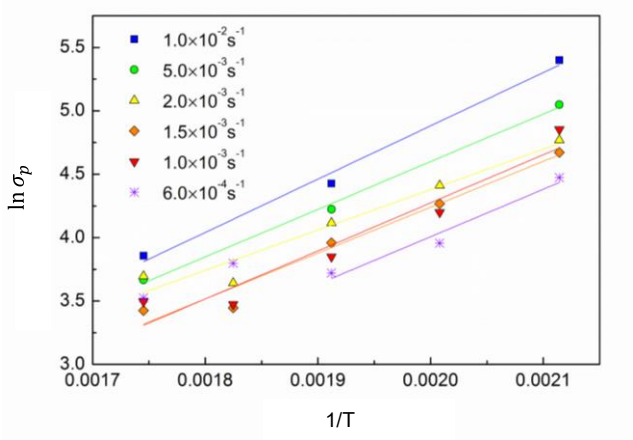

Table 7.4 Summary of *Q* for the Mg alloy.

Strain rate (s^{-1})	Activation energy (kJ/mol)
1.0×10^{-2}	153
5.0×10^{-3}	137
2.0×10^{-3}	116
1.5×10^{-3}	132
1.0×10^{-3}	138
6.0×10^{-4}	136

Fig. 7.11 Plots of natural logarithm of true stress versus reciprocal of temperatures for the Mg alloy.

7.5.2.2 Pure Al

Figure 7.12 illustrates the obtained stress-strain curves for the pure Al used as the coating material to produce the Al/Mg alloy composite, and all the obtained elongations are summarized in Table 7.5. The maximum elongation of the pure Al was 47 % at 573 K and at 2.0×10^{-3} s^{-1}. However, there are almost no differences in elongation depending neither on strain rates nor temperatures. Figure 7.13 illustrate the double logarithmic plots of true stress versus strain rate and the obtained *m*-values are summarized in Table 7.6. Here, the true stress represents the peak value at each tensile condition and was calculated under the assumption that the volume was fixed. As was clear in Fig. 7.12, the *m*-values are very small in all conditions. Furthermore, Fig. 7.14 shows the plots of natural logarithm of true stresses versus reciprocal of temperatures, and the obtained activation energies are depicted in Table 7.7. Since the activation energies for lattice diffusion and pipe diffusion are 142 and 82 kJ/mol [7.31], respectively, therefore, the major rate controlling process for the present pure Al can be deduced that pipe diffusion at lower temperatures and lattice diffusion at higher temperatures.

Notably, the elongations obtained from the tensile test of the pure Al specimen, are significantly less than the elongation found in the Al coating part in the same pure Al-coated Mg alloy sheet although the same pure Al material was used there. In other words, the results obtained from the tensile test of pure Al contradicts the fact that the same Al can be elongated to 550 % when it is used as the coating material on the Mg alloy surface. It is known that the brittle/ductile multilayered composites have been acknowledged to

have a remarkable enhancement of ductility and actually, much effort have been devoted in order to elucidate the mechanisms of ductility enhancement of the brittle material in the composite materials [7.35-7.37]. The major reason of the remarkable enhancement of ductility is due to load transfer from the brittle layer to ductile layer in the laminated composites owing to the interaction between the layers [7.38]. Generally, when necking occurs at a position in a tensile specimen, local elongation is accelerated in that region, resulting in the occurrence of fracture. However, as explained above, the load transfer occurs in the composite material. Namely, in the case of the present study, when the Al coating layer is bonded to the Mg alloy substrate, the necking and the subsequent local elongation of the Al coating is suppressed due to the uniform deformation of the superplastic Mg alloy.

It is also known that the load transfer delays the localized necking through the formation of multiple necking [7.39-7.41]. In the case of the present study, the multiple necking was observed in the highly-elongated specimen (Chapter 6, Fig. 6.2 (a)), therefore, the multiple necking can be an evidence of the occurrence of the load transfer.

Consequently, it is reasonable to consider that the Al-coated Mg alloy sheet in the present study underwent the load transfer, which can explain the large elongation of the pure Al as the coating material. However, actually, the interface characteristics are still unclear in the present study, and the above-mentioned enhancement theory cannot be realized without the good bonding between the coating and substrate. Therefore, in order for the aforementioned mechanism to arise, interface between the Al and Mg alloy is observed precisely as follows.

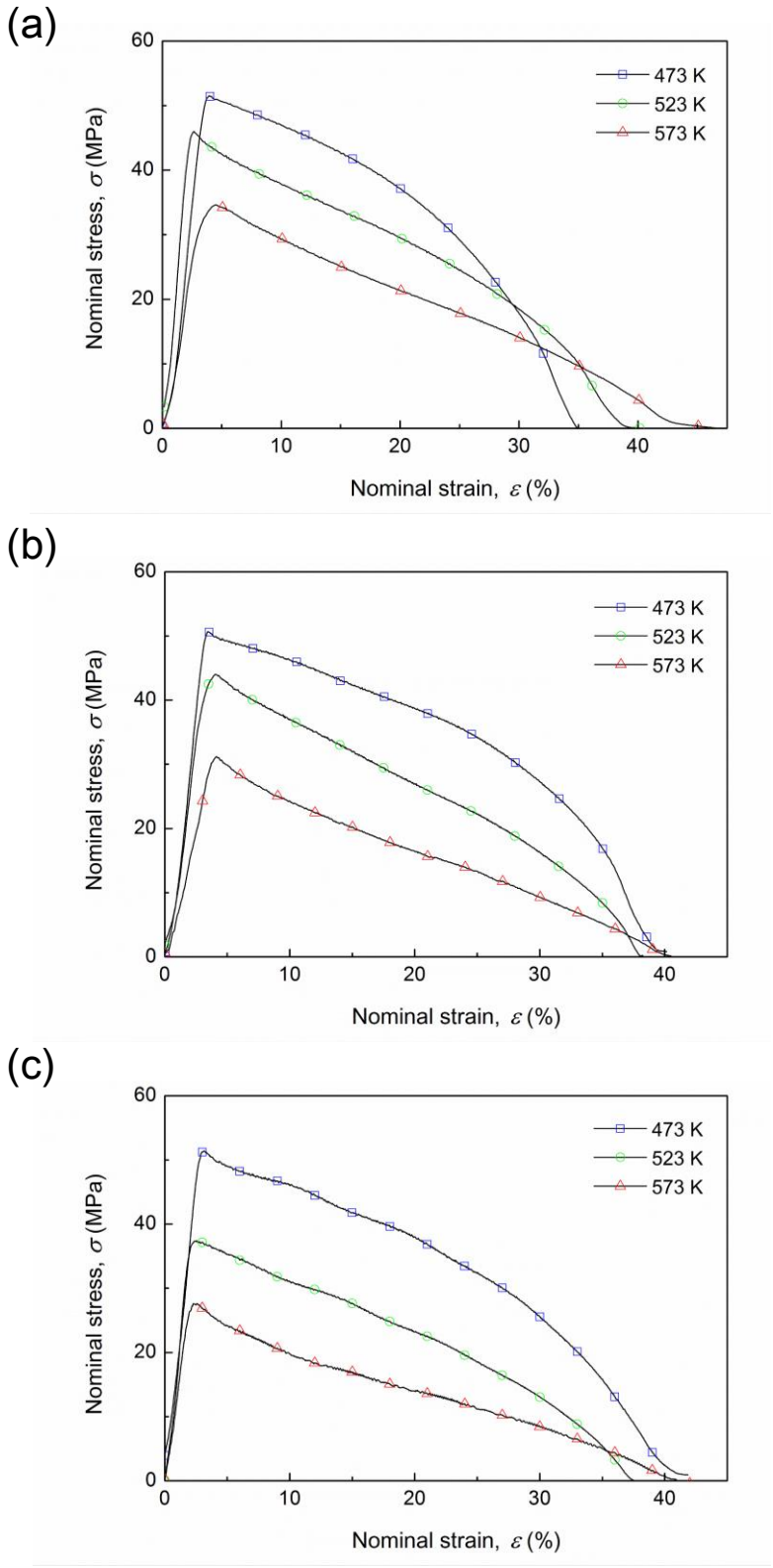

Fig. 7.12 Tensile behavior of the pure Al at various strain rates; (a) 2.0×10^{-3} s^{-1}, (b) 1.0×10^{-3} s^{-1} and (c) 6.0×10^{-4} s^{-1}.

Table 7.5 Summary of the total elongations at all conditions for the pure Al.

Al					
Temperature (K)	Strain rate (s^{-1})	Elongation (%)	Temperature (K)	Strain rate (s^{-1})	Elongation (%)
573	2.0×10^{-3}	47	498	2.0×10^{-3}	34
	1.5×10^{-3}	34		1.5×10^{-3}	35
	1.0×10^{-3}	40		1.0×10^{-3}	38
	6.0×10^{-4}	45		6.0×10^{-4}	45
	4.0×10^{-4}	38		2.0×10^{-4}	37
548	6.0×10^{-3}	42	473	2.0×10^{-3}	35
	2.0×10^{-3}	40		1.5×10^{-3}	36
	1.5×10^{-3}	42		1.0×10^{-3}	40
	1.0×10^{-3}	40		6.0×10^{-4}	42
	2.0×10^{-4}	45		2.0×10^{-4}	46
523	2.0×10^{-3}	41			
	1.5×10^{-3}	43			
	1.0×10^{-3}	38			
	6.0×10^{-4}	38			
	2.0×10^{-4}	43			

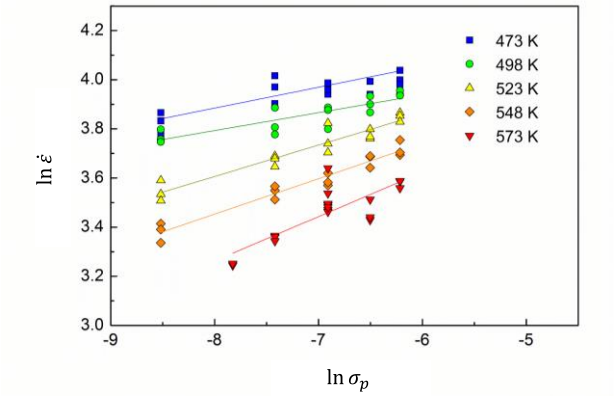

Table 7.6 Summary of *m*-value for the pure Al.

Temperature (K)	*m*-value
473	0.09
498	0.07
523	0.13
548	0.14
573	0.18

Fig. 7.13 Double logarithmic plots of true stress versus strain rate for the pure Al.

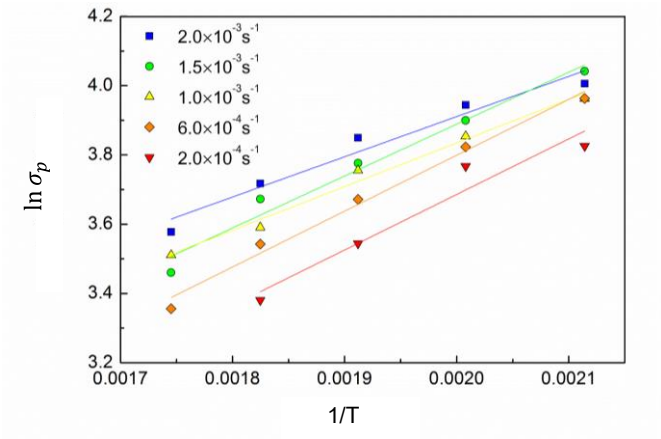

Table 7.7 Summary of Q for the pure Al.

Strain rate (s^{-1})	Activation energy (kJ/mol)
2.0×10^{-3}	88
1.5×10^{-3}	114
1.0×10^{-3}	96
6.0×10^{-4}	123
2.0×10^{-4}	122

Fig. 7.14 Plots of natural logarithm of true stress versus reciprocal of temperatures for the pure Al.

7.6 Interface structure

As shown in the previous section 7.5.2.2, it has been demonstrated that the pure Al does not exhibit the large elongation when it is tensile-tested alone, and the reason of the large elongation of the pure Al coating in the composite sheet has been considered as the load transfer and necking suppression by the superplastic Mg alloy substrate. In this section, in order to verify the mechanism, the Mg/Al interface is focused.

As shown in Chapter 2, an intermetallic compound layer of Al_3Mg_2 was formed at the interface between the Al coating layer and the Mg alloy substrate during the hot extrusion. Due to the hot forging process, the thickness of the intermetallic compound layer was reduced from 3.8 to 2.0 μm and by the forging process, the intermetallic compound was broken and some cracks were formed in the longitudinal direction, as indicated by arrows in Fig. 7.15 (a). Figure 7.16 illustrates optical images of intermetallic compound after the tensile tests under variety of conditions. After the tensile tests at room temperature, the intermetallic compound exhibits cracks in transverse direction and a larger number of cracks were observed than in the as-forged sheet. While the intermetallic compound in the specimen tensile-tested at 473 K, a much less number of cracks were observed and moreover, the intermetallic compound in the specimen tensile-tested at 573 K, no transverse cracks were observed. Furthermore, it should be noted that no debondings were observed at both interfaces between the Al coating and the intermetallic compound and between the Mg alloy substrate and the intermetallic compound in all

conditions. Namely, the sufficient bonding interface has been kept in the Al-coated Mg alloy sheet even after the maximum tensile elongation of 550 %. Consequently, it can be concluded that the large elongation of the pure Al, coated on the Mg alloy, can be explained by the load transfer.

However, there is still a concern for the behavior of intermetallic compound during the tensile tests. In the whole tensile specimen tested at 573 K and at 1.0×10^{-3} s^{-1} exhibited a large elongation of 550 %, almost no cracks were observed in the intermetallic compound despite the brittle characteristics, originating from their giant unit cell. This phenomenon can be understood in two ways; self-recovery of cracks by growing and plastic deformation. However, even though the present Al_3Mg_2 intermetallic compound layer exhibited a good formability in the bending tests at elevated temperatures as shown in Chapter 2, there are too much differences in the degree of deformation between the bending tests and the superplasticity. Therefore, in order to resolve this concern, the further observation of the intermetallic compound was carried out.

In order to follow the deformation behavior of the intermetallic compound layer during the tensile test, Al-coated Mg alloy sheets were water-quenched at several strains and the intermetallic compounds at each strain were observed by FE-SEM. The tensile test at 573 K and at 1.0×10^{-3} s^{-1} was selected as a representative condition.

Figure 7.17 illustrates the intermetallic compounds during the tensile test at 573 K and at 1.0×10^{-3} s^{-1} at a strain of (a) and (b) 12 %, (c) and (d) 100 %, (e) and (f) 200 % and (g) and (h) 480 %. Figures 7.17 (a), (c), (e) and (g) depict the sound part, while (b), (d), (f) and (h) depict the cracks. At the beginning of the tensile test, some cracks can be observed, however, as the test proceeds, the number of cracks decreases. Specifically, at a strain of 200 % (Figs. 7.17 (e) and (f)), some transverse cracks were observed, however, at a strain of 480 % (Figs. 7.17 (g) and (h)), no transverse cracks were observed and instead of that, only a small number of longitudinal cracks were observed, which can be considered as remains of the transverse cracks. Therefore, interestingly, it can be said that the broken intermetallic layer appeared to be repaired during the tensile test.

In the present section 7.6, it has been demonstrated that the good bonding between the Al coating and Mg alloy substrate has been retained during the tensile tests. Therefore, it can be said that the large elongation of the pure Al coating in the sheet is originated in the necking suppression by the superplastic Mg alloy substrate. However, the actual evolution and behavior of the pure Al as the coating layer during the tensile test is still unclear. Thus, the microscopic and crystallographic observations are performed in the following sections.

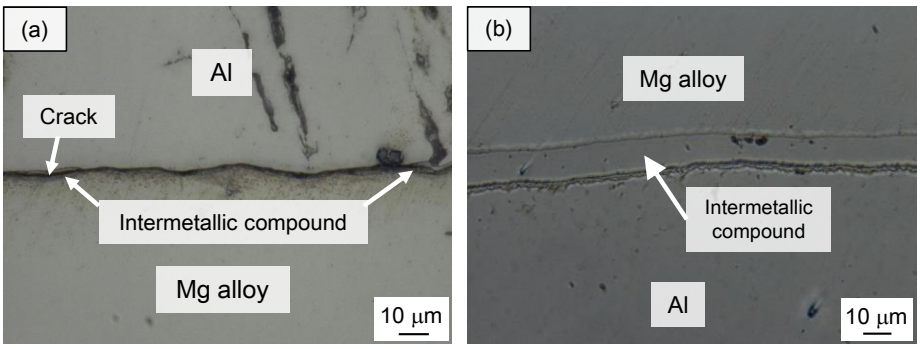

Fig. 7.15 Cross sections of the interface between Al coating layer and the Mg alloy substrate; (a) before and (b) after the tensile test at 573 K and at 1.0×10^{-3} s^{-1}.

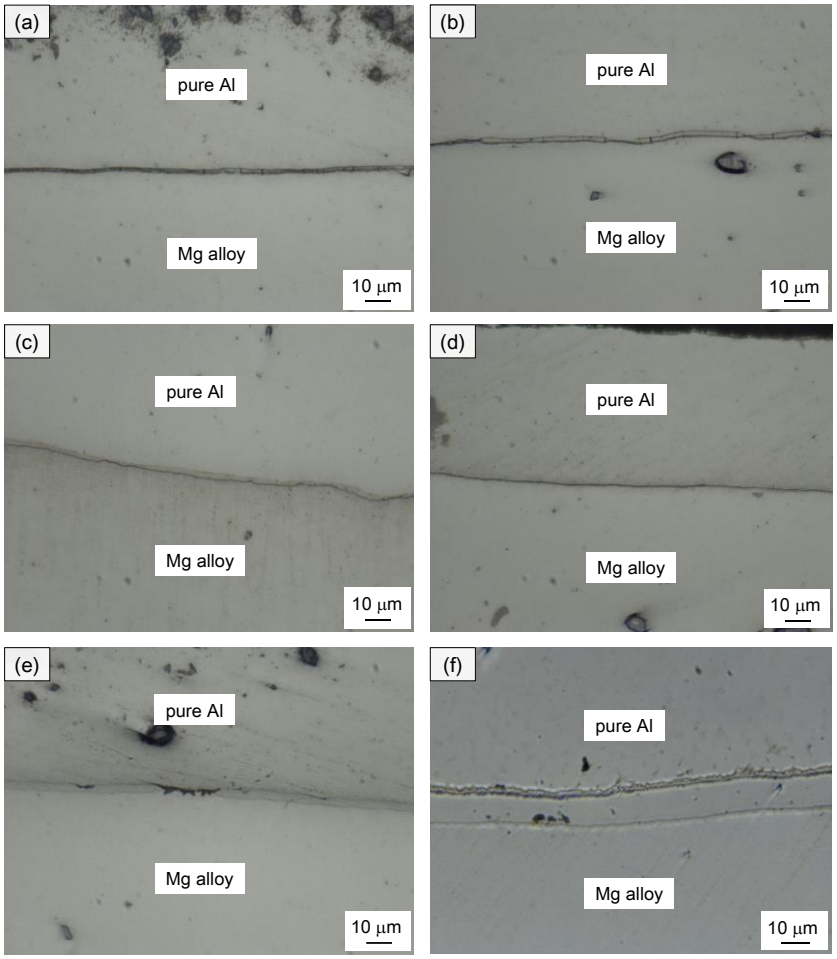

Fig. 7.16 Intermetallic compounds after the tensile tests under variety of conditions; (a) at room temperature at 1.0×10^{-2} s^{-1}, (b) at room temperature at 1.0×10^{-3} s^{-1}, (c) at 473 K at 1.0×10^{-2} s^{-1}, (d) at 473 K at 1.0×10^{-3} s^{-1}, (e) at 573 K at 1.0×10^{-2} s^{-1} and (f) at 573 K at 1.0×10^{-3} s^{-1}.

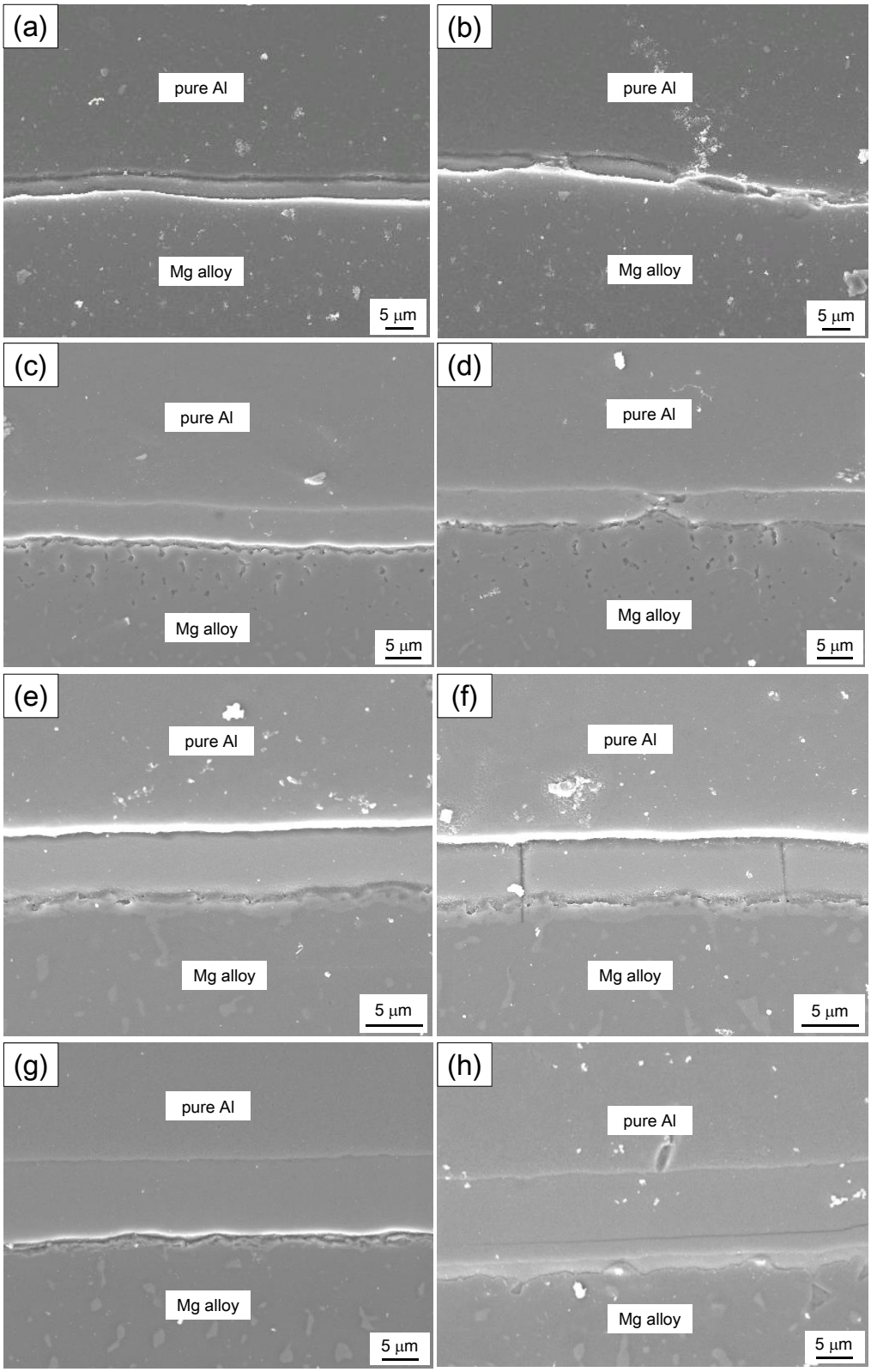

Fig. 7.17 Intermetallic compounds during the tensile test at 573 K and at 1.0×10^{-3} s^{-1} at a strain of (a) and (b) 12 %, (c) and (d) 100 %, (e) and (f) 200 % and (g) and (h) 480 %.

7.7 Deformation mechanism of pure Al as coating layer

7.7.1 Microstructure and crystallographic observation after tensile tests

In order to investigate the tensile deformation behavior of pure Al as the coating material, the microstructure and crystallographic orientations were investigated by EBSD analysis. Figure 7.18 illustrates the microstructures and crystallographic orientations of the Al coating layer. ND and RD indicate the extrusion and forging directions in the process for the fabrication of the tensile specimens, respectively, and the tensile direction is indicated by TD in the pole figures. For comparison, the Al in the as-forged Al-coated Mg alloy sheet is also presented in Fig. 7.18 (a), and Figs. 7.18 (b), (c) and (d) illustrate the microstructures and crystallographic orientations of the Al in the sheet tensile-tested at 1.0×10^{-3} s^{-1} and at room temperature, 473 K and 573 K, respectively. These inverse pole figures (IPFs) illustrate the crystal orientations of each pixel, however, only the crystallographic orientation, which face to ND to the sheet can be read and there are no information about the three dimensional orientation. Therefore, Figs. 7.18 (e), (f), (g) and (h) are illustrated, which are the IPFs obtained from the same region but each pixel illustrates the orientation observed from TD. As a consequence, the three dimensional observation for the crystal orientations of the sheets can be attained with a pair of those pictures.

The obtained total elongations of the specimens shown in Fig. 7.18 (c) and (f), (e) and (g), and (d) and (h) were 27, 240 and 550 %. The upper and lower sides of the figures correspond to the interface and surface sides, respectively. These images were taken from the range as much as possible in the coating area, therefore, the differences of the image heights are due to the differences in the coating thickness.

Firstly, the microstructure morphologies are focused here. As was shown in the section 5.3.2 in Chapter 5, the as-forged Al in Fig. 7.18 (a) shows the equiaxed grains in whole through thickness, while from Figs. 7.18 (b) and (c), it can be seen that the grains near the interface are elongated while the ones near the surface are not elongated and remain to be equiaxed as the as-forged Al shown in Fig. 7.18 (a). Apparently, this grain elongation can be considered to be due to a restriction from the Mg alloy substrate. Because the restrictions are only imposed on the interface and not on the surface, therefore, the half microstructure could remained to be equiaxed. Furthermore, a careful observation of Figs. 7.18 (b) and (c) reveals that the elongated grains consists of the aggregation of smaller equiaxed grains segmented by the low-angle boundaries. It has been known that pure Al can easily trigger the recovery even at a room temperature because the melting

temperature of pure Al is quite low of 933 K, namely, room temperature (298 K) is $0.32T_m$ for pure Al. Therefore, the equiaxed grains in Figs. 7.18 (b) and (c) can be considered to be results of recovery process.

In Fig. 7.18 (d), the significant grain coarsening can be observed. It should be noted that Fig. 7.18 (d) shows only small number of grains, however, most of the grains in the sheet exhibited the same tendencies in orientation and shape. Furthermore, in Fig. 7.18 (d), it is noteworthy that the grains are equiaxed even after the large elongation of 550 %. Generally, the reasons for the development of the equiaxed grains, being supposed to be elongated, are recrystallization or grain boundary sliding (GBS). Since it is not appropriate to discuss about microstructure evolution with only one picture, this topic will be discussed later using other data.

Secondly, with respect to the crystal orientations, originally, the as-forged Al (Fig. 7.18 (a)) clearly shows that the {011} planes are face to both ND and TD and {111} planes, which are the major slip planes for f.c.c. materials, are aligned to parallel to the forging die. This can be understood as below; because of the high forging reduction ratio of 85 %, the pure Al was totally deformed with the slip of the {111} planes. Additionally, weak recrystallization texture of {100} <001> can be seen in the pole figures in both ND and TD. Therefore, it can be seen that the pure Al has undergone the recrystallization, which results in the equiaxed grains.

While, after the tensile deformation, textures has significantly changed. The Al in the sheet tensile-tested at room temperature (Fig. 7.18 (b)) exhibited a weak compression texture and slightly rotated tensile fiber texture of [111]. At elevated temperatures (Figs.7.18 (c) and (d)), the brass-type texture were observed, however, it is known that pure Al generally does not show the brass-type texture because of its high stacking fault energy [7.42]. Therefore, as one of the substitutional possibilities to lead this texture, the constraint effect by Mg alloy substrate was taken into account. Figure 7.19 depicts the various constraints models of the so-called “relaxed Taylor model” by indicating the deformed shapes of an originally-cubic grain with different shears, and Fig. 7.20 illustrates some textures calculated with the model [7.43]. Note that RD indicated in Fig. 7. 20 is specified as R in Fig. 7. 19 and is different from the direction indicated in Fig. 7. 18. As the constraints, the three principle shears were considered as shown in Fig. 7.19. From the calculated textures shown in Fig. 7.20, it can be said that the texture obtained from the Al part in the sheet tensile-tested at elevated temperatures (Figs.7.18 (c) and (d)) are similar to the calculated one with the constraints BS or BSC, which is shear in multiple directions (Figs.7.20 (c) and (d)). Thus, the texture shown in Figs.7.18 (c) and (d) can be considered as the compression textures with the constraints by the Mg alloy substrate.

The above discussion seems to be reasonable, however, actually there is a conflict when considering the microstructure and crystallographic observation results together. In Figs. 7.18 (b) and (c), the microstructures show the constraint effect only about a half part close to the Mg alloy, however, the Al in the whole range of the thickness exhibits the constraint type textures, as can be seen as a green-colored region. In order to explain this phenomenon, further investigations are definitely necessary. Furthermore, the reason for the development of the equiaxed grains after the large elongation is also still not clarified yet. Therefore, in the next section, the microstructure and crystallographic evolutions of the pure Al during the tensile test are investigated in detail.

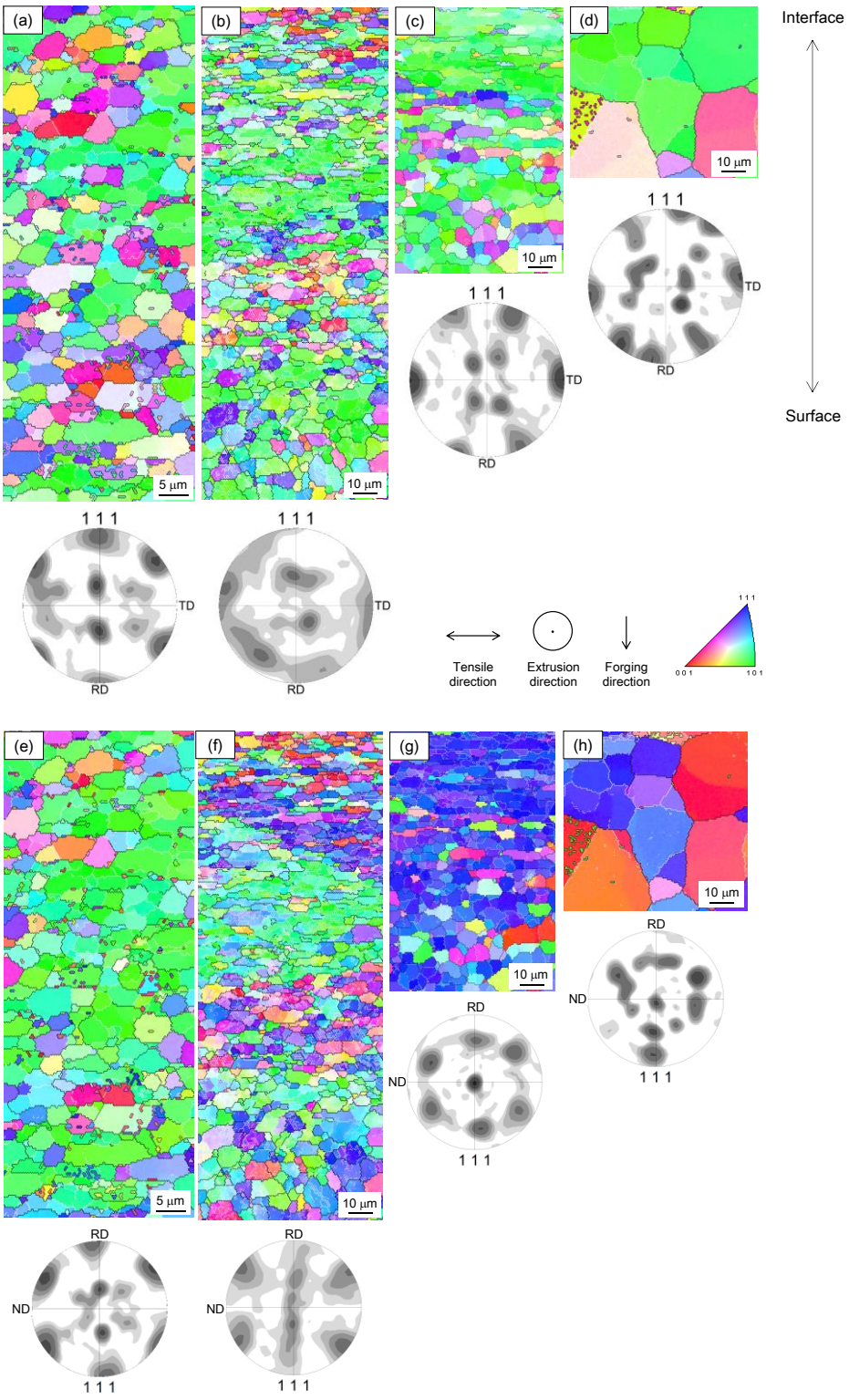

Fig. 7.18 EBSD analysis results of Al coating in the sheet; (a) and (e) as-forged; from (b) to (h) are elongated at 1.0×10^{-3} s^{-1} and at room temperature ((b) and (f)), 473 K ((c) and (g)) and 573 K ((d) and (h)), respectively. ND and RD indicate the extrusion and forging directions in the process for the fabrication of the tensile specimens, respectively, and the tensile direction is indicated by TD in the pole figures.

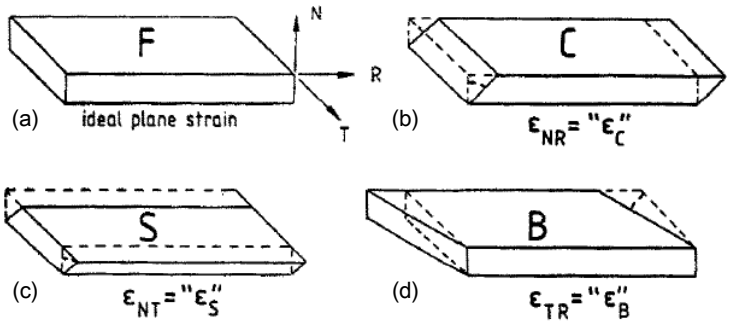

Fig. 7.19 Deformed shapes of an originally-cubic grain (a) under full constraints, and with relaxed constraints conditions with free shears of; (b) $\varepsilon_{\mathrm{NR}}$, (c) $\varepsilon_{\mathrm{NT}}$ and (d) $\varepsilon_{\mathrm{TR}}$ [7.43].

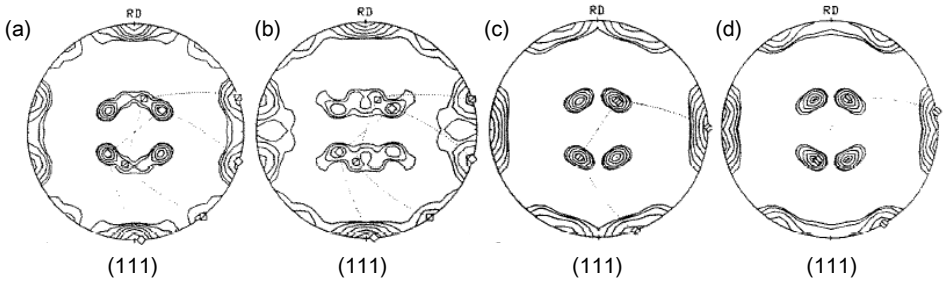

Fig. 7.20 (111) pole figures of calculated f.c.c. rolling textures with the constraints shown in Fig. 7.20; (a) constraint B, (b) constraint BC, (c) constraint BS and (d) constraint BSC [7.43]. RD is specified as R in Fig. 7. 19 and is different from the direction indicated in Fig. 7. 18.

7.7.2 Microstructure and crystallographic evolution during tensile test

The Al-coated Mg alloy sheet was water-quenched at several strains, as in the same manner in the previous section 7.6, and the microstructure and crystallographic orientation were examined by EBSD analysis. The tensile test at 573 K and at 1.0×10^{-3} s^{-1} was selected as a representative condition to be investigated.

Figure 7.21 illustrates the microstructural and crystallographic changes during the tensile test. As in the case of Fig. 7.20, the results observed from both ND and TD are presented to achieve the quasi-three dimensional observation. ND and RD indicate the extrusion and forging directions in the process for the fabrication of the tensile specimens, respectively, and the tensile direction is indicated by TD in the pole figures. The black and white boundaries in the images represent high (more than 15 ^{o}) and low (2 ^{o} to 15 ^{o})

angle grain boundaries. This time, for the detailed investigation, the IPFs after the 10 minutes of heating prior to the tensile test are also illustrated as Figs. 7.21 (b) and (i).

Firstly, it is certain that after the 10 minutes of heating most of the grains exhibit the recrystallization texture. However, after starting the actual tensile test, textures totally changed already after 12 % of elongation. At 12 % of elongation (Figs. 7.21 (c) and (j)), the Al layer exhibits the fiber texture of [111], which is known as the texture of f.c.c. materials under the tensile force. However, after 50 % of elongation (Figs. 7.21 (d) and (k)), the aforementioned constraint texture, shown in the previous section 7.7.1, can be seen and from then on, this constraint texture remained until fracture.

This texture change can be understood as hereinafter. Generally, the crystals in f.c.c. materials rotate following to the arrow indicated in Fig. 7.22 (a) under the tensile force and the arrow indicated in Fig. 7.22 (b) under the compression force [7.44]. In the present study, the starting point is not as indicated in the figure, but the (0 1 0) or (1 0 0) point because of the recrystallization texture. Firstly, the pure Al follows the arrow in Fig. 7.22 (a) due to the tensile force, however, after a certain amount of strain, the effect from the Mg alloy has grown larger, and then the pure Al starts following the arrow in Fig. 7.22 (b) and textures exhibited the compression textures. In other words, this texture change indicates the change of the type of the force, loaded on the Al, at some point during the tensile test.

This theory well-illustrates the texture change, shown in Fig. 7.21, however, it is still unclear at which strain the texture has changed. Here, the strain, which shows the maximum possible elongation of individual pure Al of 40 %, should be an important point as a threshold. The considerable reason is as follows. As confirmed with the microstructure of a specimen tensile-tested at room temperature (Fig. 7.18 (b) and (f)), the Mg alloy substrate influences only on about the half of the thickness in Al coating layer, and therefore, the other half should deform by itself. It means that the pure Al, positioned in the surface side, should activate the slip system and achieve the elongation with following the rotation path for the tensile force (Fig. 7.22 (a)). However, if the whole specimen exceeds the maximum elongation innate to the pure Al, the Al layer, which is excluded from the support of Mg alloy substrate, should be fractured. In the actual tensile test, there is no such macroscopic fracture, therefore, the threshold strain should be smaller than the maximum elongation innate to the pure Al and after the threshold strain, the tensile force imposed to the pure Al layer should change to the compression force, which is much harder to cause the fracture rather than tensile force. This load-type change can also be a reason for the large elongation of the pure Al over its innate maximum elongation other than the aforementioned load transfer, owing to the strong bonding at the

interface.

In the above discussion, the large elongation of the pure Al as a coating material has explained. Note that the discussion is done under the assumption that the Al deformed with the crystallographic slip, however, when considering the reason of observed equiaxed grains, there are two possibilities of the deformation mechanism; crystallographic slip and GBS. In order to elucidate this microscopic deformation mechanism, the observed microstructure change during the tensile test is examined hereinafter.

Before mentioning the equiaxed grains, first of all, the general microstructure evolution is described in accord with the observation results. In Figs. 7.21 (a) and (b), there is no remarkable change of the grains in shape and orientation. However, after strain of 50 % and mainly in the surface side, there are some grains, not showing the constraint texture. It is worthy of attention that those grains are surrounded by only the high-angle boundaries. After entering the constraint texture state, the grains can be classified into three main groups by the boundary types surrounding it. Taking into account that the high-angle boundaries can move faster than the low-angle boundaries, the microstructure evolutions during the tensile test for each grain can be explained by the following theories;

1. As for the grains with high-angle boundaries, the boundaries move and the grains eat their neighbor grains and consequently coarsen.

2. As for the grains with low-angle boundaries, the boundaries hardly move and therefore, grains simply form the recovered microstructure.

3. As for the grains with partially high-angle boundaries, when the neighbors have the similar crystallographic orientations, the grains form the low-angle boundary at the interface, and consequently form the recovered microstructure.

Here the recovered microstructure can be observed in Figs. 7. 21 (d), (e) and (f) as the grains with the gradations, originating from the polygonization.

From the aforementioned three evolutions, the grain coarsening during the tensile test can be explained by the motion of the high-angle boundaries (theory 1) or the coalescence of the sub-grains due to the grain rotation as shown in Fig. 7.23 (theory 2) [7.45]. The coalescence can be explained as the process of dislocation motion from the dissipating sub-grains to the other sub-grains. Therefore, for this process, the dislocation climb along the dissipating sub-grain boundaries and grain rotation involving the atomic motion are necessary. That is, the diffusion process is definitely required. Figure 7. 24

illustrate the three-dimensional deformation mechanism diagram of the pure Al [7.46]. According to the figure, the present pure Al with the as-forged grain size deforms with the mechanism of Coble creep model. Therefore, it has been elucidated that this pure Al have potential for the dislocation climb and atomic diffusion for the coalescence by the mechanism of Coble creep.

Up to here, the microstructure evolution has been explained and from here, the equiaxed grains are explained. As mentioned above, the possible mechanism of the equiaxed grains are recrystallization or GBS. The ideas to motivate each mechanism are given below.

If the reason for the development of the equiaxed grains is GBS, the major deformation mechanism should be the combination of GBS and crystallographic slip. In this case, the aforementioned Coble creep mechanism can account for the accommodation process of GBS. This Coble creep contribution for the deformation agrees with the deformation mechanism diagram, which indicates the deformation should be governed by the Coble creep. However, there are some drawbacks to support this GBS theory. Firstly, GBS is characterized by the texture randomization, however, it is not observed in the present study. By considering the strong constraint from the Mg alloy substrate, it should be hard to arise GBS with the grain rotation. Secondly, a large extent of the grain size coarsening has occurred during the tensile test, therefore it is likely to cross over the Coble creep deformation region in the deformation mechanism diagram.

The dynamic or static recrystallization is also a possible reason for the development of the equiaxed grains. As for the dynamic recrystallization (DRX), even though there are some reports of DRX of high purity Al [7.47], there are no reports for the discontinuous dynamic recrystallization (DDRX) of the pure Al with 99.99 % (4N) of the present sample purity. While it is known the 4N-Al to arise the continuous DRX (CDRX), which is basically classified as the same process as the dynamic recovery [7.48]. Therefore, the 4N-Al in the present study is more likely to have undergone the CDRX rather than DDRX. The difference between the CDRX and DDRX is illustrated in Fig. 7.25 [7.49]. Basically, in DDRX process, the recrystallization nuclei form preferentially at some highly deformed region, while in CDRX process, the grain nucleation and coarsening occur homogeneously and after this process, the microstructures are quite similar to the one after the DDRX. In this CDRX process, it is known that when a material undergoes the severe plastic deformation, all the grains have potential to be recrystallized, and therefore, because of the high temperature, all the grain boundaries shift homogeneously and the equiaxed grains are created. This can explain the microstructure of the present study well, and therefore, this process can be considered as a dominant mechanism of the equiaxed

grain formation. Moreover, it is generally known that the static recrystallization can occur even in such a very short period after the deformation and before water-quenching. Therefore, static recrystallization is also likely to arise and can be a reason for the the development of equiaxed grains.

However, there are only some grains showing the recrystallization texture after the elongation of 550 %, and the equiaxed grains are not only the ones showing the recrystallization texture but also the others. Therefore, the reason for the development of the equiaxed grains cannot be explained only by the recrystallization. To sum up, the reason for the development of the equiaxed grains is the most likely to be a result of CDRX. However, it cannot be stated here explicitly, because the static recrystallization can occur as well and there is a conflict with the obtained texture.

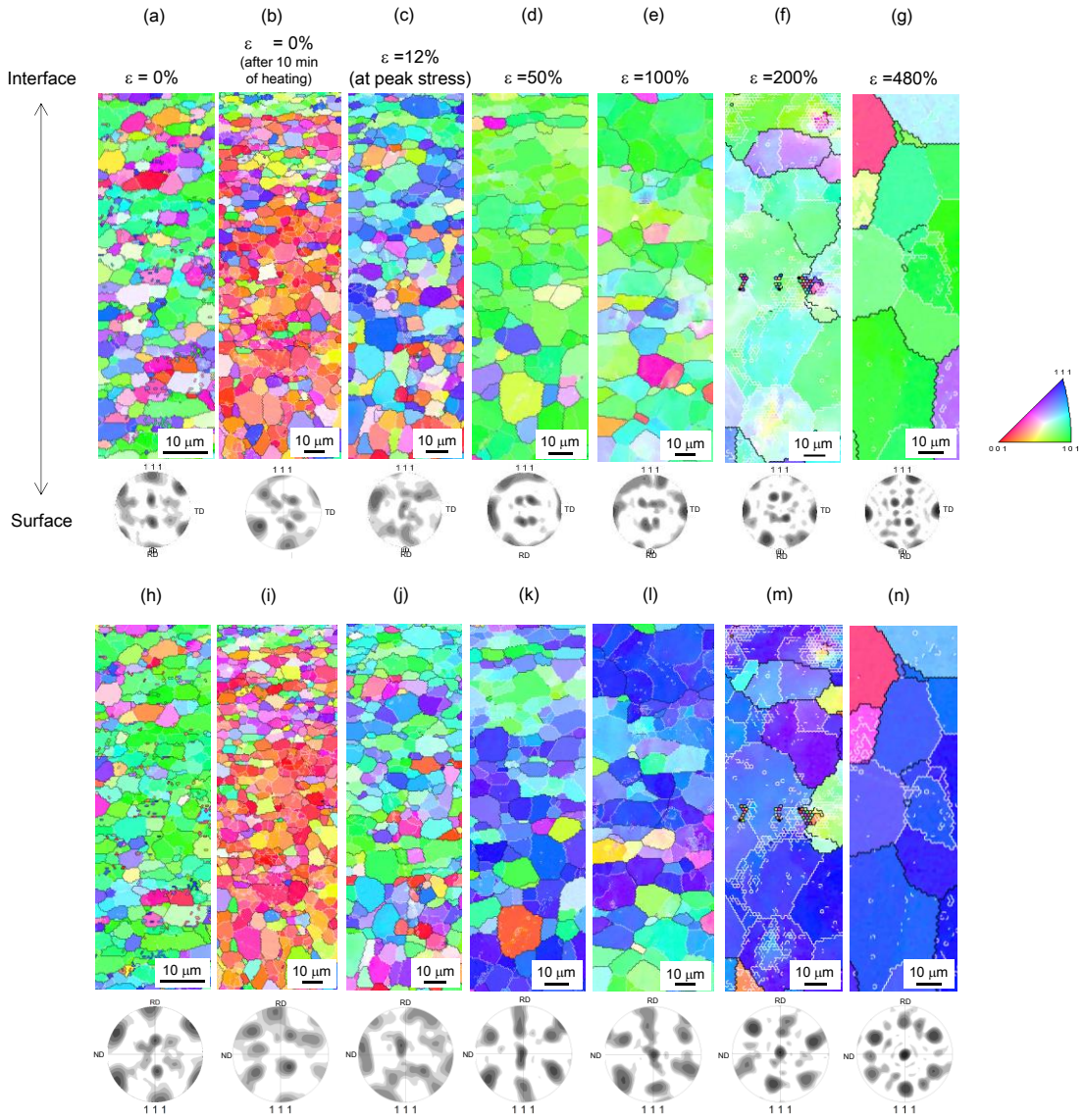

Fig. 7.21 Crystal orientation change during the tensile test at a temperature of 573 K and at a strain rate of 1.0×10^{-3} s^{-1}. Forging direction is vertical and the extrusion direction is normal to this paper. The black and white boundary lines represent high (more than 15 ^{o}) and low (2 ^{o} to 15 ^{o}) angle grain boundaries. ND and RD indicate the extrusion and forging directions in the process for the fabrication of the tensile specimens, respectively, and the tensile direction is indicated by TD in the pole figures. From (a) to (g) show the results observed from ND and from (h) to (n) show the ones observed from TD.

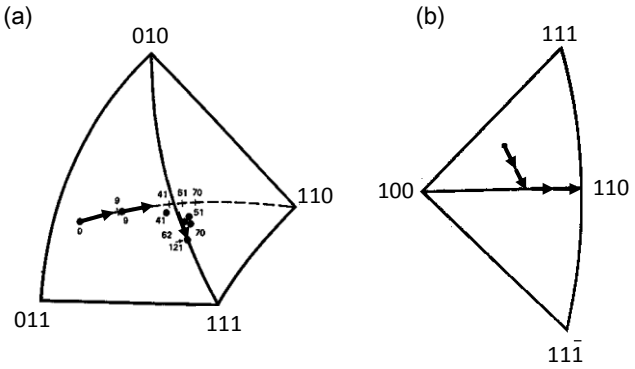

Fig. 7.22 Crystal rotations of f.c.c. materials under (a) tensile force and (b) compression force [7.44].

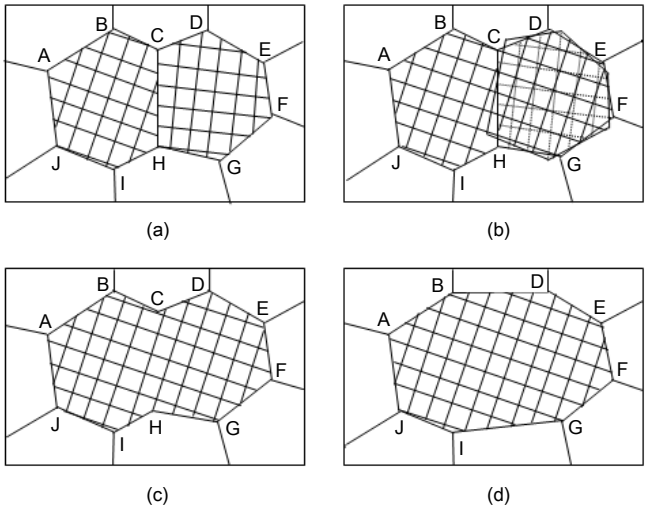

Fig. 7.23 Coalescence of two subgrains by rotation of one of them. (a) The original subgrain structure before coalescence; (b) one subgrain is undergoing a rotation; (c) the subgrain structure just after coalescence; (d) the final subgrain structure after some subboundary migration [7.45].

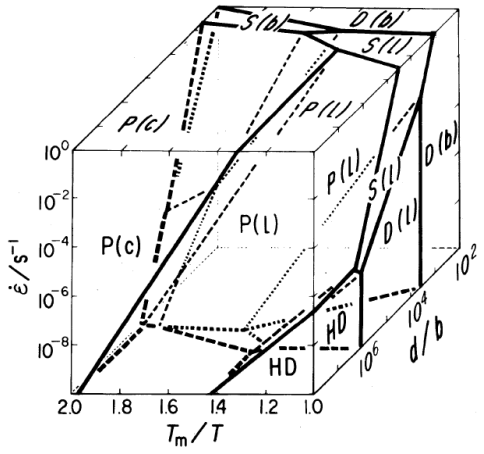

P	Power-law creep
S	Superplastic flow
D	Diffusion creep
HD	Harper-Dorn creep
l	lattice diffusion
b	grain-boundary diffusion
c	dislocation-core diffusion

Fig. 7.24 Three-dimensional presentation of the deformation mechanism diagram of pure Al. Thick lines are on the surface and medium lines are in the interior of the hexahedron [7.46].

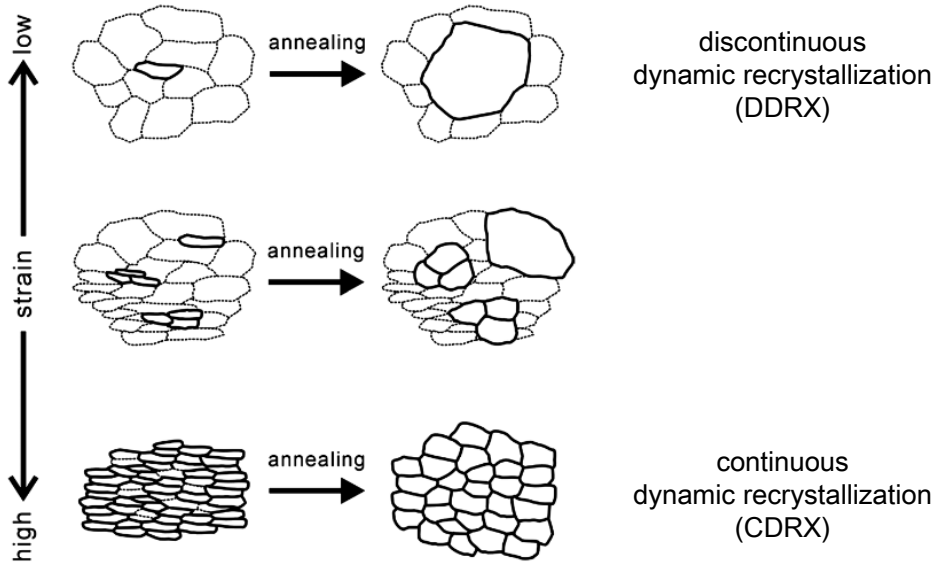

Fig. 7.25 Schematic illustrations showing the difference of DDRX and CDRX [7.49].

7.8 Summary

In the present chapter, the deformation behavior of the Al-coated Mg alloy sheet has been investigated in detail. By introducing the strain rate sensitivity index, it was found that the obtained large elongation of the sheet can be classified as superplasticity.

By investigating the individual tensile behaviors of each Mg alloy and pure Al, it was found that the Mg alloy showed superplasticity, however, the ductility of the pure Al was significantly poor when it is tensile-tested alone.

The microstructure and crystallographic investigations of the pure Al coated on the Mg alloy have revealed the reason for the large elongation of the pure Al on the Mg alloy substrate. It can be considered that the strong bonding at the Mg/Al interface suppressed the necking initiation of the pure Al layer. The intermetallic compound was observed in detail and the strong bonding at the interface was confirmed. Moreover, the restriction from the Mg alloy causes the major force to deform the pure Al from the tensile force to the compression force. This force change can also contribute the abnormal large elongation. Lastly, the reason for the development of the equiaxed grains observed after the large elongation is discussed. It has been found that the most likely reason should be the continuous dynamic recrystallization. However, since there is still a conflict with the texture results, therefore the explicit determination of the formation mechanism of the equiaxed grains has been avoided in the present study.

References

[7.1] W.A. Backofen, I.R. Turner, D.H. Avery, Superplasticity in an Al-Zn alloy. *Trans. Am. Soc. Metals* **57** (1964) 980-990.

[7.2] N. Chandra, Constitutive behavior of superplastic materials. *Inter. J. Non-Linear Mech.* **37** (2002) 461-484.

[7.3] M. Kawasaki, T.G. Langdon, Principles of superplasticity in ultrafine-grained materials. *J. Mater. Sci.* **42** (2007) 1782-1796.

[7.4] K. Kitazono, Past and future of superplasticity. *J. Jpn. Inst. Light Met.* **63** (2013) 160-164 (*in Japanese*).

[7.5] J.W. Edington, K.N. Melton, C.P. Cutler, Superplasticity. *Prog. Mater. Sci.* **21** (1976) 61-158.

[7.6] K. Higashi, Advances in superplasticity and in superplastic materials (I) - Phenomenological expression of superplasticity. *Journal of the Society of Powder Technology* **25** (1988) 528-536. (*in Japanese*)

[7.7] M.F. Ashby, R.A. Verrall, Diffusion-accommodation flow and superplasticity. *Acta Met.* **21** (1973) 149-163.

[7.8] R.C. Gifkins, Grain-boundary participation in high-temperature deformation: An historical review. *Mater. Charact.* **32** (1994) 59-77.

[7.9] M. Otsuka, R. Horiuchi, Superplasticity in aluminum alloys. *J. Jpn. Inst. Light Met.* **27** (1977) 85-101. (*in Japanese*)

[7.10] C.W. Humphries, N. Ridley, Cavitation in alloy steels during superplastic deformation. *J. Mater. Sci.* **9** (1974) 1429-1435.

[7.11] D.W. Livesey, N. Ridley, Cavitation and cavity growth during superplastic flow in microduplex Cu-Zn-Ni alloys. *Metall. Mater. Trans. A* **13** (1982) 1619-1626.

[7.12] J. Xinggang, C. Jianzhong, M. Longxiang, Fractal dimension of fracture surface and superplasticity of 7475 Al alloy. *J. Mater. Sci. Lett.* **12** (1993) 1616-1618.

[7.13] D.A. Miller, T.G. Langdon, Evidence for cavitation in superplastic Zn-22 pct Ai of very high purity. *Metall. Mater. Trans. A* **9** (1978) 1688-1690.

[7.14] S.A. Shei, T.G. Langdon, The fracture characteristics of a superplastic single phase copper alloy. *J. Mater. Sci.* **13** (1978) 1084-1092.

[7.15] Y.H. Wei, Q.D. Wang, Y.P. Zhu, H.T. Zhou, W.J. Ding, Y. Chino, Superplasticity and grain boundary sliding in rolled AZ91 magnesium alloy at high strain rates. *Mater. Sci. Eng. A* **360** (2003) 107-115.

[7.16] M.G. Zelin, On micro-superplasticity. *Acta Mater.* **45** (1997) 3533-3542.

[7.17] S. Lee, C.T. Chinang, C.L. Chu, C.C. Hsu, Mechanical properties and fracture

mechanisms of aluminum matrix composites reinforced by $Al_9(Co, Ni)_2$ intermetallics. *Trans. Nonferrous Met. Soc. China* **20** (2010) s576-s579.

[7.18] Y. Takayama, T. Tozawa, H. Kato, Superplasticity and thickness of liquid phase in the vicinity of solidus temperature in a 7475 aluminum alloy. *Acta Mater.* **47** (1999) 1263-1270.

[7.19] W.D. Cao, X.P. Lu, H. Conrad, Whisker formation and the mechanism of superplastic deformation. *Acta Mater.* **44** (1996) 697-706.

[7.20] G. Dirras, J. Gubicza, D. Tingaud, S. Billard, Microstructure of Al-Al_2O_3 nanocomposite formed by *in situ* phase transformation during Al nanopowder consolidation. *Mater. Chem. Phys.* **129** (2011) 846-852.

[7.21] C.L. Chen, M.J. Tan, Cavity growth and filament formation of superplastically deformed Al 7475 Alloy. *Mater. Sci. Eng. A* **298** (2001) 235-244.

[7.22] J.J. Blandin, B. Hong, A. Varloteaux, M. Suery, G. L'esperance, Effect of the nature of grain boundary regions on cavitation of a superplastically deformed aluminum alloy. *Acta Mater.* **44** (1996) 2317-2326.

[7.23] Y. Takayama, T. Tozawa, H. Kato, Superplasticity and thickness of liquid phase in the vicinity of solidus temperature in a 7475 aluminum alloy. *Acta Mater.* **47** (1999) 1263-1270.

[7.24] H.R. Abedi, A. Zarei-Hanzaki, S. Khoddam, Effect of γ precipitates on the cavitation behavior of wrought AZ31 magnesium alloy. *Mater. Design* **32** (2011) 2181-2190.

[7.25] M. Mabuchi, H. Iwasaki, K. Higashi, An investigation of shear deformation in a semi-solid state of a high strain rate superplastic Si3N4p/Al-Mg-Si composite. *Acta Mater.* **46** (1998) 5335-5343.

[7.26] W.J.D. Shaw, Microsuperplastic behavior. *Mater. Lett.* **4** (1985) 1-4.

[7.27] S.W. Lee, Y.L. Chen, H.Y. Wang, C.F. Yang, J.W. Yeh, On mechanical properties and superplasticity of Mg-15Al-1Zn alloys processed by reciprocating extrusion. *Mater. Sci. Eng. A* **464** (2007) 76-84.

[7.28] D.L. Yin, K.F. Zhang, G.F. Wang, W.B. Han, Superplasticity and cavitation in AZ31 Mg alloy at elevated temperatures. *Mater. Lett.* **59** (2005) 1714-1718.

[7.29] K. Suzuki, Y. Ishida, M. Ichihara, Growth of whisker during "superplastic" straining of Zn-Al eutectoid. *J. Japan Inst. Metals* **38** (1974) 920-925. (*in Japanese*)

[7.30] R.C. Gifkins, Activation energies for superplastic materials. *Scripta Metall. Mater.* **10** (1976) 433-436.

[7.31] M.F. Ashby, H.J. Frost, Deformation-Mechanism Maps. Pergamon Press, Oxford, 1982.

[7.32] H.T. Zhou, Q.B. Li, Z.K. Zhao, Z.C. Liu, S.F. Wen, Q.D. Wang, Hot workability characteristics of magnesium alloy AZ80 – A study using processing map. *Mater. Sci. Eng. A* **527** (2010) 2022-2026.

[7.33] T.Y. Kwak, W.J. Kim, Hot compression behavior of the 1 wt% calcium containing Mg-8Al-0.5Zn (AZ80) alloy fabricated using electromagnetic casting technology. *Mater. Sci. Eng. A* **615** (2014) 222-230.

[7.34] W.J. Kim, Y.G. Lee, Enhanced superplasticity of 1 wt.%Ca-AZ80 Mg alloy with ultrafine grains. *Mater. Lett.* **64** (2010) 1759-1762.

[7.35] C. Jeong, T. Oya, J. Yanagimoto, Analysis of fracture behavior and stress-strain distribution of martensite/austenite multilayered metallic sheet. *J. Mater. Process. Technol.* **213** (2013) 614-620.

[7.36] J. Yanagimoto, T. Oya, S. Kawanishi, N. Tiesler, T. Koseki, Enhancement of bending formability of brittle sheet metal in multilayer metallic sheets. *CIRP Annals. Manuf. Technol.* **59** (2010) 287-290.

[7.37] M.H. Serror, Analytical study for deformability of laminated sheet metal. *J. Adv. Res.* **4** (2013) 83-92.

[7.38] C. Schoene, E. Scala, Multiple necking phenomena in metal composites. *Metall. Mater. Trans. B* **1** (1970) 3466-3469.

[7.39] M. Hojo, N. Iwasaki, F. Sekino, S. Ochiai, S. Sakai, K. Watanabe, Fracture behavior under fatigue loading at room temperature and its influence on critical current of Nb-Ti/Cu composite wire. *Cryogenics* **39** (1999) 627-636.

[7.40] S. Ochiai, K. Shimomura, Y. Murakami, Multiple necking of fibre in single tungsten fibre composites. *Met. Sci.* **9** (1975) 535-540.

[7.41] H.S. Liu, B. Zhang, G.P. Zhang, Delaying premature local necking of high-strength Cu: A potential way to enhance plasticity. *Scr. Mater.*, **64** (2011) 13-16.

[7.42] T. Takahashi, M. Hashimoto, T. Murakami, Influence of magnesium on the rolling texture of polycrystalline aluminum. *J. Jpn. Inst. Light Metals* **23** (1973) 425-429.

[7.43] J. Hirsch, K. Lucke, Mechanism of deformation and development of rolling textures in polycrystalline F.C.C. metals – II. Simulation and interpretation of experiments on the basis of Taylor-type theories. *Acta Metall.* **36** (1988) 2883-2904.

[7.44] G.I. Taylor, C.F. Elam, The plastic extension and fracture of aluminum crystals. *Proc. R. Soc. A-Math. Phys. Eng. Sci.* **108** (1925) 28-51.

[7.45] J. C. M. Li, Possibility of subgrain rotation during recrystallization. *J. Appl. Phys.*, **33** (1962) 2958-2965.

[7.46] H. Oikawa, Strain rate-temperature-grain size diagram of high-temperature deformation mechanism for aluminum. *J. Jpn. Inst. Light Metals* **30** (1980) 376-

383. (*in Japanese*)

[7.47] H. Yamagata, Dynamic recrystallization and dynamic recovery in pure aluminum at 583 K. *Acta Metall. Mater.* **43** (1995) 723-729.

[7.48] H. Yamagata, Y. Ohuchida, N. Saito, M. Otsuka, Effect of temperature on the continuous dynamic recrystallization of 99.99 % aluminum. *Mater. Trans.* **42** (2001) 2440-2445.

[7.49] N. Tsuji, Formation mechanisms of ultrafine grained structures in severe plastic deformation of metallic materials. *Tetsu-to-Hagané* **94** (2008) 582-589. (*in Japanese*)

Chapter 8

Conclusions

Mg alloys are the lightest metal materials among practically used alloys for structural applications and they also possess many other attractive properties such as good recyclability and high ability of vibration absorption and electromagnetic shielding. Owing to these superior properties, they have attracted a great deal of attention from a number of industries in a broad range of areas. Specifically, Mg alloys capture the attentions of automobile industries, doe to their ambition to achieve the weight reduction of vehicles in reaction to the global environmental problems. However, the practical applications of Mg alloys have been limited because of their extremely poor corrosion resistance. Although a large number of coating techniques have been proposed, the high reactivity of Mg alloys makes the coating process extremely difficult and therefore, promising coating techniques have been still anticipated for the further development and applications of Mg alloys.

In the preliminary study of the present author, a new coating technique by using hot extrusion was developed. The present study has dedicated to further development and characterization of the Al-coated Mg alloy. This study has demonstrated a possibility of wide and practical use of Mg alloys by the multi-disciplinary approach with both experimental and numerical methods.

The significant points and findings in each chapter are summarized below.

In Chapter 1, the characteristics and social demands of Mg alloys were presented. Based on the background, the purposes of the present study were stated and organization of this thesis was explained.

In Chapter 2, the Al coating technique for Mg alloys by hot extrusion, which is a basis of the present study, was explained. The Al-coated Mg alloy bars and plates were successfully fabricated by the hot extrusion technique and importantly, it was confirmed that these extrudates exhibited an excellent corrosion resistance. Furthermore, it was found that the die

angle and initial thickness of the Al coating plate influence on the coating thickness uniformity in the final product.

In Chapter 3, for the simulations of the present Al coating process followed by the sensitivity analysis, the flow stress model for AZ80 Mg alloy was developed by inverse analysis combined with the mechanical test and optimization process. Firstly, the basic algorithm and procedure of the inverse analysis are explained and rheological parameters in the three selected constitutive models were identified by the inverse analysis combined with the mechanical test and optimization process. This approach was verified by comparing the simulated load-displacement curves using the constitutive models incorporating the identified parameters to the experimental curves obtained from compression tests. Consequently, the flow stress model for AZ80 Mg alloy was determined.

In Chapter 4, the effects of extrusion parameters on the coating thickness uniformity were evaluated by the sensitivity analysis with the help of the numerical simulation incorporated the developed flow stress model for AZ80 Mg alloy. The effects of the following five parameters were evaluated; (1) the initial thickness of the Al coating plate, (2) the extrusion temperature, (3) the ram speed, (4) the die angle and (5) the strengths of core and coating materials. It has been found that the initial thickness of the coating material plate and die angle are the most significant parameters with respect to both the coating thickness uniformity and the average coating thickness.

In Chapter 5, the feasibility of fabrication of the Al-coated Mg alloy sheet was demonstrated with a view to the practical applications of the present coating technique. It has been found that even after the severe forging deformation through the sheet formation, the Mg/Al bonding is maintained and therefore, the Al-coated Mg alloy sheet exhibited an excellent corrosion resistance. Consequently, it has been indicated that the Al-coated Mg alloy extrudate is capable of subsequent forming with the excellent corrosion resistance.

In Chapter 6, the tensile properties of the Al-coated Mg alloy sheet was evaluated in order to demonstrate the deformability and mechanical properties of the sheet. The sheet showed a large and homogeneous elongation of 550 % at a temperature of 573 K and at a strain rate of 1.0×10^{-3} s^{-1}. Notably, it has been demonstrated that the Al coating layer continuously covers the Mg alloy substrate without breaking, even after such an extremely large elongation.

In Chapter 7, the large elongation of the sheet was specified and the deformation mechanism of the sheet was investigated. The strain rate sensitivity index was found to be approximately 0.4 at 573 K, indicating the large elongation can be classified as the superplasticity. The crystallographic orientation and fractographic analysis revealed that the Mg alloy substrate deformed with a mechanism of grain boundary sliding with the accommodation process of diffusion creep. In order to investigate the detailed deformation behavior of both the Mg alloy substrate and pure Al coating layer, the individual tensile tests for Mg alloy specimens and pure Al specimens were conducted. It was found that the Mg alloy specimen showed the superplastic elongation as much as 990 %, however, the individual pure Al was capable of the maximum elongation of as little as 47 %. The mechanism of the large elongation of the pure Al as a coating material on the Mg alloy substrate has been discussed. Consequently, it has been considered that the strong bonding at the Mg/Al interface suppresses the necking of the brittle pure Al by the uniform and superplastic deformation of the Mg alloy substrate. This theory has been supported by the observation fact of the strong bonding at the Mg/Al interface.

Moreover, the microstructure and crystallographic investigations of the pure Al coating layer on the Mg alloy substrate have revealed the microscopic deformation mechanism of the large elongation of the pure Al. It has been demonstrated that the restriction from the Mg alloy changes the major force to deform the pure Al from the tensile force to the compression force, which is harder to lead the fracture. Additionally, the reason of the equiaxed grains observed after the large elongation has been discussed and it has been considered that the most possible reason should be continuous dynamic recrystallization.

The Al-coated Mg alloy, developed and characterized in the present study, is extremely original and the present study has a significant importance especially in the industrial applications. As mentioned earlier, the market of the Mg alloys has been expanding and should be broader within a measurable period of time. Therefore, this promising technique would definitely contribute more or less and either directly or indirectly.

Since the present study has taken in the multiple fields of study, this study can act as a stimulus in each field and activate the contacts between those fields. Therefore, not only the scientific but also the academic impact can be expected from the present study.

Appendix

1. Newton-Raphson method

The Newton-Raphson method is an iterative solving method for a nonlinear problem which is hardly solved analytically. As so much of the differential calculus, it is based on a simple idea of linear approximation.

Figure A.1 illustrates an example of the application of the Newton-Raphson method.

Assume the first approximation point is x_0, and then find the intersection point, x_1, of the tangential line of function, $f(x)$ on (x_0, $f(x_0)$) and x axis. Set the point x_1 as the next approximation solution and this process is iterated until the solution converged. From Fig. A.1, it is clear that if the selection of the initiation point is adequate, the true solution, α, should be obtained by this iterative process.

The generalized algorithm is explained in the next section.

1.1 Algorithm

In order to solve the nonlinear problem as outlined above, a recurrence formula, indicating the next approximation point, x_{i+1}, from the first point, x_0 is necessary. Firstly, the tangential line of $f(x)$ at (x_0, $f(x_0)$) can be expressed as;

$$y - f(x_i) = f'(x_i)(x - x_i) \tag{A1.1}$$

where $f'(x_i)$ can be expressed as;

$$f'(x_i) = \frac{df(x_i)}{dx} \tag{A1.2}$$

Thus, the point x_{i+1} can be expressed as follows;

$$x_{i+1} = x_i - \frac{f(x_i)}{f'(x_i)} \tag{A1.3}$$

By using this equation, the point x_{i+1} can be calculated from x_i and the iteration process is repeated.

1.2 End of the process

The end of the process can be decided arbitrarily. However, the common conditional is;

$$\left|\frac{x_{i+1}-x_i}{x_i}\right| \leq \varepsilon \qquad \text{(A1.4)}$$

where the ε is constant, which can be decided arbitrarily. When the x_{i+1} fulfill the above conditional, the process end and the last x_{i+1} should be considered as a true solution.

This Newton-Raphson method is known to be one of the easiest and dependable solving method for the non-linear problems. However, it should be noted that the initial point should be selected carefully, otherwise the method would not give the correct solution or even would not be converged.

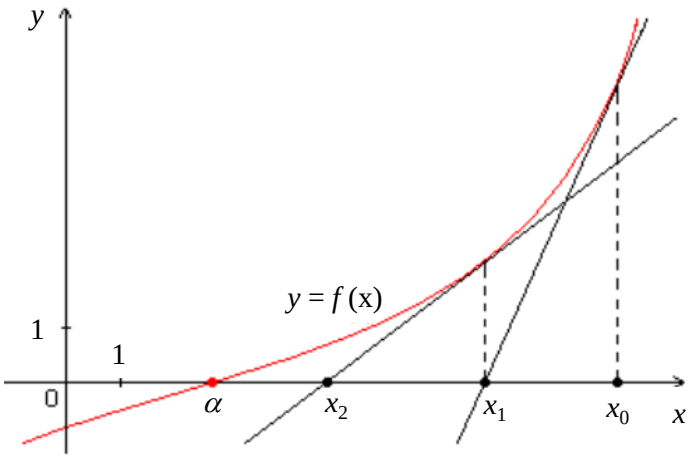

Fig. A1.1 Graphical illustration of the Newton-Raphson algorithm.

2. Nelder-Mead simplex method

The Nelder-Mead simplex method is one of the most popular direct search method for nonlinear unconstrained optimization. This method is efficient and robust in searching for a minimum, and is insensitive to the selection of an initiation point. The algorithm is explained below.

2.1 Algorithm [A2.1, A2.2]

Consider the minimization of a function of *n* variables, without constraints. P_0, P_1, …, P_n are the $(n+1)$ points in *n*-dimensional space defining the current "simplex". The y_i is the value of the objective function at point P_i, and define P_h as a point, showing the maximum (worst) of the objective function, y_h, and P_l as a point, showing the minimum (best) of the objective function, y_l. Furthermore, define $\bar{P}$ as the centroid of the points with $i \neq h$.

At each stage in the process, P_h is replaced by a new point. For the replacement, the following four operations are used; *reflection*, *expansion*, *contraction* and *shrinkage*. By replacing the worst point to the better one, the objective function approaches the local minimum. The process starts from the reflection. The reflection of P_h is denoted by P^r, and its coordinates are defined by the relation below;

$$P^r = (1+\rho)\bar{P} - \rho P_h \qquad \text{(A2.1)}$$

where ρ is a positive constant, the *reflection coefficient*. The ρ generally has a value of 1. Thus, the P^r is on the line joining P_h and $\bar{P}$, on the far side of $\bar{P}$ from P_h as shown in Fig. A2.1 (b). The obtained value, y^r, can result in the following three patterns;

1. $y_l \leq y^r < y_h$
2. $y^r < y_l$
3. $y_h \leq y^r$

If the result is in the pattern 1, $y_l \leq y^r < y_h$, the reflection succeeded and the P_h is replaced by P^r and the process is restarted with a new simplex. If the result is in the pattern 2, $y^r < y_l$, namely, the reflection produces a new minimum, then the expansion process proceeds and find the new point P^e, shown in Fig. A2.1 (c), by the relation as follows;

$$P^e = \gamma P^r + (1-\gamma)\bar{P} \quad \text{(A2.2)}$$

where γ is the *expansion coefficient*, which is greater than unity. Usually, the γ has a value of 2. The following two results can be considered;

A) $y^e < y_l$

B) $y^e > y_l$

If the result is in the pattern A, $y^e < y_l$, the P_h is replaced by P^e and the process is restarted with a new simplex. On the other hand, if the result is in the pattern B, $y^e > y_l$, which means that the expansion process did not succeed, therefore the P_h is replaced by P^r and the new process is restarted.

Back to the branching point of the result of the reflection process, if the result is in the pattern 3, $y_h \leq y^r$, the contraction process takes place by following the relation as below;

$$P^c = \beta P_h + (1-\beta)\bar{P} \quad \text{(A2.3)}$$

where β is the *contraction coefficient*, which lies between 0 and 1, and generally has a value of 0.5. Accordingly, P^c is on the line joining P_h and $\bar{P}$. Note that the P^c is never positioned on the far side of P_h as shown in Fig. A2.1 (d). The considerable results are;

I. $y^c < y_h$

II. $y^c > y_h$

If the result is in pattern I, $y^c < y_h$, this process gives the improvement of the objective function and the P_h is replaced by the P^c and the new process is restarted with a new simplex. If the result is in pattern II, $y^c > y_h$, then the point P_l remains unchanged and the whole simplex undergoes the shrinkage process. The shrinkage point, P^s, can be expressed as follows;

$$P^s = \delta(x_l + x_i) \quad \text{(A2.4)}$$

where δ is the *shrinkage coefficient*, which lies between 0 and 1. Generally, this shrinkage coefficient is 0.5, therefore the whole simplex shrinks and then the process restarts with the shrunk simplex.

2.2 End of the process

The end of the process can be decided arbitrarily. However, with introducing a parameter, α, the following conditional is generally applied;

$$\alpha > \frac{2|y^h - y^l|}{|y^h| + |y^l|} \tag{A2.5}$$

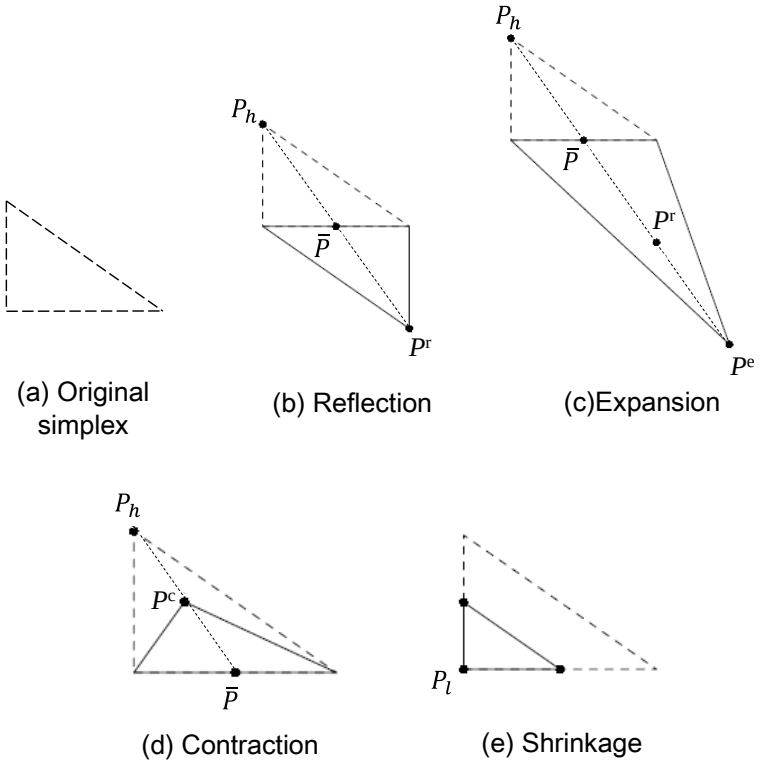

Fig. A2 The simplexes after a variety of operations in Nelder-Mead simplex method [A2.1].

References

[A2.1] J.A. Nelder and R. Mead (1965) A simplex method for function minimization. *Comput. J.*, **7**, 308-313.

[A2.2] J.C. Lagarias, J.A. Reeds, M.H. Wright and P.E. Wright (1998) Convergence properties of the Nelder-Mead simplex method in low dimensions. *SIAM J. Optim.*, **9**, 112-147.